NTNU

Norwegian University of
Science and Technology

Influence of a Wavefoil on the Wave Pattern Resistance of a Ship

Benjamin Vist Hagen

Marine Technology
Submission date: August 2018
Supervisor: Sverre Steen, IMT
Co-supervisor: Eirik Bøckmann, IMT

Norwegian University of Science and Technology
Department of Marine Technology

NTNU Trondheim
Norwegian University of Science and Technology
Department of Marine Technology

MASTER THESIS IN MARINE TECHNOLOGY

SPRING 2018

FOR

Benjamin Vist Hagen

Influence of a wavefoil on the wave pattern resistance of a ship.

Hydrofoils mounted in the bow region of a conventional displacement ship hull provides thrust when the ship moves forward in waves. This type of foil is sometimes called a wave foil. However, there will be an interaction between the steady wave patterns of the foil and ship hull which might increase or decrease the total wave making resistance, dependent on the placement of the foil relative to the hull. In that sense, the foil has an effect which is similar to a bulb. It is planned to study this interaction by means of CFD.

The objective of the master thesis is to investigate the effect of a wave foil on the wave pattern resistance of a ship. The master thesis will focus on a particular case, while it is the general understanding of the importance of the wave foil on the ship wave resistance that is sought.

The methods and methodology applied in the analyses shall be well documented and validated as far as time allows. The computational results shall be analysed in order to obtain an understanding of how the wave pattern resistance is influenced by the wave foils. The practical importance of the wave foils on the wave pattern resistance of the ship shall be discussed. If the wavefoils are found to be important for the wave pattern resistance, practical implications, for instance with respect to placement of the foils, shall also be discussed.

In the thesis the candidate shall present his personal contribution to the resolution of problem within the scope of the thesis work.

Theories and conclusions shall be based on mathematical derivations and/or logic reasoning identifying the various steps in the deduction.

The thesis work shall be based on the current state of knowledge in the field of study. The current state of knowledge shall be established through a thorough literature study, the results of this study shall be written into the thesis. The candidate should utilize the existing possibilities for obtaining relevant literature.

The thesis shall be organized in a rational manner to give a clear exposition of results, assessments, and conclusions. The text should be brief and to the point, with a clear language. Telegraphic language should be avoided.

The thesis shall contain the following elements: A text defining the scope, preface, list of contents, summary, main body of thesis, conclusions with recommendations for further work, list of symbols and acronyms, reference and (optional) appendices. All figures, tables and equations shall be numerated.

NTNU Trondheim
Norwegian University of Science and Technology
Department of Marine Technology

The supervisor may require that the candidate, in an early stage of the work, present a written plan for the completion of the work. The plan shall include a budget for the use of laboratory or other resources that will be charged to the department. Overruns shall be reported to the supervisor.

The original contribution of the candidate and material taken from other sources shall be clearly defined. Work from other sources shall be properly referenced using an acknowledged referencing system.

The thesis shall be submitted electronically (pdf) in DAIM:

- Signed by the candidate
- The text defining the scope (this text) (signed by the supervisor) included
- Computer code, input files, videos and other electronic appendages can be uploaded in a zip-file in DAIM. Any electronic appendages shall be listed in the main thesis.

The candidate will receive a printed copy of the thesis.

Supervisor : Professor Sverre Steen
Co-supervisor : Eirik Bøckmann
Start : 12.01.2018
Deadline : 13.08.2018

Trondheim, 12.01.2018

Sverre Steen
Supervisor

Abstract

The Reynolds-averaged Navier-Stokes equation has been numerically solved in order to study the interaction between the steady wave patterns of a wavefoil and ship hull, using the open source software OpenFOAM. Turbulence is modelled using the k-ω SST model. Theories applied concerning wave resistance, hydrofoils and computational fluid dynamics are described. A detailed description of methods used in setting up the numerical analyses are given, with important aspects to consider in computational fluid dynamics included.

A thorough literature study has shown the positive aspects of a wavefoil in creating a thrust force in waves, and by so reducing the total resistance and fuel consumption. However, in calm water conditions there will be an interaction between the steady wave patterns of the wavefoil and ship hull, increasing the total resistance. This interaction effect is studied further in this thesis.

All the Numerical analyses uses the Duisburg Test Case ship model hull due to the availability of the geometry in OpenFOAM and reference data. The wavefoil is modelled with a NACA 0018 cross-section profile and a sharp trailing edge. Further, the wavefoil has zero angle of attack relative to the undisturbed flow.

A double body study on the bare ship hull shows little variation in frictional resistance with varying grid density and resolution of the boundary layer. The form factor was found to be k = 0.086 from the double body analysis, yielding a relative difference of -8.5% when compared to available reference data.

Analyses on the bare hull, including a free surface, was performed in order to find the calm water resistance and steady wave patterns for three forward speeds. Systematic mesh and time step independence studies were performed in order to reduce error. Results show that for Fn=0.209 and Fn=0.218 the resistance is respectively underestimated by 10.35% and 10.78% when compared to model test results. Nevertheless, the results are considered stable and physical, but possible improvements have been discussed. Letting the model be free to heave and pitch, or running the simulation with sinkage and trim data from model tests, may have resulted in closer resistance predictions with respect to model tests.

Results for the ship hull with the wavefoil show that the calm water total resistance increases relative to the bare hull, even though the wavefoil produces a thrust force. The relative difference between the total resistance of the ship hull with the wavefoil and the bare ship hull for Fn=0.209, Fn=0.218 and Fn=0.226, is respectively found to be 8.43%, 8.00% and 8.14%. By inspection of the wave elevations on the ship hull and the steady wave patterns, it is found that the wavefoil amplifies the bow wave and alters the wave pattern. A reason for the amplification of the bow wave is found to be a negative angle of attack on the wavefoil from the flow due to the ship hull. This causes a wave crest being formed on the free surface directly above the wavefoil. Thus, the wavefoil in this study affects the steady wave pattern resistance in a negative manner.

To avoid amplification of the bow wave, the wavefoil can be rotated, giving it a positive angle of attack relative to the inflow. This may cause a wave through to be formed on the free surface above the wavefoil and cancellation of the bow wave. Further, the wavefoil should have a longitudinal position where the wave-making due to the wavefoil and the ship bow are out of phase, which will yield a cancellation effect. Assuming linearity, forces in calm water and forces due to incoming waves can be superimposed, meaning that the

negative interaction effect on the wave pattern will be present in waves also. In a design phase, it therefore is recommended to consider these aspects, such that the interaction effect is also accounted for in waves.

Sammendrag

Reynolds-averaged Navier-Stokes ligningen har blitt løst numerisk for å studere interaksjonen mellom bølgemønstrene til en bølgefoil og et skipsskrog ved bruk av open source programmet OpenFOAM. Turbulens er modellert ved bruk av k-ω SST-modellen. Benyttet teori som omhandler bølgemotstand, hydrofoiler og beregnende væskedynamikk er beskrevet. En detaljert beskrivelse av metoder brukt i oppsett av numeriske modeller er gitt, med vurdering av viktige aspekter i beregnende væskedynamikk inkludert.

Et grundig litteraturstudium har vist de positive fordelene til en bølgefoil, hvor en foroverkraft skapes i bølger. Dette leder til redusert totalmotstand og drivstofforbruk. Imidlertid er det under forhold i stille vann funnet at bølgemønstrene til bølgefoilen og skipsskroget vil samhandle og øke motstanden. Denne samhandlingen er studert videre i denne hovedoppgaven.

Duisburg Test Case-skipsskroget i modellskala er benyttet i alle numeriske analyser på grunn av tilgjengelig referansedata, samt at geometrien allerede er tilgjengelig i OpenFOAM. Bølgefoilen er modellert med et NACA 0018 tverrsnitt og en skarp følgende kant. Videre har bølgefoilen null angrepsvinkel relativt til den uforstyrrede strømningen.

En double body-studie av det bare skroget viser liten variasjon i friksjonsmotstanden med varierende mesh-tetthet og oppløsning av grensesjiktet. Formfaktoren er funnet til å være k = 0.086 fra double body-analysen, noe som resulterer i en relativ forskjell på -8.5% sammenlignet med tilgjengelig referansedata.

Analyser på det bare skipsskroget, med en fri overflate inkludert, ble utført for å finne motstanden i stille vann og bølgemønstrene for tre foroverhastigheter. Systematiske uavhengighetsstudier for beregningsnett og tidssteg ble utført for å redusere feil. Resultater for Fn=0.209 og Fn=0.218 viser at motstanden er underestimert med henholdsvis 10.35% og 10.78% sammenlignet med forsøk i modellskala. Resultatene er likevel ansett å være stabile og fysiske, men mulige forbedringer er diskutert. Ved å la modellen være fri til hiv- og stamp-bevegelse, eller benytte nedsenking- og trim-data fra modellforsøk, kunne de numeriske motstandspredikasjonene ha kommet nærmere motstanden fra modellforsøk.

Resultatene for skipsskroget med bølgefoilen viser at stillevannsmotstanden øker sammenlignet med det bare skipsskroget, selv om bølgefoilen skaper en foroverkraft. Den relative forskjellen mellom totalmotstanden for skipsskroget med bølgefoil og det bare skipsskroget for Fn=0.209, Fn=0.218 og Fn=0.226, er henholdsvis funnet til å være 8.43%, 8.00% og 8.14%. Ved inspeksjon av bølgehevningene på skipsskroget og bølgemønstrene, er det funnet at bølgefoilen amplifiserer baugbølgen og endrer bølgemønsteret. En grunn til amplifiseringen av baugbølgen er funnet til å være en negativ angrepsvinkel på bølgefoilen på grunn av strømingen forårsaket av skipsskroget. Dette fører til at en bølgetopp formes på den frie overflaten direkte ovenfor bølgefoilen. På denne måten vil bølgefoilen i denne studien påvirke bølgemønstermotstanden negativt.

For å unngå amplifikasjon av baugbølgen kan bølgefoilen roteres, noe som vil gi en positiv angrepsvinkel relativ til innstrømningen. Dette kan føre til at en bølgedal formes på den frie overflaten ovenfor bølgefoilen og en kansellering av baugbølgen. Videre må bølgefoilens langsgående plassering være slik at bølgelagingen på grunn av bølgefoilen og skipsskroget er ute av fase, noe som vil føre til en kansellerende effekt. Ved å anta linearitet kan krefter i stille vann og krefter på grunn av innkommende bølger superponeres,

hvilket betyr at den negative interaksjonseffekten på bølgemønsteret også vil være til stede i bølger. I en design fase er det derfor anbefalt å overveie disse aspektene, slik at interaksjonseffekten også blir tatt i betraktning i bølger.

Preface

The work presented in this report is a master thesis in Marine Technology at the Department of Marine Technology, NTNU, Trondheim, Norway. Due to unforeseen external occurrences out of the author's control the work has been somewhat delayed, and has been carried out during the spring and summer of 2018. It marks the end of a five-year integrated master's degree.

There have been new topics and software to learn during the work period. A lot of the time has been dedicated to setting up numerical models and learning the software - especially when it came to setting up the numerical grids. At times the work has been challenging, but the entire process is found interesting and outermost educational. To be able to work with wavefoils, considering the positive aspects they can have for ships and the environment, is found rewarding.

The author would like to acknowledge the following persons for their contributions, for which he is grateful:

Supervisor Professor Sverre Steen for the opportunity to work with the project topic, his help in defining the scope of the work and report guidance.

Co-supervisor Postdoctoral Fellow Eirik Bøckmann for his contributions in providing the topic and guidance during the work period.

PhD Candidate Jarle Kramer for his shared insight in computational fluid dynamics and OpenFOAM, which is found invaluable to the author.

PhD Candidate Håkon Strandenes for his help in getting started with simulations on the super computer Vilje.

My friends who have made my studies fun and entertaining.

My family for their continuous support throughout the entire course of my education.

Trondheim, 10.08.2018

Benjamin Vist Hagen

Contents

1 Introduction **1**
1.1 Background and Motivation . . . 1
1.1.1 Studies on Wave Propulsion . . . 2
1.1.2 Remarks on Presented Literature . . . 4
1.2 Objective . . . 5
1.3 Scope and Limitations . . . 5

2 Ship Resistance **7**
2.1 Overview of Ship Resistance Components . . . 7
2.2 Flow Parameters and Resistance Coefficients . . . 8
2.3 Wave-making Resistance and Wave System . . . 10
2.4 Appendage Resistance . . . 12

3 Foil Theory **15**
3.1 Foil Terminology . . . 15
3.2 Forces and Force Coefficients . . . 16
3.3 Hydrofoil Beneath a Free Surface . . . 17
3.4 Foil Thrust . . . 19

4 Mathematical Description of CFD **21**
4.1 Navier-Stokes and RANS Equations . . . 21
4.2 Turbulence Model: k-ω SST . . . 23
4.3 Boundary Layer Theory . . . 24
4.3.1 Dimensionless Velocity Profiles: Law of the Wall . . . 25

5 Numerical Method and Considerations **29**
5.1 OpenFOAM . . . 29
5.2 Meshing . . . 30
5.3 Initial Conditions for Turbulent Parameters . . . 32
5.4 OpenFOAM Numerical Solvers and Algorithms . . . 33
5.4.1 simpleFoam . . . 33
5.4.2 interFoam . . . 33
5.4.3 Specific Solvers for Flow Parameters and Discretisation Schemes . . . 34
5.5 Stability . . . 35
5.6 Forces in OpenFOAM . . . 35
5.7 Error Sources in Numerical Modelling and Solving . . . 36
5.8 Computational Resources . . . 37

6 Ship Model and Numerical Models **39**
6.1 Ship Model: Duisburg Test Case . . . 39
6.2 Double Body Model . . . 40
6.3 Bare Hull With Free Surface Model . . . 41
6.4 Hull With Wavefoil Model . . . 42
6.5 Explanation of Boundary Conditions . . . 44

7 Results and Discussion **47**
7.1 Double Body Analysis . . . 47
7.2 Bare Hull With Free Surface Analysis . . . 49
7.2.1 Mesh Independence Study . . . 49
7.2.2 Time Step Study . . . 52
7.2.3 Final Results Bare Hull Analysis . . . 54
7.3 Ship Hull With Wavefoil Analysis . . . 58
7.3.1 Mesh . . . 58
7.3.2 Results . . . 59
7.4 Discussion on Using Wavefoils . . . 67

8 Conclusions and Further Work **71**
8.1 Conclusions . . . 71
8.2 Suggestions for Further Work . . . 73

Bibliography **74**

Appendix **I**

A Solver Files - fvSolution **I**

B Discretisation Files - fvSchemes **V**

C Additional Results - Bare Hull **IX**
C.1 Pressure Resistance Mesh Independence Study . . . X
C.2 Residuals From Mesh Independence Study . . . XI
C.3 Pressure Resistance Time Step Study . . . XII
C.4 Residuals From Time Step Study . . . XIV
C.5 Results for Three Forward Speeds . . . XVI

D Additional Results - Hull With Wavefoil **XIX**

E Electronic Appendages **XXV**

List of Figures

2.1 Basic hydrodynamic resistance components. 8
2.2 Wave system components (Molland et al., 2011, figure 3.15.). 11
2.3 Wave system of a ship showing divergent and transverse waves (Molland et al., 2011, figure 3.13.). 11
2.4 Kelvin wave pattern (Faltinsen, 2005, figure 4.3). 12

3.1 Foil geometry and definitions. 15
3.2 Illustration of a hydrofoil beneath a free surface. 18
3.3 Drag and wave resistance on a hydrofoil with different submergence depths. 19
3.4 Thrust force, T, on a foil due to inflow with an angle. 19

4.1 Illustration of the Law of the Wall (Tennekes and Lumley, 1972, figure 5.6). 27

5.1 Overview of case file structure in OpenFOAM. 30

6.1 Computational domain used in the double body analysis. 41
6.2 Computational domain used in the free surface analyses. 42
6.3 Ship hull with wavefoil attached. 43

7.1 Viscous resistance convergence and friction coefficient for double body mesh independence study, Fn = 0.218. 48
7.2 Non-dimensional distance to the wall, y^+, on ship hull surface for mesh with 1 817 181 cells. 48
7.3 Convergence of total and viscous resistance for mesh independence study of bare hull analysis, Fn = 0.218. 50
7.4 Non-dimensional distance to the wall, y^+, on ship hull for the mesh independence study, Fn = 0.218. 51
7.5 Convergence of total and viscous resistance for time step study on mesh 1 of bare hull analysis, Fn = 0.218 52
7.6 Convergence of total and viscous resistance for time step study on mesh 2 of bare hull analysis, Fn = 0.218. 53
7.7 Calculated total resistance compared to experimental results. 54
7.8 Wave elevations on the bare ship hull for Fn = 0.218. 55
7.9 Wave pattern generated by ship hull at Fn = 0.218. 56
7.10 Angle of flow relative to undisturbed flow at longitudinal and vertical position where wavefoil will be placed, Fn = 0.218. 57
7.11 2D free surface elevation caused by NACA 0015 hydrofoil with α = -5°, $h/c = 2$ and $Fn_h = 0.83$. 57
7.12 Mesh at intersection and cross-section of wavefoil. 58

7.13 Convergence of forces on hull and wavefoil for Fn = 0.218. 60
7.14 Non-dimensional distance to the wall y^+, ship with wavefoil analysis for Fn = 0.218. 60
7.15 Calm water resistance and foil thrust. 62
7.16 Wave elevations on ship hull with and without wavefoil. 63
7.17 Wave patterns at Fn = 0.209. 64
7.18 Wave patterns at Fn = 0.218. 65
7.19 Wave patterns at Fn = 0.226. 66
7.20 Flow angle relative to undisturbed flow over the span of the wavefoil at longitudinal and vertical position of the leading edge. 69

C.1 Convergence of pressure resistance for mesh independence study of bare hull. X
C.2 Residual convergence from mesh independence study of bare hull. XI
C.3 Convergence of pressure resistance for time step study on mesh 1 of bare hull. XII
C.4 Convergence of pressure resistance for time step study on mesh 2 of bare hull. XIII
C.5 Residual convergence from time step study on mesh 1 of bare hull. XIV
C.6 Residual convergence from time step study on mesh 2 of bare hull. XV
C.7 Convergence history total and viscous resistance for three forward speeds - Bare hull analysis. XVI
C.8 Convergence history pressure resistance for three forward speeds - Bare hull analysis. XVII
C.9 Residual convergence for three forward speeds - Bare hull analysis. XVIII

D.1 Convergence of total and viscous resistance on hull. XX
D.2 Convergence of pressure resistance on hull. XXI
D.3 Convergence of forces on wavefoil. XXII
D.4 Residual convergence - Hull with wavefoil analysis. XXIII

List of Tables

5.1 Specifications of Vilje. 37

6.1 Fluid properties and gravitational acceleration used in analyses. 39
6.2 Main dimensions of DTC hull in design loading condition (El Moctar, Shigunov, et al., 2012, table 1). 40
6.3 Results of resistance model tests DTC hull (El Moctar, Shigunov, et al., 2012, table 4). 40
6.4 Boundary conditions used in double body analysis. 41
6.5 Boundary conditions for free surface bare hull model. 42
6.6 Boundary conditions for hull with wavefoil model. 43
6.7 Dimensions of wavefoil. 43

7.1 Mesh independence study double body analysis, Fn = 0.218. 47
7.2 Mesh parameters for mesh independence study. 49
7.3 Resistance results for mesh independence study of bare ship hull, Fn = 0.218. 49
7.4 Resistance results for time step study of bare hull analysis, Fn = 0.218. . . 52
7.5 Resistance on bare ship hull. 54
7.6 Resistance on ship hull not including forces on wavefoil. 61
7.7 Forces on wavefoil. 61
7.8 Resistance on ship hull including wavefoil. 61

Acronyms

CFD - Computational fluid dynamics

CFL condition - Courant-Friedrichs-Lewy condition

DTC - Duisburg Test Case

DWT - Deadweight tonnage

GAMG - Geometric-algebraic multi-grid

NS - Navier-Stokes

PIMPLE - PISO + SIMPLE

PISO - Pressure-implicit with splitting of operators

RANS - Reynolds-averaged Navier-Stokes

SIMPLE - Semi-implicit method for pressure linked equations

SST - Shear stress transport

VOF - Volume of fluid

List of Symbols

α	Angle of attack
$\delta(x)$	Boundary layer thickness
κ	Constant describing logarithmic region of boundary layer
μ	Dynamic viscosity
μ_t	Turbulent dynamic viscosity
∇	Differential operator
ν	Kinematic viscosity
ν_t	Turbulent kinematic viscosity
ω	Specific eddy dissipation rate
$\overline{p}$	Time average over the time scale of turbulence for pressure
$\overline{u}$	Time average over the time scale of turbulence for velocity component in x-direction
$\overline{v}$	Time average over the time scale of turbulence for velocity component in y-direction
$\overline{w}$	Time average over the time scale of turbulence for velocity component in z-direction
ρ	Density of fluid
ρ_a	Density air
ρ_w	Density water
τ	Boundary layer shear stress
τ_l	Viscous shear stress
τ_t	Turbulent shear stress
τ_w	Wall shear stress, frictional stress
A	Projected area of foil in lift direction for zero angle of attack
Asp	Aspect ratio
B	Constant describing logarithmic region of boundary layer
B_{wl}	Waterline breadth
c	Chord length

C_B	Block coefficient
C_D	Drag coefficient
C_F	Friction coefficient
C_f	Friction coefficient
C_L	Lift coefficient
C_T	Total resistance coefficient
C_W	Wave resistance coefficient
F_D	Drag force
F_i	Force in direction i
F_L	Lift force
Fn	Froude number
Fn_h	Submergence Froude number
g	Gravitational acceleration
h	Submergence depth
h/c	Submergence to chord ratio
I	Turbulent intensity
k	Total turbulent kinetic energy, form factor
L	A representative length
l	Turbulent length scale
L_{pp}	Length between perpendiculars
n	Surface normal
p	Pressure
p'	Fluctuating part of pressure
R_P	Pressure resistance
R_T	Total resistance
R_V	Viscous resistance
R_W	Wave resistance
Re	Reynolds number
S	Wetted surface area
s	Foil span
S_w	Wetted surface under waterline at rest
T	Thrust force

t	Time, thickness
T_m	Draught midships
U	Free stream velocity, incident flow velocity, velocity of moving body
u	Velocity component in x-direction
u'	Fluctuating part of velocity component in x-direction
u^+	Dimensionless velocity in the boundary layer
U_∞	Free stream velocity
U_{design}	Design speed
v	Velocity component in y-direction
v'	Fluctuating part of velocity component in y-direction
$v*$	Wall friction velocity
w	Velocity component in z-direction
w'	Fluctuating part of velocity component in z-direction
y^+	Dimensionless distance from wall

Chapter 1

Introduction

1.1 Background and Motivation

To counteract global climate change and limit the rise of global temperatures, the Paris Agreement on climate change entered into force in 2016 (United Nations, 2018). Adapting countries have agreed to keep the global temperature rise well below 2 degrees Celsius and strive for 1.5 degrees Celsius (United Nations, 2018). In 2012, anthropogenic CO2 emissions due to shipping accounted for 2.6% of the global emissions, and future emissions are expected to increase by 150 - 250% within 2050 (Bouman et al., 2017). Therefore, it is clear that the shipping industry must play its part in the reduction of greenhouse gas emissions.

For ships, finding and developing alternative fuel sources and utilizing clean energy such as solar, wind and wave energy can be highly motivated by the goal to keep the global temperature rise below 2 degrees Celsius. A promising way to reduce the resistance of a ship, and thereby reduce fuel consumption in a seaway is to utilize wave energy through energy saving devices, where the energy from the waves are converted into a propulsive thrust through the energy saving device.

For a conventional displacement ship hull, hydrofoils can be placed in the bow region. When the ship advances forward in waves it will experience vertical motions, and the relative vertical motion between the hydrofoils and the water are converted into a propulsive thrust (see for instance Faltinsen (2005, page 211)). Such foils can be called wavefoils, and will here on out be referred to by this name.

The idea of propelling boats by means of wave energy has been around for a long time. A patent for utilising wave energy for propulsion was made as early as in 1858, and a successful attempt of building a wave powered boat was made in 1890s (Bøckmann, 2015, Bøckmann and Steen, 2016). Arguably the simplest ways to utilise wave energy for propulsion, and the most common way to do so, is through outfitting a ship with foils (Bøckmann and Steen, 2016). However, experiments by Bøckmann and Steen (2016) show that wave propulsion with bow mounted hydrofoils can be challenging in calm water, due to an increase in calm water resistance when the foils are mounted compared to the bare hull. Thus, it may be interesting to take a further look at the causes for the calm water findings of Bøckmann and Steen (2016).

1.1.1 Studies on Wave Propulsion

Theoretical and experimental studies that explored thrust generation of a hydrofoil advancing in waves were carried out and presented over a series of four reports by Isshiki (1982a), Isshiki (1982b), Isshiki and Murakami (1983), and Isshiki and Murakami (1984). In the first report, already existing theory was improved by Isshiki (1982a) by including the free surface effect approximately. The first report further studied the thrust from a non-oscillating hydrofoil advancing in waves and it was found that the free surface effect should not be neglected. In the second report by Isshiki (1982b) optimized foil motions in heave and pitch were explored, with the the requirement that the motions are power free. It is concluded in the report that through optimisation, a high wave devouring efficiency can be attained. Additionally, when a free surface is included, it is argued that an optimum submergence depth of the foil can be found where the thrust takes its maximum.

In the third (Isshiki and Murakami, 1983) and fourth (Isshiki and Murakami, 1984) report, thrust generation through absorption of wave energy by an advancing hydrofoil was verified experimentally. The hydrofoil was allowed to heave and pitch passively through the use of springs, which gave restoring forces for the hydrofoil motions. Effects of foil draft, heave and pitch springs, and an auxiliary float were theoretically investigated in the fourth report (Isshiki and Murakami, 1984). When a float, properly attached to the foil, was used a larger thrust force was found than without a float.

Grue et al. (1988) examined an advancing foil moving in water close to a free surface theoretically with a two-dimensional model and all equations linearized. The problem was solved by applying a vortex distribution along the centre line of the foil and the wake, and then solving for the local vortex strength. It was found that when the foil is moving in incoming waves, a relatively large amount of the wave energy may be extracted for propulsion. The theory was further examined for application on the propulsion of a ship by a foil propeller. In head waves, with wave amplitude equal to 0.5m, it was found that a 40m long ship would travel at 4m/s. The theory by Grue et al. (1988) is also compared to the experimental results of Isshiki and Murakami (1984), with various degrees of agreement.

Naito and Isshiki (2005) summarised the state-of-the-art in bow wing research in 22 topics. Further, they conducted experiments with an actively pitch controlled bow wing (wavefoil), where the wing's effect on the thrust was confirmed through measurement of ship resistance. Furthermore, it is suggested by Naito and Isshiki (2005) that by calculation of the interference flow field, the shape, angle and installation position of the bow foil can be examined. By such, the optimum condition for the foil can be found. However, they also state that an optimum position for bow foils that do not increase total resistance in calm water has not been found (as of the year published). They recommend a system that can store the foils in order to avoid the negative effects of foils in calm water and very rough seas - resistance increase and slamming, respectively. If fixed wavefoils are used, and no storage system is included, it is recommended that the foils are designed for the most effective sea condition.

Free running tests, where wave energy alone is the propulsive force, of a 2 metre ship model of an 80 metre long container ship was conducted by Nagata et al. (2010). The ship model was outfitted with a hydrofoil placed below and just in front of the bow region. In head sea, the model achieved a forward speed of nearly 0.7m/s for the most favourable

scenario considering wave height and wave length combination. In following sea, the most favourable scenario resulted in a forward speed of just above 0.6m/s.

Two studies by Belibassakis and Politis (2012, 2013) investigated an oscillating wing located beneath a ship hull. In the studies, the wing experienced vertical motion due to the heaving and pitching motions of the ship, and active pitching motion imposed by an external mechanism. Further, a boundary element method was used in order to model the forces on the wing. Results of Belibassakis and Politis (2012) indicate that the studied wing is a good mechanism for transforming the hull kinetic energy into a useful thrust in rough seas. Additionally, the wing reduced the ship motions in waves. The same results was found in the study of Belibassakis and Politis (2013) over a range of motion parameters.

Politis and Politis (2014) studied a biomimetic wing with active pitch control by using a boundary element method. They developed a formula by which the instantaneous pitch angle of the wing is determined using the heaving data of the current and past time steps. Their result show that the proposed active pitch control always result in thrust producing motions. In addition, it is found that the power required to set the pitch angle is a small percentage of the useful wave power.

A numerical study of a two-dimensional oscillating hydrofoil was carried out by De Silva and Yamaguchi (2012). They used the commercially available software FLUENT to solve the Reynolds-averaged Navier-Stokes equation, and modelled free surface waves and motions of the flapping foil by implementing a user-defined function technique. The numerical calculations were compared to the experimental results of Isshiki and Murakami (1984), where De Silva and Yamaguchi (2012) used an active type oscillation foil and the experimental study was conducted with a passive type oscillation foil. The numerical results were found to be in good agreement with the experimental results. It is further found in the numerical study of De Silva and Yamaguchi (2012) that both thrust and efficiency peaks when the oscillation frequency of the foil is equal to the wave encounter frequency. Additionally, a number of other design parameters are presented in the numerical study, which if correctly maintained can increase the wave energy absorption of the oscillating hydrofoil.

Bøckmann (2015) studied the effect of a wavefoil, with placement beneath the bow, and the effect of stall on the wavefoils. The wavefoils used in the investigations were fixed, pitch-controlled, and spring-loaded. He used a slightly modified version of the Leishman-Beddoes dynamic stall model for the wavefoil forces, which was implemented in the ship simulator VeSim. The model was compared to experiments and it gave good estimates of the average foil thrust. However, it did have some problems with not always being able to reproduce the experimental force histories. For a 90 metre long platform supply vessel with a fixed wavefoil, simulations gave fuel savings between 2 and 15% when sailing at 15 knots in what was considered to be typical North Sea waves. Bøckmann (2015) did not account for flow interaction between the ship hull and the wavefoil in his simulations. As he argues, the interaction will reduce the predicted fuel savings as the hull will generally reduce the inflow angles to the foil. Lastly, he concludes that pitching foils can reduce the ship resistance significantly relative to a fixed foil for waves producing the most violent ship motions in his simulations.

Further studies by Bøckmann and Steen (2016) used foils placed in the bow of a conventional displacement ship hull for a 8000 DWT tanker, with wavefoils having a fixed

roll angle of 10 degrees and a fixed pitch angle of 0 degrees. Experiments showed that in head sea the ship resistance was reduced by 9-17% when employing wavefoils, according to scaled model test resistance. However, in calm water conditions it was found that the ship resistance increased with the wavefoils when compared to the bare hull calm water resistance, even though the wavefoils produced a significant thrust force. The wavefoils were able to produce thrust due to the inflow having an angle off attack on the foils caused by the hull form. Further, it is believed that the interaction between the hull and wavefoils alters the wave-making of the ship, increasing the wave-making resistance and thus the total resistance in the study.

Fuel savings for a general cargo ship with retractable wavefoils were studied by Bøckmann, Yrke, et al. (2018), using ShipX from Sintef Ocean. Two round-trip shipping routes were studied in order to not only account for selected wave conditions. Their results show, for the most favourable shipping route studied, an average fuel saving of 22% with deployed wavefoils compared to the ship with foils retracted. It was concluded that it was mostly the foil thrust that effected the fuel savings, and not only increasing the brake power of the ship's main propulsion system.

Reduction of wave-making resistance in calm water on a ship using hydrofoils was experimentally studied by Abkowitz and Pauling Jr. (1953). They argued that a hydrofoil at an angle of attack could be a promising way of reducing the wave-making resistance. This is because the hydrofoil will produce a low pressure region and cause a hollow in the free surface, which can cancel out the high pressure region caused by the bow at the water line. A series of resistance test was conducted for a model scale passenger-cargo ship, which was compared with the total resistance of the same ship with hydrofoils mounted. Results showed that at low speeds the resistance increased with the hydrofoils. This is believed to be due to the additional drag force caused by the hydrofoil, and the lower importance of wave-making resistance at low speeds relative to high speeds. For higher speeds, the results showed that the hydrofoil had reduced the total resistance more than it had added to the drag force.

1.1.2 Remarks on Presented Literature

The presented studies show that there can be significant positive effects by using wavefoils - and that they can be used as an auxiliary propulsion system. Not only does total resistance and fuel consumption decrease, the wavefoils also dampen motions in a seaway.

The increased total resistance findings in calm water conditions of Bøckmann and Steen (2016) is supported by the study of Naito and Isshiki (2005), which says that an optimum condition that minimise the resistance in calm water can be found by calculating the interference flow field between the hull and the foil. Bøckmann and Steen (2016) believes that the interaction between the hull and foil causes an increase in the wave-making resistance in calm water. The interaction effect can be said to be supported by the experiments of Abkowitz and Pauling Jr. (1953), who in contrast investigated the use of a hydrofoil to reduce the wave-making resistance of a ship.

Hence, it is of interest to study the interaction between the steady wave patterns of the wavefoils and the hull in calm water conditions. Depending on the placement of the foils relative to the hull the total wave-making resistance is believed to increase or decrease.

In this sense the wavefoils have an effect similar to that of a bulb (as argued by Abkowitz and Pauling Jr. (1953)).

Computational fluid dynamics (CFD) can be used to investigate the interaction effect. One of the main advantages using CFD is that details such as shear stresses, velocity and pressure profiles, and stream lines can be obtained (Çengel and Cimbala, 2014, page 880). Thus, CFD analysis of the interaction between the ship hull and wavefoils can provide detailed insight in the flow pattern, which will help understand the effect of wavefoils in calm water. Furthermore, studies by Karim et al. (2014) and Prasad et al. (2015) suggests that CFD methods are well suited for calculations of a hydrofoil beneath a free surface, due to the prediction of forces and hydrofoil created wave profiles compared to experimental data. Additionally, there exist several studies showing the capability of CFD in calculating ship resistance. One example is the study by El Moctar, Sigmund, et al. (2017) who studied the added resistance of two different ships in calm water and regular head waves, where results were found to be in agreement with model tests. Therefore, it will be interesting to analyse a ship hull with wavefoils appended using CFD.

1.2 Objective

The current research aims to investigate the effect of wavefoils on the wave pattern resistance of a ship by means of CFD. The analyses are performed for a particular case, with one ship type and foil geometry. However, it is the general understanding of the importance of the wavefoils on the ship wave resistance that is sought.

In order to achieve reliable results, partial objectives are made in order to validate calculations and produce trustworthy analyses:

- Validate the frictional force on the bare ship hull with relevant reference data using a double body simulation (i.e. not including the free surface).
- Validate the resistance of the bare ship hull and wave-making with relevant reference data.
- Adding wavefoil to the ship hull and investigate the interaction between the ship hull and wavefoil.

1.3 Scope and Limitations

The scope of the work involves a description of background theory, numerical analysis and interpretation, and can be summed up as follows:

1. Present relevant theory used in the work.
    - Ship resistance theory.
    - Foil theory.
    - Mathematical description of computational fluid dynamics and boundary layer theory.

2. Description of the numerical methods used in solving the problem.
3. Set up numerical models and simulations using OpenFOAM.
4. Analyse and discuss the results.

As the current research have been performed in a set time frame, the limitations connected to the study are mainly related to time. A lot of the time has been dedicated to setting up satisfactory numerical models. Further, sufficient computational power have been available, but the time steps involved in the numerical analyses are small due to the grid fineness required by the study. This causes the numerical simulations to be run for a long time period in order to obtain representative data series. The numerical models with the finest grid were analysed over a 10-day period, deeming analyses for finer grids too time costly.

Chapter 2

Ship Resistance

Ship resistance is covered in the current chapter. The main focus is on a physical description of the important aspects in the current research.

2.1 Overview of Ship Resistance Components

Basic hydrodynamic resistance components of a ships total resistance are shown in figure 2.1, where the components are broken down into two main categories; pressure and friction. These two categories can further be described in how they act on the hull. Pressure resistance are forces acting normal on the hull surface, whereas friction forces are tangential shear forces on the hull.

A physical breakdown of the resistance forces according to Molland et al. (2011, pages 12-13) are:

Pressure resistance
Pressure forces acting on each element of the hull surface, which can be summed up over the hull to produce the total pressure resistance. Further, the pressure drag arises partly due to viscous effects and partly due to wave-making of the hull, as illustrated by figure 2.1.

Frictional resistance
Tangential shear forces acting on each element of the hull surface, which can be summed up over the hull to produce the total shear resistance or frictional resistance. This is a force that arises purely due to viscous effects.

Thus, the total resistance may be described by three components:
Total resistance = Frictional resistance + Viscous pressure resistance + Wave resistance

Further consideration of flow parameters, resistance coefficients, wave resistance and appendage resistance are made in the following text. Although it is possible to divide resistance into more categories, it is not seen as vital to go into great detail on for instance air resistance. A reason for this is that no superstructures that may considerably influence the air resistance are modelled in the present study. Moreover, the most important aspects of resistance for the study are - and will be - described.

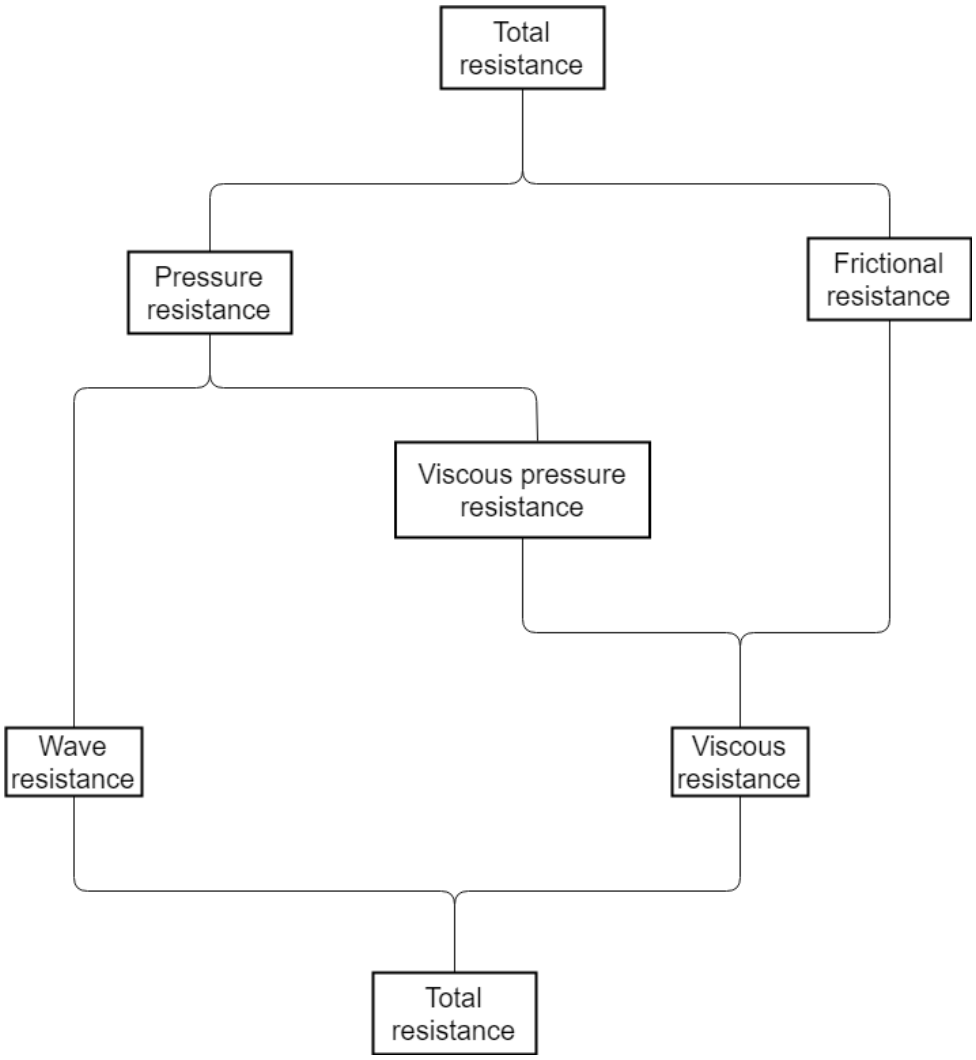

Figure 2.1: Basic hydrodynamic resistance components.

2.2 Flow Parameters and Resistance Coefficients

Equation 2.1 and 2.2 defines the Froude number and Reynolds number, respectively. The Froude number can be seen as a ratio of inertial force to gravitational force, whereas the Reynolds number gives a ratio between inertial and viscous forces (Çengel and Cimbala, 2014, table 7-5). Further, a Froude number less than about 0.5 implies that the ship is a displacement vessel such that the hydrostatic force carries the main part of the weight of the vessel (Faltinsen, 2005, page 1; Faltinsen, 1990, page 1).

The main factors influencing the flow can be characterised in terms of the Reynolds number and the Froude number (see for instance Larsson and Raven (2010, pages 11-12)). A high Reynolds number implies a turbulent flow, whereas a low Reynolds number a laminar flow. Most cases of practical interest are those of turbulent flows, meaning that the fluid particles following the flow exhibit a fluctuating behaviour that affects structures in the fluid and therefore also the frictional resistance. The Froude number is important when a free surface is considered as it appears in the free surface boundary condition (Larsson and Raven, 2010, page 11). It must be the same in model and full scale if the

effect of gravity on the free surface shall be correct in model testing (Larsson and Raven, 2010, pages 11-12). An equal Froude number in model and full scale will then give a geometrically similar wave pattern (Larsson and Raven, 2010, page 16; Steen, 2014, page 34).

$$Fn = \frac{U}{\sqrt{gL}} \tag{2.1}$$

$$Re = \frac{UL}{\nu} \tag{2.2}$$

Where,

L is a representative length. For instance length between perpendiculars, L_{pp}

g is the gravitational acceleration

ν is the kinematic viscosity

Equation 2.3 gives the non-dimensional resistance for an arbitrary resistance component, where the resistance component can be measured or calculated for instance by CFD. When appendages are included in resistance calculations, the wetted surface area of the appendage is calculated separately and added to the wetted surface area of the ship hull (ITTC, 2011b).

$$C_i = \frac{R_i}{\frac{1}{2}\rho S U^2} \tag{2.3}$$

Where,

C_i is an arbitrary resistance coefficient

R_i is a resistance component

ρ is the fluid density

S is the wetted surface area

U is the velocity of the body

The frictional resistance coefficient can be found using equation 2.4 if the viscous resistance, R_V, is known. In CFD the viscous resistance can be found by calculating the wall shear stress. However, when the viscous resistance is not known, the friction coefficient may be estimated by the ITTC-1957 correlation line given by equation 2.5 (ITTC, 2011b). Even though the correlation line is only an approximation it can be said to be a tolerable estimate for most hull forms (Molland et al., 2011, page 79).

$$C_F = \frac{R_V}{\frac{1}{2}\rho S U^2} \tag{2.4}$$

$$C_F = \frac{0.075}{(log_{10}(Re) - 2)^2} \tag{2.5}$$

Where,

C_F is the friction coefficient

R_V is viscous resistance

Re is the Reynolds number

2.3 Wave-making Resistance and Wave System

The subsequent text follows that of deep-water theory, considering that shallow water has significant effects on wave pattern (Molland et al., 2011, page 30). Wave-making resistance can be described by the resistance parameter, R_W, and its non-dimensional component, C_W.

Wave-making resistance, or wave resistance, is caused by the waves generated by a ship following a straight course with constant forward speed in calm water conditions (Faltinsen, 2005, page 38). Moreover, the wave-making resistance includes both the local wave elevation along the hull and the far-field waves.

Waves are generated because of pressure variations along the hull. The pressure variations changes the fluid level near a free surface such that waves are generated. Further, the waves need energy in order to be sustained. This energy is absorbed from the ship hull, which constitute a resistance force on the ship (Molland et al., 2011, page 12).

The wave system of a ship is mainly determined by the peaks of high and low pressure that occurs in the pressure distribution along the hull (Molland et al., 2011, page 29). Figure 2.2 illustrates how waves are generated depending on the pressure peaks, for which a crest is formed for positive peaks, and a trough for negative peaks.

Figure 2.2 further shows that the wave system is built up of four components:

- Bow wave system.
- Forward shoulder wave system.
- After shoulder wave system.
- Stern wave system.

The bow and stern wave systems will be dependant upon hull form and fullness. A fuller bow will for instance push the bow wave in front of the ship, whereas a very slender bow will have the bow wave located astern of the bow. The forward and after shoulder wave systems will be dependent upon hull form and position of the shoulders. More pronounced shoulders leads to clearer forward and after shoulder wave systems. Nevertheless, the principle remains the same. Assuming linearity, the superposition principle may be used on the wave components and the total wave system can be obtained.

In addition to the wave system being dependent upon hull form, it is also influenced by the forward speed of the ship. As speed is increased, the length of the waves will increase (Molland et al., 2011, page 31). This changes the phase between the individual wave systems. Thus, the total wave system changes with changing forward speed.

The interference of all the separate wave systems will constitute the ship wave pattern. Interference between wave components plays an important role; wave systems that amplify each other leads to a high wave resistance, whereas the opposite situation in which waves cancel each other corresponds to a low wave resistance (Larsson and Raven, 2010, page 31). At Froude numbers around 0.2 the wave pattern will tend to be fully developed, and the energy radiated by the transverse and stern waves becomes important (Larsson and Raven, 2010, page 33-34).

Figure 2.3 illustrates the bow and stern wave systems from a bird's eye view. The wave system created by a ship hull will consist of both divergent and transverse waves, which are also shown in figure 2.3.

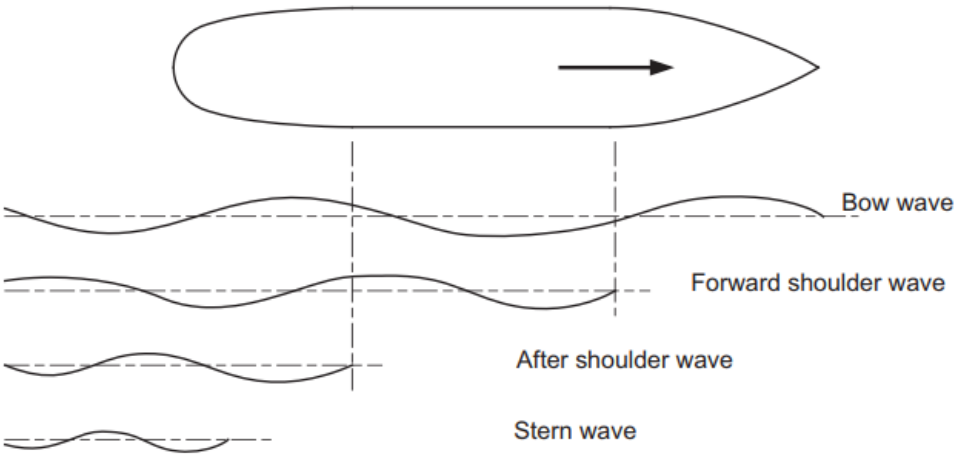

Figure 2.2: Wave system components (Molland et al., 2011, figure 3.15.).

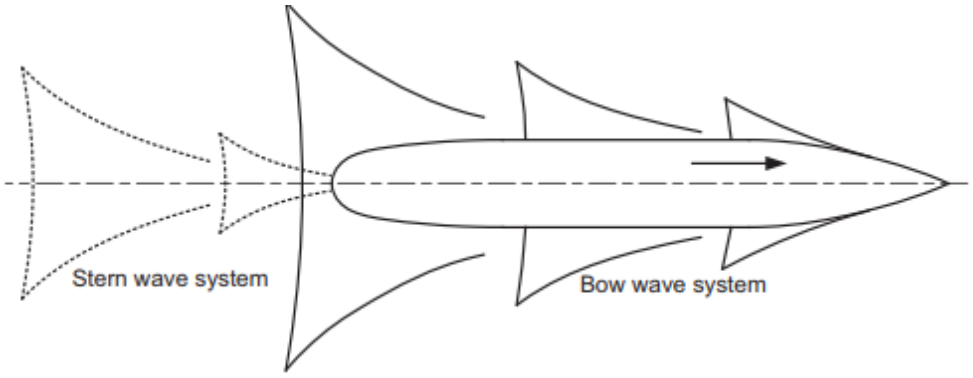

Figure 2.3: Wave system of a ship showing divergent and transverse waves (Molland et al., 2011, figure 3.13.).

Because group velocity is half the wave phase velocity, the wave energy does not stay with the crest but lags behind (Larsson and Raven, 2010, page 26). A consequence of this is that the crest will die out and a new crest is formed behind, which in turn will die out and have a new wave formed behind it. Thus, the wave crests do not extend indefinitely, but are short and arranged in a fan shaped pattern (Larsson and Raven, 2010, page 26). This is illustrated for a single pressure point travelling in a straight line over the surface of the

water in figure 2.4 and is called the Kelvin wave pattern. This pattern will be different for a ship due to interference of the individual wave systems (bow, stern, shoulder).

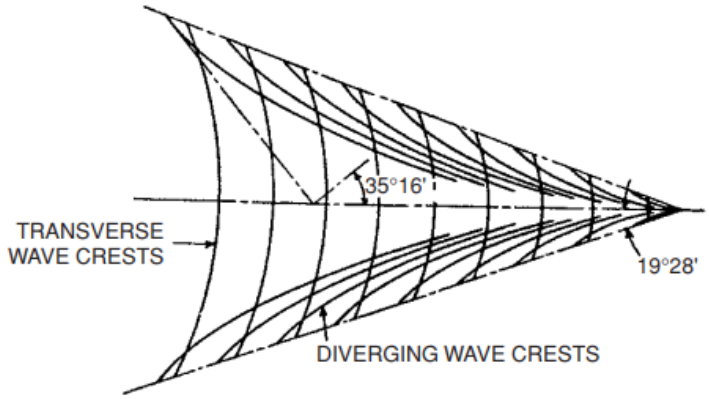

Figure 2.4: Kelvin wave pattern (Faltinsen, 2005, figure 4.3).

In order to reduce the wave-making resistance of a ship, it can be utilised with a bulb. The bulb will create a wave system that starts with a crest, because of the the high pressure region due to the stagnation point. The crest will be followed by a wave through, which will coincide with the hull's bow wave crest such that parts of the bow wave system is cancelled out. Best cancellation is obtained when the phase of the bulb generated wave is opposite to that of the bow wave and their waves amplitude is equal (Larsson and Raven, 2010, page 197). Abkowitz and Pauling Jr. (1953) argued that a hydrofoil at an angle of attack could serve as an anti wave-making device, following the principle that the low pressure region over the hydrofoil will create a wave trough aft of the hydrofoil that can cancel out bow wave systems. The longitudinal position of the hydrofoil is then an important aspect, such that the wave trough coincides with the bow wave crest. Also Naito and Isshiki (2005) discussed the importance of the longitudinal position of the hydrofoil from a calm water resistance point of view. They stated that the optimum position of the wing, that do not increase the total calm water resistance, has not been found (as of date published), and that further research must be done in this area to find it.

2.4 Appendage Resistance

Additional resistance on a ship can be caused by appendages such as rudders, stabilisers, bilge keels and so on. With careful alignment, the resistance due to appendages will result mainly from skin friction. However, bluff appendage bodies can cause flow separation and lead to a significant increase in resistance. If an appendage is located near a free surface, the appendage can cause an increase also in wave resistance (Molland et al., 2011, page 37).

To what extent wavefoils will create a wave resistance will depend upon vertical placement and foil configuration. Section 3.3 discusses the effect of a hydrofoil beneath a free surface to a larger extent. Further, there will be an additional frictional drag due to the foils, which will contribute to the total resistance. Depending on the magnitude of the

thrust force crated by the wavefoil, the total resistance of the ship may be affected either positively or negatively.

Chapter 3

Foil Theory

Relevant theory for foils are described in this chapter, where the main focus is on a physical description of relevant aspects for the current research.

3.1 Foil Terminology

Geometry of a three-dimensional foil is illustrated in figure 3.1. Here, c represents the chord length, s represents the span, and U is the incident flow velocity of the foil. In case the foil, represented by a straight line between the leading edge and trailing edge, has an angle relative to the inflow, there will be an angle of attack α. The aspect ratio of a rectangular foil is defined by equation 3.1.

$$Asp = \frac{s}{c} \tag{3.1}$$

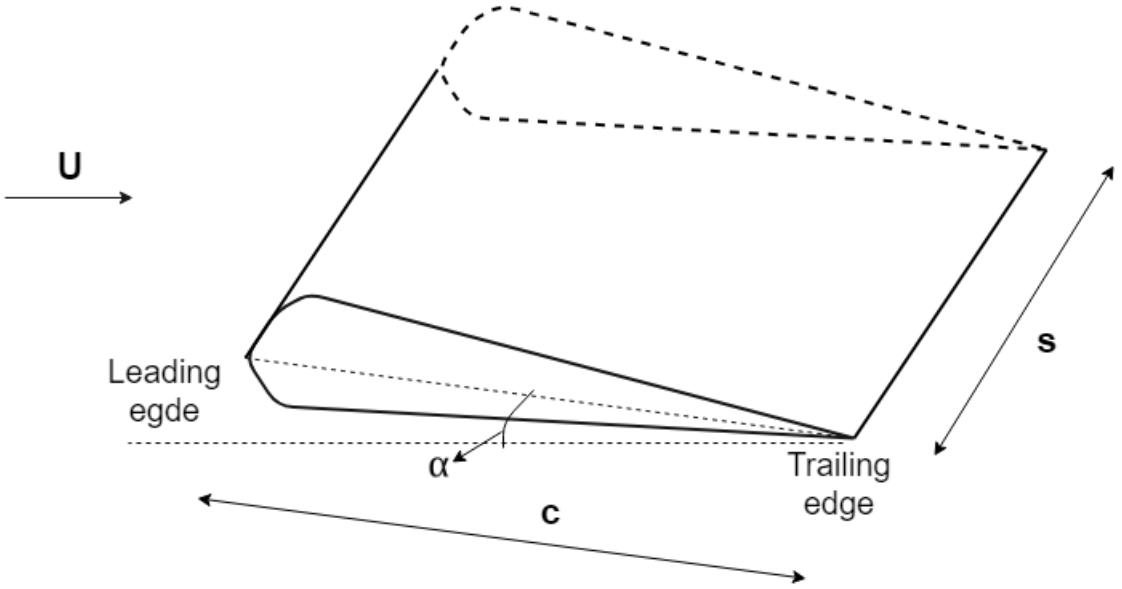

Figure 3.1: Foil geometry and definitions.

Another geometrical aspect of a foil, is the camber line. This is a line that represents the mean of the thickness at any given point on a foil cross-section. In case the camber line is a straight line between the leadin and trailing edges, as is the case in figure 3.1, the foil is said to be symmetric.

3.2 Forces and Force Coefficients

A hydrofoil in infinite, incompressible and inviscid fluid will not experience any drag force. This is known as D'Alembert's paradox, which says that there is no hydrodynamic force acting on a body in infinite fluid due to steady potential flow without circulation (Faltinsen, 2005, page 26). However, in real life viscous effects play an important role and will cause a viscous drag force on the hydrofoil. In addition, pressure drag forces can arise due to phenomena such as flow separation and vortex shedding.

The lift and drag forces acting on a foil can be made non-dimensional through equation 3.2 and 3.3, respectively.

$$C_L = \frac{F_L}{0.5\rho U^2 A} \tag{3.2}$$

$$C_D = \frac{F_D}{0.5\rho U^2 A} \tag{3.3}$$

Where,

C_L is the lift coefficient

C_D is the drag coefficient

F_L is the force in the perpendicular direction relative to the inflow, directed upwards

F_D is the force in in-line direction relative to the inflow

U is the free stream velocity, or inflow velocity on the foil

A is the projected area of the foil in lift direction for zero angle of attack

Further, the pressure forces F_L and F_D can be found from equation 3.4.

$$F_i = -\int_S p n_i dS \tag{3.4}$$

Where,

F_i is the force in direction i, for i = 1,2,3 corresponding to x-, y- and z-direction, respectively.

p is the pressure acting on the foil

n_i is the decomposed surface normal in the direction of the force, and positive pointing outwards from the surface

S is the foil surface area

The lift force on a hydrofoil can depend on many parameters, and a list for an individual hydrofoil can be found in Faltinsen (2005, page 168). One of the most important aspects that creates a lift force in the current research is the angle of attack, which creates a lift force crucial for achieving foil thrust and is discussed in section 3.4.

For a foil with angle of attack below stall angle and the Kutta-condition fulfilled (which says that the flow shall leave the trailing edge tangentially), viscous effects dominate the drag force. The viscous drag force arises due to friction, where the friction coefficient for a flat plate aligned with the flow can be estimated from equation 3.5 (Faltinsen, 2005, page 22). The wall shear stress, or frictional stress, will depend on the boundary layer being laminar or turbulent (see section 4.3). Hence, the total drag force on a foil will depend upon both pressure forces and viscous forces, such that total drag = pressure drag + viscous drag.

$$C_f = \frac{\tau_w}{0.5\rho U^2} \tag{3.5}$$

Where,

C_f is the friction coefficient

τ_w is the wall shear stress or frictional stress

Stall is a possible viscous effect on a hydrofoil and occurs if a critical angle of attack, for which below stall does not occur, is exceeded. The flow will then separate from the leading edge or near the leading edge, and the mean lift force on the foil will decrease relative to no flow separation (Faltinsen, 2005, page28). When stall occurs, viscous pressure resistance is important.

3.3 Hydrofoil Beneath a Free Surface

The presence of a free surface will influence a hydrofoil operating under it. Equation 3.6 defines the Froude number for a foil based on chord length. In practice, Froude numbers for a hydrofoil will be high and free surface effects will give a reduction in lift force. In a study by Xie and Vassalos (2007) it was found a reduction in lift force for decreasing submergence at Froude numbers equal to one and above. A reason for the reduction in lift force is the generation of free surface waves (Faltinsen, 2005, page 199). Other possible phenomena that can cause a reduction in lift force for a hydrofoil with high submergence Froude number (equation 3.7) and very small submergence are cavitation and ventilation (Faltinsen, 2005, page 200). For small Froude numbers, less than one, based on chord length the lift coefficient can increase with decreasing submergence. This was for instance reported in numerical studies by Karim et al. (2014) and Xie and Vassalos (2007).

$$Fn = \frac{U}{\sqrt{gc}} \tag{3.6}$$

For a submerged foil, the submergence Froude number is defined by equation 3.7, and it is also common to use the submergence to chord ratio, h/c, to generalise the results.

Further, submergence depth and chord length are defined as in figure 3.2.

$$Fn_h = \frac{U}{\sqrt{gh}} \tag{3.7}$$

Where,

Fn_h is the submergence Froude number

h is the submergence depth

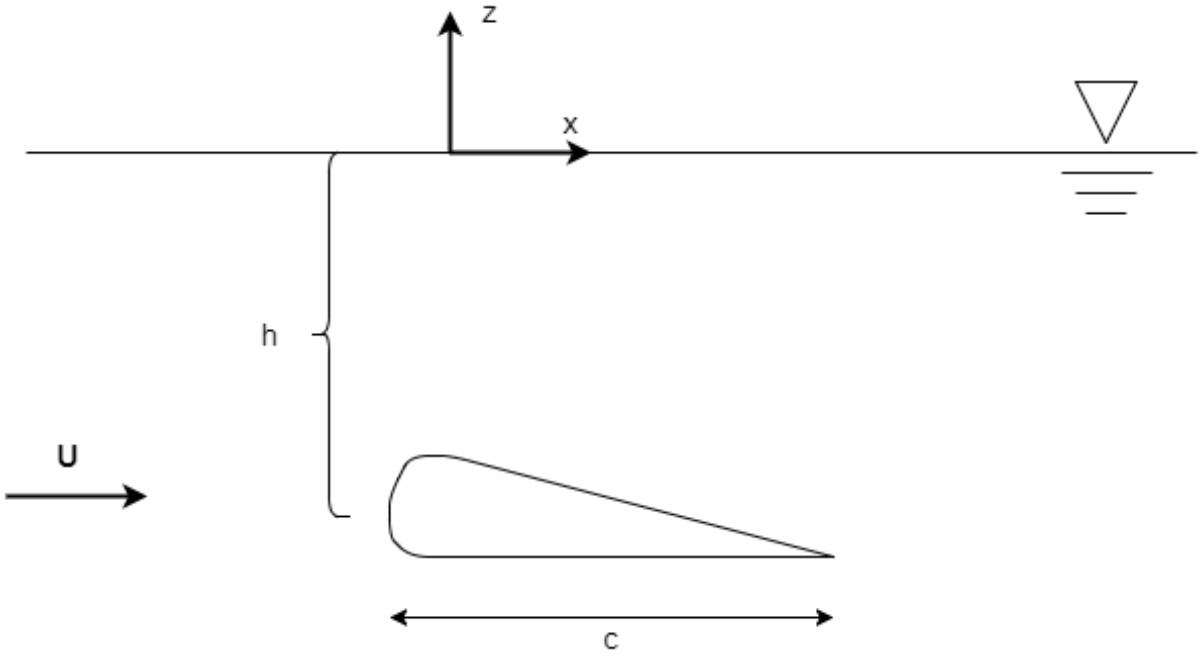

Figure 3.2: Illustration of a hydrofoil beneath a free surface.

A hydrofoil with forward speed, which travels beneath a free surface, will create surface waves if it is sufficiently close to the free surface. By use of linear theory, one can deduce that a hydrofoil generates free surface waves when the submergence Froude number is larger than approximately 0.4 (Faltinsen, 2005, page 199). When free surface waves are generated an additional resistance will arise, namely wave resistance. Both the lift and the thickness of a hydrofoil will cause wave resistance (Faltinsen, 2005, page 200).

Figure 3.3a and 3.3b shows drag force and wave resistance for a three-dimensional hydrofoil at different submergence depths presented by Faltinsen (2005, figure 6.52) and Xie and Vassalos (2007, figure 11), respectively. Faltinsen (2005) used a theoretical approach to find the drag, whereas Xie and Vassalos (2007) used a three-dimensional panel method to calculate the wave resistance. Both results show the importance of submergence depth on the wave resistance.

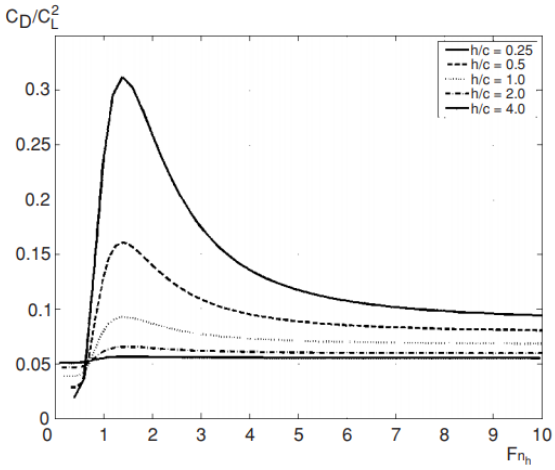

(a) Drag on a foil for different h/c ratios (Faltinsen, 2005, figure 6.52).

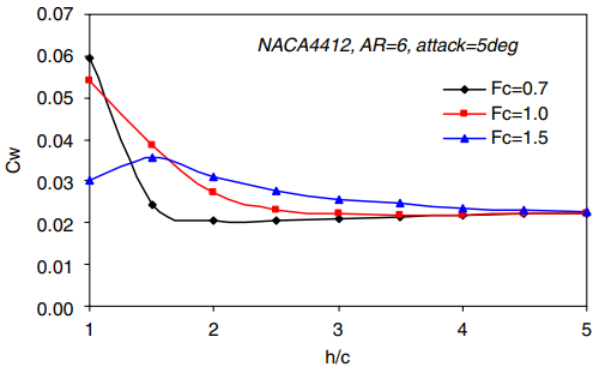

(b) Wave resistance on a foil for different Froude numbers and submergences (Xie and Vassalos, 2007, figure 11).

Figure 3.3: Drag and wave resistance on a hydrofoil with different submergence depths.

3.4 Foil Thrust

A foil can generate a thrust force, T, depending on the foil configuration and inflow. Figure 3.4 shows inflow from below (3.4a) and above (3.4b) for a horizontal and symmetric foil. Knowing that the lift force acts perpendicular to the inflow velocity vector (Faltinsen, 2005, page 188), the force can be decomposed into a vertical and horizontal component. The lift force and its horizontal component will have the same sign, proving a forward force known as foil thrust.

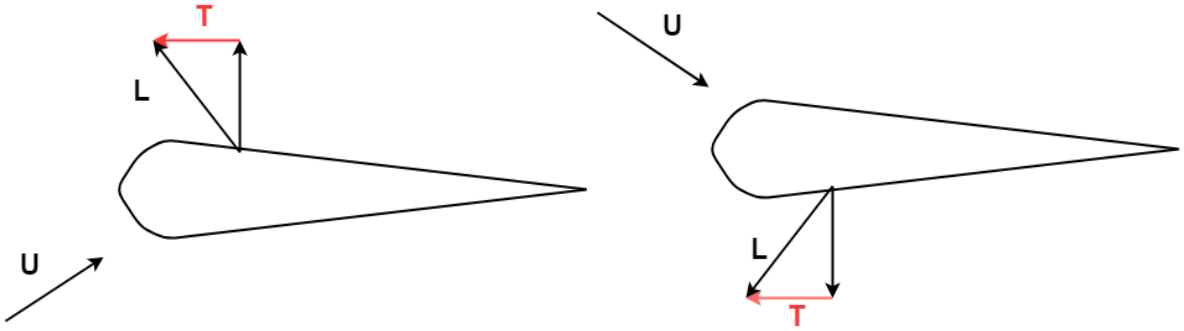

(a) Inflow attacking from below.

(b) Inflow attacking from above.

Figure 3.4: Thrust force, T, on a foil due to inflow with an angle.

As stated in section 3.2 there will be drag forces acting on a foil. Figure 3.4 does not include any drag force in the illustration, however, this will influence the effect of the foil thrust. Therefore, in order to obtain net thrust, the drag force must be smaller than the horizontal component of the lift force.

To achieve foil thrust, foils can be exposed to vertical motion that effectively gives an angle of attack. This can be done actively by a mechanical solution, or passively by letting foils follow the vertical motion of a ship. The latter is the principle utilised by

wavefoils. As a ship experiences heave and pitch motion, the inflow angle on the foils changes and a foil thrust can be achieved on horizontal foils.

Chapter 4

Mathematical Description of CFD

In this chapter, a mathematical description of the Navier-stokes equations are given. Additionally, turbulence and boundary layer theory are described. Parts of the work in the current chapter were carried out in the project thesis work during the autumn semester of 2017, but have been modified and extended for a more thorough description.

To solve a turbulent flow by direct numerical simulation (DNS) of the Navier-Stokes (NS) equations require that all relevant length scales are resolved. This imposes difficulties because the finer features of a turbulent flow field are always unsteady and three-dimensional. Further, turbulent eddies arises in all directions for a turbulent flow, where the length and time scales between the smallest and largest eddies can be several orders of magnitude. An increasing Reynolds number would further increase this difference, making DNS calculations even more difficult (Çengel and Cimbala, 2014, page 902-903). Thus, DNS simulations will require an extremely fine grid and small time step in order to solve all length and time scale, making such simulations extremely computational demanding and time consuming.

For engineering purposes a DNS simulation will be too costly and also available computer resources will limit the possibilities. Therefore, some simplifications can be made in order to reduce the computational efforts. One such possibility is the use of the Reynolds-averaged Navier-Stokes (RANS) equation, together with a turbulence model. Much of present-day design code development and computational research in turbulent flows is through the RANS equation (Pletcher et al., 2013, page 271). The RANS equation uses time averaging of the equations of motion, relating the flow problem to the mean flow. Due to the time averaging of the equations, additional terms arise in the NS equation. These additional terms can be interpreted as stress gradients associated with the turbulent motion, and must be related to the mean flow through a turbulence model (Pletcher et al., 2013, page 271).

4.1 Navier-Stokes and RANS Equations

Equation 4.1 and 4.2 gives the incompressible continuity equation and incompressible time dependent NS-equation, respectively. The time dependence is important when it comes to capturing transient flow phenomena, such as separation, vortex shedding and wakes.

For the present case it is reasonable to assume that the fluid is incompressible, i.e water can be considered to have constant density. If a free surface is considered, the air phase is also assumed to be incompressible. A reason for air to be considered as incompressible is that the velocities involved are small, much less than 100 m/s (Pletcher et al., 2013, page 249).

$$\frac{\partial u}{\partial x} + \frac{\partial v}{\partial y} + \frac{\partial w}{\partial z} = 0 \tag{4.1}$$

$$\rho \frac{D\vec{U}}{Dt} = -\vec{\nabla} P + \rho \vec{g} + \mu \nabla^2 \vec{U} \tag{4.2}$$

Where,

u, v and w are the velocity components in x-, y, and z- directions, respectively

$\vec{U}$ is the velocity vector containing the velocity components

∇ is the differential operator

t represents time

μ is the dynamic viscosity

Equation 4.3 shows how the velocity components and pressure in a turbulent flow can be decomposed into a time averaged and a fluctuating part, which is the Reynolds decomposition of turbulent quantities (Tennekes and Lumley, 1972). By definition, the time average of a fluctuating quantity is zero, however, the time average of the product of two fluctuating quantities will not necessarily be zero (Pletcher et al., 2013, page 272-273).

$$u = \overline{u} + u' \qquad v = \overline{v} + v' \qquad w = \overline{w} + w' \qquad p = \overline{p} + p' \tag{4.3}$$

Where,

$\overline{u}$, $\overline{v}$ and $\overline{w}$ are the time averages of the velocity components in x-, y- and z- directions, respectively

x', y' and w' are the fluctuating part of the velocity components

$\overline{p}$ is the time average of the pressure

p' is the fluctuating part of the pressure

Using the relations in equation 4.3, inserting them in the continuity equation and then taking the time average of the whole equation, will give the Reynolds-averaged continuity equation for an incompressible fluid (equation 4.4). Note that tensor notation is used, meaning that for a repeated index a summation is required.

$$\frac{\partial \overline{u}_j}{\partial x_j} = 0 \tag{4.4}$$

By utilizing the same procedure for the NS-equation, as for the continuity equation, the RANS equation is obtained for an incompressible fluid (equation 4.5) (Pletcher et al., 2013, page 276).

$$\frac{\partial}{\partial t}(\rho\overline{u}_i) + \frac{\partial}{\partial x_j}(\rho\overline{u}_i\overline{u}_j) = -\frac{\partial\overline{p}}{\partial x_i} + \frac{\partial}{\partial x_j}(\overline{\tau}_{ij} - \rho\overline{u_i'u_j'}) \tag{4.5}$$

Where,

$$\overline{\tau}_{ij} = \mu(\frac{\partial\overline{u}_i}{\partial x_j} + \frac{\partial\overline{u}_j}{\partial x_i}) \tag{4.6}$$

$\overline{\tau}_{ij}$ is the result of viscous stresses, whereas the term -$\rho\overline{u_i'u_j'}$ arises from turbulent stresses, or Reynolds stresses. The Reynolds stresses are new unknowns, and further equations are needed in order to solve the RANS equation.

4.2 Turbulence Model: k-ω SST

Two-equation models are commonly used to model the turbulent quantities in a turbulent flow. In a two equation model two new variables are solved by introducing two additional transport equations. The new transport equations must be solved simultaneously with the continuity and RANS equations. The two new variables are hence used to find, or model, the Reynolds stresses and the turbulent (eddy) viscosity.

Among the popular turbulence models is the k-ω SST (Shear Stress Transport) model. It combines the standard k-ε and k-ω models by rewriting both k and ε equations in terms of ω (Klein et al., 2014). The argument for combining both models are that the k-ω model is superior to the k-ε model in the boundary layer, but it fails for flows with pressure induced separation. In addition, the ω equation has been found to be sensitive to the free stream outside the boundary layer, whereas the ε is more stable in this region (Menter, Kuntz, et al., 2003). Thus, by combination, the best qualities of each model is used.

Transport equations for k and ω, using the model of Menter (2003), are given in equation 4.7 and 4.8, respectively (Menter, Kuntz, et al., 2003). The blending function involved governs the the switch between k-ε and k-ω models. Further, constants in the equations are also the result of blending, where the constants from the k-ε and k-ω models are used (Klein et al., 2014).

$$\frac{\partial(pk)}{\partial t} + \frac{\partial(\rho U_i k)}{\partial x_i} = \widetilde{P_k} - \beta^*\rho k\omega + \frac{\partial}{\partial x_i}[(\mu + \sigma_k\mu_t)\frac{\partial k}{\partial x_i}] \tag{4.7}$$

$$\frac{\partial(\rho\omega)}{\partial t} + \frac{\partial(\rho U_i\omega)}{\partial x_i} = \frac{\alpha\widetilde{P_k}}{\nu_t} - \beta\rho\omega^2 + \frac{\partial}{\partial x_i}[(\mu + \sigma_\omega\mu_t)\frac{\partial\omega}{\partial x_i}] + 2(1 - F_1)\rho\sigma_{\omega 2}\frac{1}{\omega}\frac{\partial k}{\partial x_i}\frac{\partial\omega}{\partial x_i} \tag{4.8}$$

Where,

k is the total turbulent kinetic energy

ω is the specific eddy dissipation rate

$U_i = \overline{u}_i$

$\widetilde{P_k}$ is the turbulent kinetic energy production rate

β, β^*, σ_k, σ_ω and $\sigma_{\omega 2}$ are constants

F_1 is a blending function used to determine if ε or ω is to be used. Is equal to one inside boundary layer, and zero away from the surface

μ_t and ν_t are the turbulent dynamic and kinematic viscosity, respectively

4.3 Boundary Layer Theory

It is important to fully understand the boundary layer, which is the flow region adjacent to the wall where viscous effects are significant (Çengel and Cimbala, 2014, page 9). Thus, the viscous force on a body is mainly due to the boundary layer. For turbulent flows the boundary layer will behave differently from that of a laminar. The main reason is the velocity fluctuations that occur in turbulent flows. In the following, the relations in equation 4.3 are used.

Now, letting x be parallel to the free stream, y normal to the wall surface, and assuming the boundary layer thickness, $\delta(x)$, is much smaller than the distance x. Furthermore, 2D is assumed. According to White (2006), we can do the following approximations in the boundary layer:

$$\overline{v} << \overline{u} \qquad\qquad \frac{\partial}{\partial x} << \frac{\partial}{\partial y} \tag{4.9}$$

This means that the perpendicular mean velocity component is much less than that in the parallel direction. We also have that the gradients, or changes, in the boundary layer are much greater in the perpendicular direction to the wall surface. Thus, in the boundary layer of a turbulent and compressible flow we now get that the continuity equation can be written according to equation 4.10, and the momentum equation in the x-direction according to equation 4.11 (White, 2006). These equations are in close relation to those describing the laminar boundary layer. However, the boundary layer shear stress has an additional term in form of a turbulent shear stress.

$$\frac{\partial \overline{u}}{\partial x} + \frac{\partial \overline{v}}{\partial y} = 0 \tag{4.10}$$

$$\overline{u}\frac{\partial \overline{u}}{\partial x} + \overline{v}\frac{\partial \overline{u}}{\partial y} \approx U\frac{dU}{dx} + \frac{1}{\rho}\frac{\partial \tau}{\partial y} \tag{4.11}$$

Where,

U is the free stream velocity when considering a fixed wall

ρ is the density of the fluid

τ is the boundary layer shear stress, and $\tau = \mu \frac{\partial \overline{u}}{\partial y}$ - $\rho \overline{u'v'}$

$\overline{u'v'}$ is the time average of the product of the fluctuating turbulent velocities, and is modelled by a turbulence model

Now, if the velocity profiles $\overline{u}$(x,y) for a turbulent flow are considered, it is found that that the profile consists of two layers (White, 2006). In addition there is an overlap layer, which is a transition between the two layers. The layers are defined as:

- Inner layer - viscous shear dominates
- Outer layer -turbulent shear dominates
- Overlap layer - both types of shear are important

This can further be related to the boundary layer shear stress according to equation 4.12. Thus, the viscous shear stress dominates in the inner layer, and the turbulent shear stress in the outer layer. Further, it is found that for the inner layer the velocity profile will depend upon wall shear stress, fluid properties and distance, y, from the wall. The outer layer will depend on wall shear stress, boundary layer thickness, distance from the wall and the free stream pressure gradient, which implies that the wall acts merely as a source of retardation, reducing the local velocity below the stream velocity. (White, 2006).

The wall shear stress can be defined according to equation 4.13. It is important to keep in mind that for a turbulent flow the velocity u must be interpreted as the time average on the time scale of turbulence of the total velocity component (Faltinsen, 2005, page 14). Therefore, both the mean and fluctuating velocity components must be included in equation 4.13 when considering turbulence.

$$\tau_l = \mu \frac{\partial \overline{u}}{\partial y} \qquad \tau_t = -\rho \overline{u'v'} \tag{4.12}$$

Where,

τ_l is the viscous shear stress

τ_t is the turbulent shear stress

$$\tau_w = \mu \frac{\partial u}{\partial y}|_{y=0} \tag{4.13}$$

4.3.1 Dimensionless Velocity Profiles: Law of the Wall

The velocity profiles in the boundary layer can be made dimensionless, where the dimensionless distance to the wall surface , y^+, and dimensionless boundary layer shear velocity, u^+, are defined as in equation 4.14. It can be shown that combination of the dimensionless inner and outer layers of a velocity profile will yield a logarithmic function for the overlap layer (White, 2006). The main advantage of using dimensionless functions is that, for a

non-separating flow, different velocity profiles can be described by a single mathematical relation for each layer.

$$y^+ = \frac{yv*}{\nu} \qquad u^+ = \frac{\overline{u}}{v*} \tag{4.14}$$

Where $v*$ is the wall friction velocity, which is related to the wall shear stress (equation 4.15).

$$v* = \sqrt{\frac{\tau_w}{\rho}} \tag{4.15}$$

Figure 4.1 shows the law of the wall. The region where $y^+ \leq 5$ is called the viscous sublayer, and it is found that the velocity profile has a linear behaviour in this region, with $u^+ = y^+$ (White, 2006). The flow in this region is not steady, however, viscous effects dominates, making the velocity fluctuations of secondary importance (Tennekes and Lumley, 1972).

For $5 \leq y^+ \leq 30$ we are in a buffer layer. Here the velocity profile is neither linear nor logarithmic, but there will be a smooth transition between the viscous sublayer and the logarithmic layer.

Equation 4.16 is the dimensionless velocity profile for the overlap layer based on the inner variables. This forms the basis of the logarithmic region, which is defined for $30 \leq y^+ \leq 100$. Here the overlap layer will dominate, such that both viscous and turbulent shear dominates. When $y^+ > 100$ the outer layer will rise above the overlap layer (White, 2006). Hence, the logarithmic expression for the overlap is no longer valid outside this region.

$$u^+ = \frac{1}{\kappa} ln(y^+) + B \tag{4.16}$$

Where,

κ is a constant determined experimentally

B is a constant determined experimentally

Experimental data shows that $\kappa \approx 0.41$ and $B \approx 5.0$ (White, 2006)

For engineering purposes in CFD, it can be advantageous to use logarithmic wall functions. These are based on the logarithmic region, and the viscous sublayer is with that neglected. A reason for this is to save computational time compared to a computational model in which the viscous sublayer is modelled. This means that the grid size near the wall surface must be much lower than that arising from the use of logarithmic wall functions - when considering the y^+ values involved. A premise for the utilisation of logarithmic wall functions is that the flow is fully turbulent, such that turbulent shear dominates over viscous, making the viscous sublayer of secondary importance. Lastly, the logarithmic law is found to be applicable for nearly all wall-bounded turbulent boundary layers, making logarithmic wall functions a powerful tool in CFD (Çengel and Cimbala, 2014, page 576).

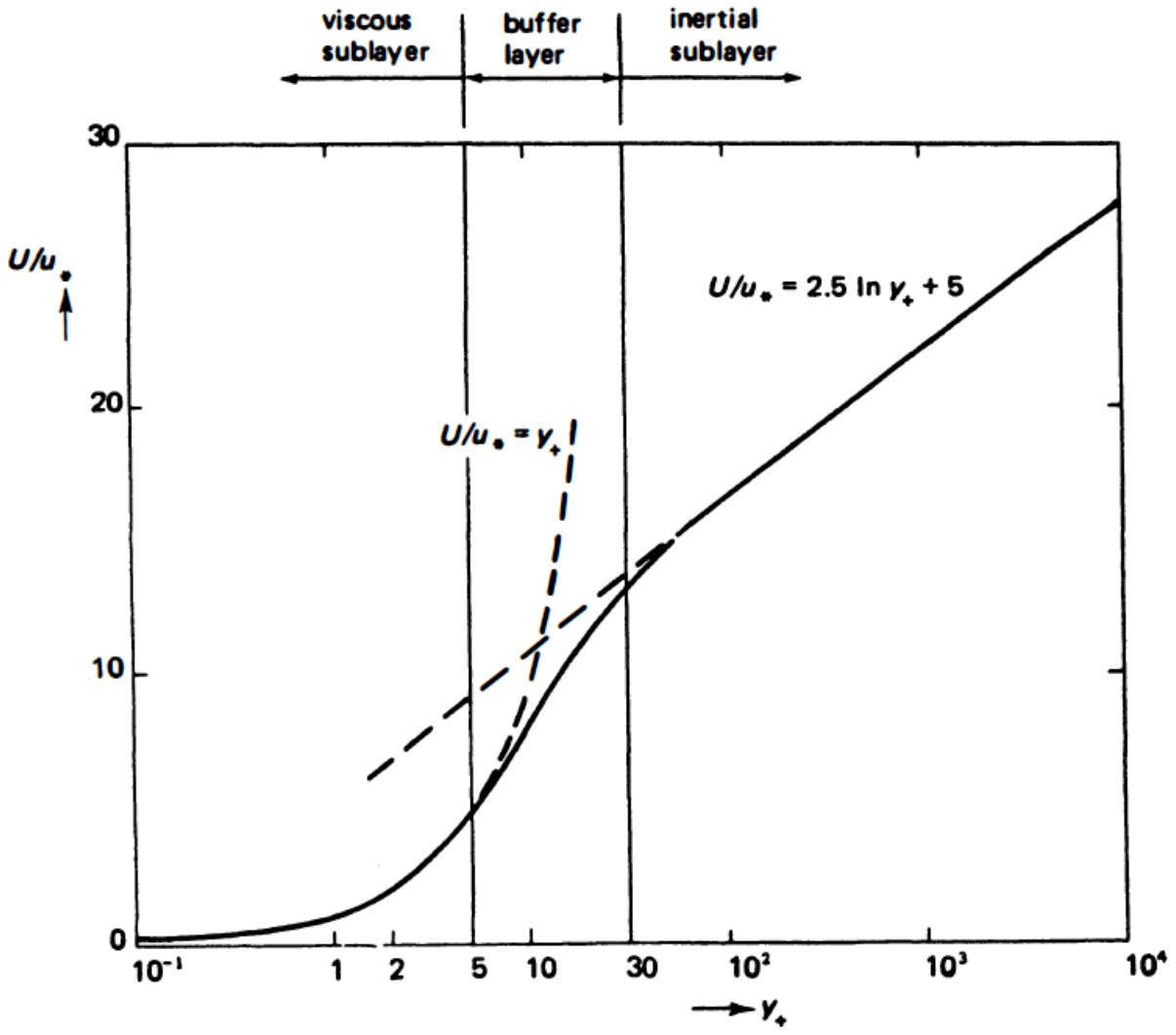

Figure 4.1: Illustration of the Law of the Wall (Tennekes and Lumley, 1972, figure 5.6).

Low Reynolds number, turbulent flows requires different handling than use of logarithmic wall functions. A reason for this is that the viscous sublayer will be of higher importance, hence, the logarithmic behaviour in the boundary layer will be violated. Spalding developed a formula that captures the wall region for both the viscous sublayer and the logarithmic region (equation 4.17) (Spalding, 1961; White, 2006). The requirement is that $y^+ < 5$, and preferably $y^+ = 1$ or less, in order to capture the viscous sublayer in numerical calculations. This means also that the grid near a wall must be finer than required by use of logarithmic wall functions, which will increase the computational time. Therefore, careful consideration of the flow problem is necessary. Logarithmic wall functions should be used when applicable, in order to be as computationally cost efficient as possible with respect to wall treatment.

$$y^+ = u^+ + e^{-\kappa B}[e^{\kappa y^+} - 1 - \kappa u^+ - \frac{(\kappa u^+)^2}{2} - \frac{(\kappa u^+)^3}{6}] \tag{4.17}$$

One of the reasons that the k-ω SST model is superior to the k-ε model in the boundary layer, is that the ω-equation provides analytical solutions for both the viscous sublayer

and the logarithmic region (Menter and Esch, 2001). A transitional value for ω can thus be found from a blending function depending upon y^+ (equation 4.18). By doing so, the model shifts gradually between a viscous sublayer formulation and wall functions, based on the grid density. (Menter and Esch, 2001). A major advantage with such a formulation is that one does not need to change how ω is treated near the wall.

$$\omega(y^+) = \sqrt{\omega^2_{viscous}(y^+) + \omega^2_{logarithmic}(y^+)} \tag{4.18}$$

Chapter 5

Numerical Method and Considerations

This chapter describes the software used in the analyses, methods connected to setting up an analysis and post-processing of it, numerical schemes and other aspects that are important to keep in mind when performing CFD.

5.1 OpenFOAM

The open source software OpenFOAM (Open Source Field Operation and Manipulation), which is published under the GNU General Public Licence, is used for the numerical simulations. More specifically, the version OpenFOAM v1612+ released by OpenCFD Ltd is used (OpenCFD Ltd, 2018a).

One of the advantages of OpenFOAM is that it comes with pre- and post-processing utilities, which, if utilised, reduces or completely eliminates the need of bringing in third-party software. A drawback can be said to be that there is no user interface in OpenFOAM. The program is run completely through the terminal, where files containing user specified information are read and subsequently used in the solving. Still, the procedure is not complex and becoming accustomed to the setup does not require much time. In addition, the software ParaView is distributed together with OpenFOAM, and is used for visualisation and post-processing such that the model can be viewed before and after solving.

Figure 5.1 show the necessary file structure of OpenFOAM. The system folder contains files specifying the solution algorithms, fvSolution, numerical schemes for differential terms, fvSchemes, and the controlling of the simulation, controlDict. The controlDict file specifies important aspects such as time step and how long the simulation should run. Further, OpenFOAM allows adjustment of the time step during the simulation. This can be beneficial as the simulation will run at the highest possible time step, while still satisfying stability by setting appropriate criteria.

All information of the user made mesh and specified boundaries are stored in the polyMesh folder, which in turn is located in the constant folder. Turbulence model and properties are further defined in the constant directory, in addition to fluid properties such as density and viscosity.

Time directories contains individually stored information about the flow field parameters for a simulated time. The information is written to files by OpenFOAM in a predefined interval, which must be appropriate with respect to both storing a sufficient amount of data for post-processing and, at the same time, not storing an unreasonable amount of data that only takes time and storage space. Simulations are started from an initial time directory, usually a 0-folder. Here, the initial and boundary conditions for the model are defined in accordance with the meshed model.

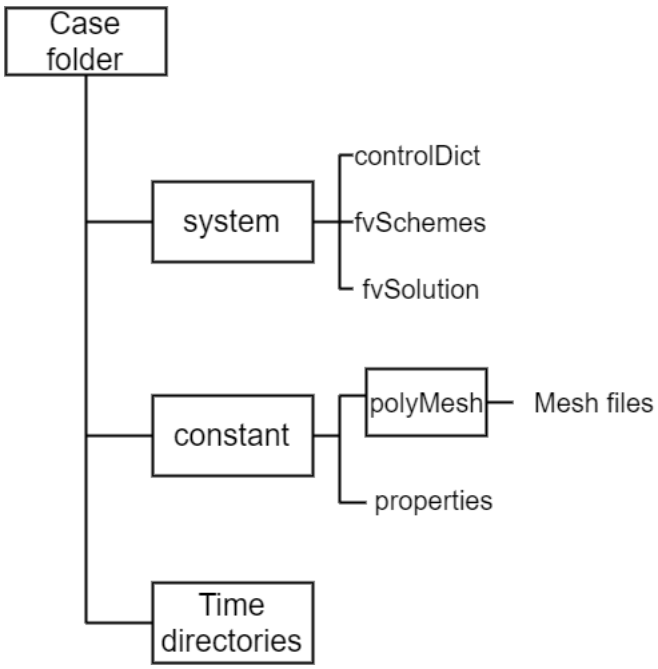

Figure 5.1: Overview of case file structure in OpenFOAM.

For running a complete analysis using OpenFOAM, seven steps can be identified:

1. Mesh and mesh implementation
2. Specifying fluid and turbulent properties
3. Specifying initial and boundary conditions
4. Selecting finite volume schemes and solver algorithm
5. Determining time domain and output intervals
6. Running analysis
7. Post-processing results

Where step two through five do not necessarily have to be performed in the given order. Further, steps one up until five are identified as the pre-processing of a numerical analysis.

5.2 Meshing

Setting up the computational grid is one of the first steps in CFD analyses. The physical domain must be filled with a mesh so that discrete volumes are identified where the

conservation laws can be applied (Pletcher et al., 2013, page 649). Care must be taken when creating the grid, as a well made mesh is important for the quality and convergence of the solution.

Creation of the computational grid is composed of two main steps. First, a background mesh is created using the blockMesh utility provided by OpenFOAM. Secondly, the mesh is refined in the appropriate areas, such as around the hull and free surface, with the snappyHexMesh utility, also provided by OpenFOAM. Further, refinement of the free surface needs additional steps that will be explained in more detail below.

The blockMesh utility produces three-dimensional hexahedral blocks in the computational domain, where each block is known as a cell in the computational domain (OpenCFD Ltd, 2018b). The size of the cells produced are equal, and all cells are isotropic with the reason being that snappyHexMesh works best with cells having an aspect ratio of one (OpenCFD Ltd, 2018b). The edge size of the cells produced with blockMesh will be known as the base size. It is important to produce a background mesh with an appropriate base size in order for snappyHexMesh to show compliance, such that an appropriate refinement level is reached.

SnappyHexMesh is used in order to mesh around the geometry and refine the mesh in the appropriate areas. The geometry is first read from a STL-file and the mesh is refined around the geometry for a number of levels specified by the user. For each level of refinement, a three-dimensional cell is split into eight new cells. Therefore, a high number of refinement levels can drastically increase the number of cells in the mesh. In addition, other areas of the domain can be refined by specifying regions of interest and refinement levels to be used in the wanted region. SnappyHexMesh then proceeds to snapping the mesh to the surface, i.e. fitting the mesh smoothly around the geometry. The last step in snappyHexMesh is adding layers to the geometry. These layers are composed of prismatic cells, aligned with the geometry surface, and are used to resolve the boundary layer.

The meshing method comprising of first using blockMesh to create the background mesh and then snappyHexMesh, as described above, works well for infinite fluid cases. However, when a free surface is involved, some extra steps are needed in order to refine the free surface region. The steps for meshing with a free surface in the thesis work can be summed up as follows:

1. Creating a background mesh with blockMesh.
2. Using snappyHexMesh to insert geometry, refine around geometry and other regions of interest by isotropic splitting of cells in all three dimensions.
3. Selecting the free surface region by using topoSet utility.
4. Refining mesh, based on the cells selected in topoSet, in vertical direction only using the refineMesh utility.
5. Snapping the mesh to the geometry surface and adding layers with snappyHexMesh.

Steps 3 and 4 are executed multiple times for achieving an appropriate free surface refinement. The cells are only refined in the vertical direction for capturing the free surface disturbance caused by the geometry. Additionally, the grid size in the horizontal plane around the free surface must be small enough for capturing the horizontal advection of fluid particles. This is achieved by isotropic refinement of the free surface using snappy-

HexMesh. Further, to ensure a uniform refinement along the free surface, the whole free surface area is selected using topoSet, and then deselecting cells of higher refinement level in the same topoSet-file based on volume.

As recommended by the ITTC (2014) guidelines, the grid is kept orthogonal for free-surface simulations. In order to dampen out ship generated waves for avoiding reflection at boundaries the cells are stretched, giving them a high aspect ratio and grid space, in the free surface region towards the boundaries (ITTC, 2011a; Piehl, 2016).

In the boundary layer, care is taken such that the cells closest to the wall will result in a non-dimensional distance to the wall in the range $30< y^+ <100$ when using logarithmic wall functions (ITTC, 2014a). If smaller y^+-values are needed, care is taken such that the non-dimensional distance is less than five and preferably equal to one (see section 4.3.1). Assuring appropriate y^+-values is achieved by controlling the layer-addition parameters in snappyHexMesh.

5.3 Initial Conditions for Turbulent Parameters

When using a turbulence model, initial values for the turbulent parameters must be calculated. For the k-ω SST model, initial values for k and ω can be determined through equation 5.1 and 5.2, respectively.

$$k = \frac{3}{2}(IU_\infty)^2 \tag{5.1}$$

$$\omega = \frac{\sqrt{k}}{\beta^{*0.25} l} \tag{5.2}$$

Where,

I is the turbulent intensity

$\beta^* = 0.09$ (Menter, Kuntz, et al., 2003)

l is a turbulent length scale

Estimation of the turbulent kinetic energy by equation 5.1 is well known within turbulent CFD, and is used in accordance with the application by Ong et al. (2009), Piehl (2016) and CFD Online (2014). Using equation 5.2 to estimate ω is also well known, and is given by CFD Online (2014). It can also be recovered in the source code of OpenFOAM.

For a ship flow where the fluid is at rest, except near the hull, the turbulent intensity can be taken to be less than 1% (Piehl, 2016). Further, the turbulent length scale can, according to Piehl (2016), be estimated as 1-10% of the beam of the ship hull when travelling with forward speed.

Based on the preceding, the values chosen for turbulent intensity and length scale in the thesis work are:

- $I = 0.5\%$

- $l = 1\%$ of ship beam

Proper estimation of the turbulent quantities is needed in order for a solution to converge as quickly as possible. If the estimates are much too high or low convergence takes a longer time, and if they are way off the solution may not converge towards the correct values at all. Therefore the values used in the analysis have been tested, and found acceptable for the convergence rate.

From the estimates of k and ω, the turbulent viscosity can be estimated. However, OpenFOAM allows for calculating the turbulent viscosity based on the input parameters, such that no estimation of turbulent viscosity is needed.

5.4 OpenFOAM Numerical Solvers and Algorithms

OpenFOAM offers a variety of different solvers that can be suitable for various problems. In the current research the simpleFoam solver is used for the double body case and the interFoam solver is used for all analyses involving a free surface.

5.4.1 simpleFoam

The simpleFOAM solver is based on the semi-implicit method for pressure linked equations (SIMPLE) algorithm, and is a steady-state solver for incompressible, turbulent flow (The OpenFOAM Foundation, 2017). A description of the procedure of the SIMPLE algorithm can according to Pletcher et al. (2013, page 643) be the following steps:

1. Guess the pressure at each grid point.
2. Solve the momentum equations to find the velocity components.
3. Solve a pressure-correction equation to find a corrected pressure at each grid point.
4. Correct the pressure and velocity according to given equations.
5. Replace the previous intermediate values of the pressure and velocity with the new corrected values. Step 2 through 5 are repeated until the solution converges.

The simpleFoam solver is used for the double body analysis as a free surface is not involved and a steady state solution is sought. The convergence of the simpleFoam solver can be decided by user specified tolerance limits, where simpleFoam will iterate until the tolerance limits for each flow parameter is reached.

5.4.2 interFoam

The interFoam solver is applicable for two incompressible, isothermal and immiscible fluids using a volume of fluid (VOF) phase-fraction based interface capturing approach (The OpenFOAM Foundation, 2017). Further, the solver uses the PIMPLE algorithm, which is a merge between the SIMPLE and pressure-implicit with splitting of operators (PISO)

algorithm. A description of the PISO algorithm can be the following steps (Pletcher et al., 2013, page 645-646):

1. Predictor step, where the pressure field prevailing at time level i is used in the implicit solution of the momentum equations.
2. First corrector step, where a new pressure field is sought along with a revised velocity field that will satisfy conversation of mass.
3. Second corrector step, where the pressure field and velocities are revised again.
4. More corrector steps can be made in the same way as step two and three. However, it is argued that only two corrector steps are sufficient for for most purposes (Issa, 1985).

The main principle of the PIMPLE algorithm will then be (Holzmann, 2018, pages 95-96): A steady-state solution is search within one time step, and once found - based on user specified tolerance limits - the algorithm moves on in time. Outer correction loops are applied to ensure that explicit parts of the equations converges, and within each outer correction loop there are corrector loops that corresponds to the corrector steps in the PISO algorithm.

The benefit of merging the SIMPLE and PISO algorithms into the PIMPLE algorithm, is that one can use larger time steps and still achieve stability in the numerical simulations (Holzmann, 2018, page 95).

For modelling the interface between water and air, interFoam uses the VOF method. It gives a phase fraction, "alpha.water", based on the two phases water and air in each cell, where:

- alpha.water = 1 if water
- alpha.water = 0 if air

5.4.3 Specific Solvers for Flow Parameters and Discretisation Schemes

For solving the pressure, the geometric-algebraic multi-grid (GAMG) solver is used. The principle behind is to generate a quick solution on a mesh with a small number of cells, and mapping the solution onto a finer grid; using the first solution as an initial guess. Using the GAMG solver has been proven to be faster than other solvers, as long as the computational cost outweighs the time it takes for refining the mesh (The OpenFOAM Foundation, 2017) Lastly, velocity and turbulent quantities are solved for using Gauss-Seidel method. It is one of the most efficient and useful point-iterative procedures for a large system of equations (Pletcher et al., 2013, page 152).

When it comes to discretisation schemes, robustness and accuracy is considered. A linear upwind method is used for discretisation of divergence terms for the velocity and the turbulent parameters. The linear upwind method is a second-order, upwind-biased, unbounded method that requires discretisation of the velocity gradient to be specified (The OpenFOAM Foundation, 2017). In the steady-state analyses, using simpleFoam,

boundedness is considered, with the linear upwind method being specified to be bounded. The reason for this is that it promotes better convergence (The OpenFOAM Foundation, 2017).

In steady state analyses the time derivatives are set to zero. However, in the transient analyses, using interFoam, the time derivatives are discretised using Euler discretisation. This is a first order and implicit method (The OpenFOAM Foundation, 2017).

Files that specifies the solver algorithms and discretisation schemes can be found in appendix A and B, respectively.

5.5 Stability

In numerical calculations it is essential to ensure numerical stability. If the calculations are numerically unstable, they will not converge towards the correct results and a simulation may crash.

For simulations described in this report, the time dependent NS-equation is solved. Therefore time integration is performed numerically, and stability must be preserved in order for the results to converge. The stability criterion that have to be satisfied is the Couran-Friedrichs-Lewy (CFL) condition, which is formulated in equation 5.3 (Pletcher et al., 2013, page 88). Here, Δt is the time step and Δx is the local element size in one dimension.

$$CFL = u\frac{\Delta t}{\Delta x} \tag{5.3}$$

By interpreting the CFL equation, it can be said that it gives the movement of a fluid particle over a number of cells per time step.

For explicit differentiation schemes, this number should be kept below unity. However, when implicit differentiation schemes are used for the divergence terms of the velocity, the CFL condition can be higher (ITTC, 2014a). The reason is that implicit schemes can tolerate that a fluid particle moves over more than one cell during a time step. However, care must be taken. A too large CFL number may still yield an unstable solution.

As discussed in section 5.4, the interFoam solver (which is based on the PIMPLE algorithm) is implicit, and can therefore tolerate CFL numbers that are larger than one. A time step sensitivity analysis in terms of the CFL number is performed in order to maintain stability in the numerical analyses.

5.6 Forces in OpenFOAM

OpenFOAM is able to calculate forces for each solid surface individually. Thus, the forces can be calculated for the ship hull and wavefoils separately. Moreover, OpenFOAM divides the total force into two components; pressure resistance, R_P, and viscous resistance, R_V. The sum of these two force components constitute the total resistance, R_T.

The pressure resistance calculated by OpenFOAM is made up of two parts. One is the resistance due to wave-making, and the other is a viscous pressure resistance component (El Moctar, Sigmund, et al., 2017).

5.7 Error Sources in Numerical Modelling and Solving

Presented below are main sources of error in numerical modelling and solving. It is important to understand that for a numerical procedure errors will be present in the final solution. One must be aware of the different types of errors and understand them in order to asses the validity of the numerical solution. In addition, understanding the error sources can be helpful in setting up the problem, such that the best possible groundwork is laid down and available theory is put into the model.

Round-off Error

This type of error is related to the computer which the simulations are run on. A computer deals with a finite number of digits, where numerical calculations may require an infinite number of digits for accuracy. Therefore, a computer round off to the nearest number it can deal with. In CFD, many millions of calculations may be performed. An initial small calculation error due to rounding may accumulate and invalidate the results.

Truncation Error

Truncation error is the error made in numerical analyses when an infinite sum is truncated to a finite sum. This is for instance applicable if a Taylor expression is used in the numerical approximation, i.e. partial derivatives are expressed as a Taylor series. The truncation error will further be the difference between the true solution and the solution obtained from the finite difference representation of the equation. In order to ensure a small truncation error, stability and consistency conditions must be met. Consistency is related to the mesh of the numerical problem. Subsequent reductions in mesh size will reduce the truncation error, and thus the solution will converge towards the true solution. Therefore, a mesh independence study is important to perform in order to find convergence towards the true solution.

Discretisation Error

The difference between the exact solution of the partial differential equation and the exact solution of the discrete representation (without round-off error) is the discretisation error. It follows that discretisation error is due to discretisation of the problem.

Modelling Error

An exact mathematical model of all physical flow phenomena is in general not available. Simplifications are done in order to explain a complex problem mathematically. For instance, the RANS-equations together with the k-ω SST turbulence model represents a modelling error, as flow parameters are related to the mean flow and the turbulence is modelled. Hence, the modelling error can be said to be the difference between the actual flow and the mathematical model.

5.8 Computational Resources

CFD can require a lot of memory usage and processor power in order to work with reasonable accuracy and time limits. Both the meshing procedure and running analyses require a lot of memory, whereas the processor power is needed for speed in the calculations. Therefore, when considering complex and large systems a normal laptop will not be sufficient for numerical calculations.

Two computational resources have been available and used in the research described in this report. The first is a work station with 16 cores and 64GB of RAM. The second is a high-performance cluster named Vilje. The main specifications of Vilje are given in table 5.1 (NTNU HPC Group, 2018).

The work station has been used for all meshing procedures, which is due to the convenience of easy inspection of the computational grid locally on the computer. Further, the double body analysis using simpleFoam is run on the work station.

All analyses involving a free surface are run on the high-performance cluster Vilje, which is needed in order to speed up the calculations. The mesh is divided over the processor cores in use, such that cells per core are in the range 80 000 - 100 000. This results in a computational time of 5 - 10 seconds for each time step.

Table 5.1: Specifications of Vilje.

Number of nodes	1404
Processors per node	2 eight-core processors per node
Processor speed	2.6GHz
Cores per node	16
Memory	2GB per core/ 32GB per node

Chapter 6

Ship Model and Numerical Models

In this chapter, the ship model and hydrofoil geometry used in the numerical analyses are described together with a description of the different domains used in the analyses. Further, boundary conditions imposed on the computational domains are stated and their function explained.

All the models are in model scale. This is due to the available reference data also being for model scale. Therefore, the model is appropriately Froude scaled so that the waves are correctly scaled and so is the resistance component caused by the wave generation (Larsson and Raven, 2010, page 12). Hence, the wave pattern created by the model ship hull should be similar to that of the full scale ship.

Table 6.1 gives the fluid properties that are used in the numerical analyses. The properties for water are consistent with the model resistance tests described in section 6.1. The density of air is simply set equal to one when applicable, with a reason being that the air resistance is not given any considerations in the analyses and the effect of air resistance will be small as no superstructure is included in the ship model. Kinematic viscosity for air is chosen for a temperature between 15 and 20 degrees Celsius (Faltinsen, 2005, table A.2).

Table 6.1: Fluid properties and gravitational acceleration used in analyses.

	Water	Air
ρ [kg/m^3]	998.8	1
ν [m^2/s]	1.090×10^{-6}	1.48×10^{-5}
g [m/s^2]	9.81	9.81

6.1 Ship Model: Duisburg Test Case

The model ship used in all the numerical analyses is the Duisburg Test Case (DTC) hull. It is a modern 14000 twenty-foot equivalent post-panamax container carrier, developed at the Institute of Ship Technology, Ocean Engineering and Transport Systems (El Moctar, Shigunov, et al., 2012). Further, the model is chosen due to the availability of reference data, both experimental and numerical, in addition to having the model geometry easily available in OpenFOAM.

Table 6.2 gives the main dimensions and loading conditions for the DTC hull in model and full scale: length between perpendiculars L_{pp}, waterline breadth B_{wl}, draught midships T_m, block coefficient C_B, wetted surface under waterline at rest S_w and design speed U_{design}.

Results of resistance model tests for two forward speeds for the DTC hull are listed in table 6.3 (El Moctar, Shigunov, et al., 2012). The friction coefficient in table 6.3 is found using the ITTC-1957 correlation line, and the frictional resistance is obtained based on this correlation line. Lastly, the results for the two model speeds are used as reference data for the numerical analyses performed in the study.

Table 6.2: Main dimensions of DTC hull in design loading condition (El Moctar, Shigunov, et al., 2012, table 1).

	Model	Full Scale
L_{pp} [m]	5.976	355.0
B_{wl} [m]	0.859	51.0
T_m [m]	0.244	14.5
Trim angle [°]	0.0	0.0
V [m^3]	0.827	173467.0
C_B [-]	0.661	0.661
S_w [m^2]	6.243	22032.0
U_{design} [knots]	3.224	25
U_{design} [m/s]	1.668	12.86

Table 6.3: Results of resistance model tests DTC hull (El Moctar, Shigunov, et al., 2012, table 4).

U [m/s]	Fn [-]	$Re \times 10^{-6}$ [-]	R_T [N]	R_F [N]	$C_T \times 10^3$ [-]	$C_F \times 10^3$ [-]	$C_W \times 10^4$ [-]
1.602	0.209	8.783	28.99	24.554	3.623	3.069	3.660
1.668	0.218	9.145	31.83	26.431	3.670	3.047	3.360

6.2 Double Body Model

Figure 6.1 shows the domain used for the double body analysis with dimensions and patch names where boundary conditions have to be specified. The dimensions are well within the ITTC (2014a) guidelines.

Further, the hull is cut horizontally at the design water line, T_m, in order to achieve a double body analysis. The ship hull is then mirrored about the waterline and wave-making is neglected (see for instance Faltinsen (2005, pages 25-26)). Furthermore, the ship hull is cut along its longitudinal centre plane making use of a symmetry constraint. The reason for this is that only forward speed is considered, and by using port-starboard symmetry the number of cells in the mesh can be cut in half. This is in accordance with the ITTC (2014b) guidelines.

Boundary conditions for all patches are specified in table 6.4 with the same names as in OpenFOAM. In addition to imposing a symmetry condition on the still water line and

centre line of the ship, this kind of condition is used on the far field boundaries side and bottom. A reason for this is to ensure no outflow on the boundaries. Logarithmic wall functions are used for the turbulent quantities on the hull surface as described in section 4.3.1, and initial conditions for the turbulence are set in accordance with section 5.3. For the hull surface, a fixed value specifying zero flow velocity is imposed to ensure a no-slip condition.

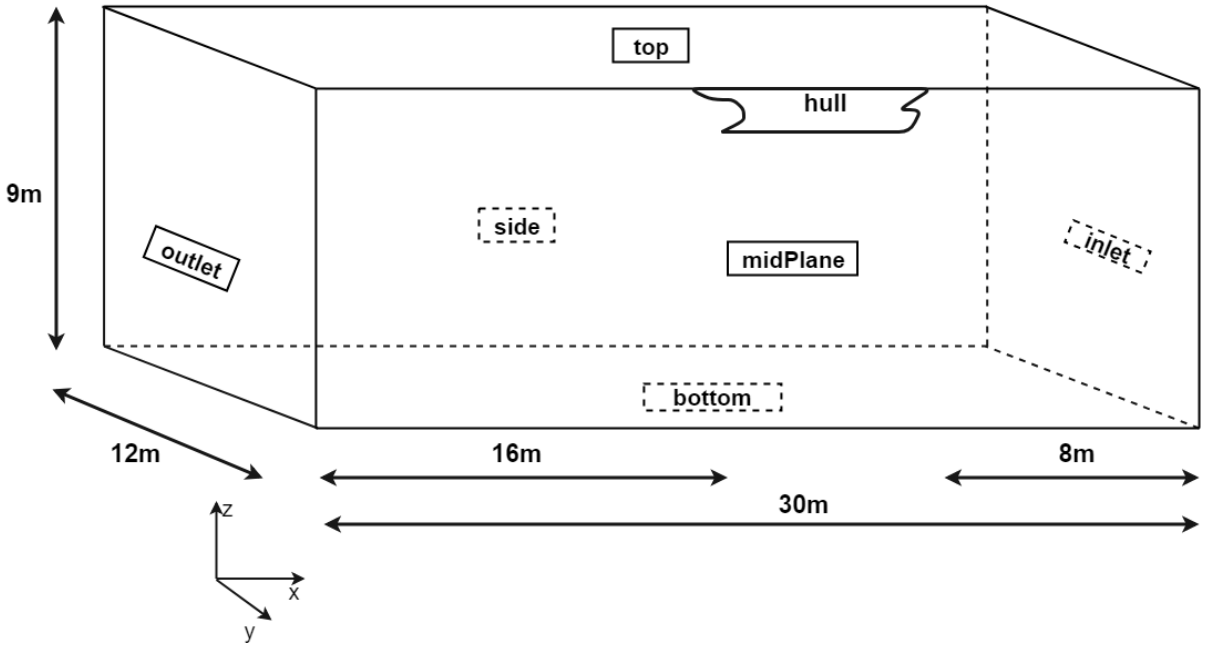

Figure 6.1: Computational domain used in the double body analysis.

Table 6.4: Boundary conditions used in double body analysis.

Parameter/Patch	U	p	k	ω	ν_t
inlet	fixedValue	zeroGradient	fixedValue	fixedValue	calculated
outlet	inletOutlet	fixedValue	inletOutlet	inletOutlet	calculated
top	symmetryPlane	symmetryPlane	symmetryPlane	symmetryPlane	symmetryPlane
bottom	symmetryPlane	symmetryPlane	symmetryPlane	symmetryPlane	symmetryPlane
side	symmetryPlane	symmetryPlane	symmetryPlane	symmetryPlane	symmetryPlane
midePlane	symmetryPlane	symmetryPlane	symmetryPlane	symmetryPlane	symmetryPlane
hull	fixedValue	zeroGradient	kqRWallFunction	omegaWallFunction	nutkWallFunction

6.3 Bare Hull With Free Surface Model

The computational domain used for the free surface analyses is shown in figure 6.2. Domain dimensions are set in accordance with the ITTC (2011a) and ITTC (2014a) guidelines, and there should be no interference from the bottom and side boundaries on the flow field. The whole hull is modelled without any superstructures, and the still water line is illustrated with the blue line. In the numerical analyses the draught of the ship is kept constant with T_m=0.244 metres, meaning that the ship is restrained from motion in all degrees of freedom.

Imposed boundary conditions on the system are listed in table 6.5. It is made use of symmetry about the centre line of the ship in the same manner as in the double body

model. The atmosphere boundary, however, requires different handling than for the double body model when both phases, water and air, are modelled. A slip boundary condition is imposed on the far field boundaries, bottom and side, and implies zero shear. The slip condition is used in accordance with the study of Shariati and Mousavizadegan (2017), who studied an underwater vehicle near the free surface.

Logarithmic wall functions are used on the hull patch for the turbulent quantities, with initial values specified according to section 5.3. Additionally, a fixed value of zero speed is imposed on the hull surface so that the no-slip condition is satisfied on the hull surface.

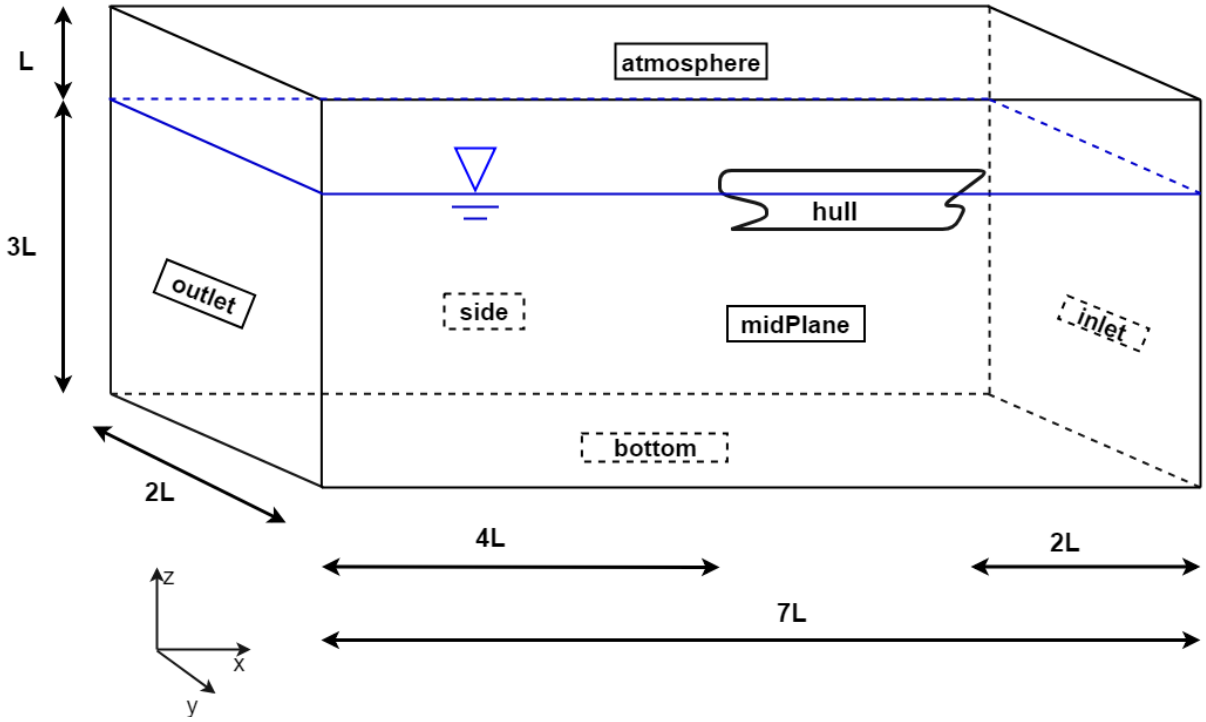

Figure 6.2: Computational domain used in the free surface analyses.

Table 6.5: Boundary conditions for free surface bare hull model.

Parameter/Patch	U	p_rgh	alpha.water	k	ω	ν_t
inlet	fixedValue	fixedFluxPressure	fixedValue	fixedValue	fixedValue	calculated
outlet	outletPhase MeanVelocity	zeroGradient	variableHeight FlowRate	inletOutlet	inletOutlet	calculated
atmosphere	pressureInlet OutletVelocity	totalPressure	inletOutlet	inletOutlet	inletOutlet	calculated
bottom	slip	slip	slip	slip	slip	slip
side	slip	slip	slip	slip	slip	slip
midePlane	symmetryPlane	symmetryPlane	symmetryPlane	symmetryPlane	symmetryPlane	symmetryPlane
hull	fixedValue	fixedFluxPressure	zeroGradient	kqRWallFunction	omegaWallFunction	nutkWallFunction

6.4 Hull With Wavefoil Model

The same computational domain that is used in the free surface bare hull analysis is used for the analysis including the wavefoil, with the only difference being an additional patch for the wavefoil - namely foil. Table 6.6 lists the boundary conditions for the model. The boundary conditions concerning the turbulent quantities on the foil patch are for a low

Reynolds number flow, and based on the formula by Spalding described in section 4.3.1. The reason for using wall functions based on the Spalding formula is the need of a high grid resolution around the hydrofoil, which results in small non-dimensional distances to the wall.

Table 6.6: Boundary conditions for hull with wavefoil model.

Parameter/Patch	U	p_rgh	alpha.water	k	ω	ν_t
inlet	fixedValue	fixedFluxPressure	fixedValue	fixedValue	fixedValue	calculated
outlet	outletPhase MeanVelocity	zeroGradient	variableHeight FlowRate	inletOutlet	inletOutlet	calculated
atmosphere	pressureInlet OutletVelocity	totalPressure	inletOutlet	inletOutlet	inletOutlet	calculated
bottom	slip	slip	slip	slip	slip	slip
side	slip	slip	slip	slip	slip	slip
midePlane	symmetryPlane	symmetryPlane	symmetryPlane	symmetryPlane	symmetryPlane	symmetryPlane
hull	fixedValue	fixedFluxPressure	zeroGradient	kqRWallFunction	omegaWallFunction	nutkWallFunction
foil	fixedValue	fixedFluxPressure	zeroGradient	kLowReWallFunction	omegaWallFunction	nutUSpalding WallFunction

Dimensions of the wavefoil used in the analyses are given in table 6.7. The foil is rectangular with a NACA 0018 profile, and no angle of attack relative to the undisturbed flow field is given. A script by Strandenes (2012) is used in order to generate the foil, with small adjustments to the script to make the foil fitting for the current case. Additionally the NACA 0018 profile is modified to have a sharp trailing edge (Strandenes, 2012; Airfoil Tools, 2018)

Table 6.7: Dimensions of wavefoil.

c [m]	0.1165	$= 0.0195 \times L_{pp}$
s [m]	0.3007	$= 0.7 \times B_{wl}/2$
h [m]	0.1740	
h/c [-]	1.494	
Asp [-]	2.58	

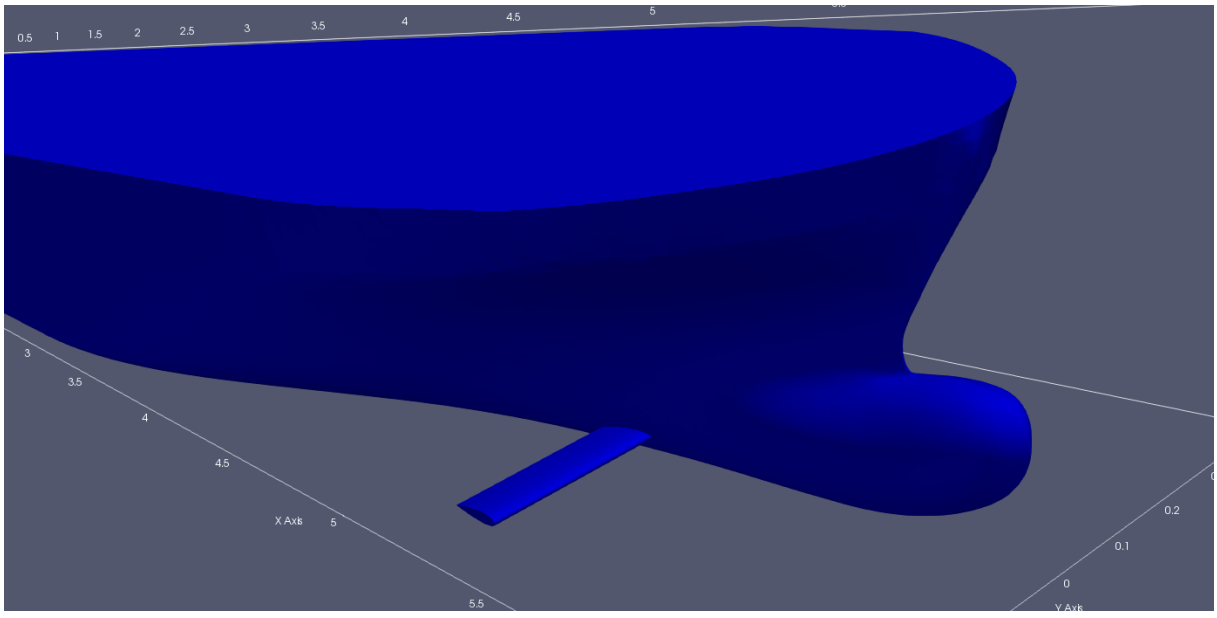

Figure 6.3: Ship hull with wavefoil attached.

Both the dimensions and the positioning of the wavefoil are decided together with the co-supervisor for the current research. The positioning of the wavefoil can be viewed in figure 6.3, with specifications:

- Longitudinal position: The leading edge is placed at a distance x = 5.45 metres forward of the stern.
- Transverse position: The wavefoil intersects the hull at y = 0.07 metres from the longitudinal centre line.
- Vertical position: The mean line is placed at a distance z = 0.07 metres above the base line of the ship hull.

6.5 Explanation of Boundary Conditions

An explanation of the boundary conditions follows below, and is based on descriptions by OpenCFD Ltd (2018b, section A.4). Additional comments are added where it is felt necessary or where no description is given by OpenCFD Ltd (2018b, section A.4).

calculated
No special constraint is set on the flow parameter when using this boundary condition. Instead, it is calculated based on other flow parameters at the same boundary.

fixedFluxPressure
This is a gradient condition for the pressure, where the gradient is user specified. For a value of zero, a zero gradient condition is applied and the flux over the boundary is determined entirely by the velocity.

fixedValue
This boundary condition sets a fixed value on the patch when used. It can for instance be used for a uniform inflow, and to impose a no-slip condition on surfaces by specyfying zero velocity

inletOutlet
In principle, this boundary condition is the same as setting a zero gradient. However, it can be said to be a stronger condition based on the fact that it can handle return flow. Therefore, the user can specify if return flow is allowed or not, and what values to use if return flow occurs.

kLowReWallFunction
Specifies the wall treatment of the turbulent kinetic energy to include the viscous sublayer.

kqRWallFunction
Specifies the wall treatment of the turbulent kinetic energy to be in the logarithmic region.

nutKWallFunction
Specifies the wall treatment of the turbulent kinematic viscosity to be in the logarithmic region.

nutUSpaldingWallFunction
Specifies wall treatment of the turbulent kinetic viscosity to include the viscous sublayer,

using the equation by Spalding for the non-dimensional distance to the wall (equation 4.17).

omegaWallFunction
Specifies wall treatment of specific eddy dissipation rate, ω.

outletPhaseMeanVelocity
Used at the outlet. The mean velocity of the flow is specified in order to obtain equal flux of mass flow rate out of the domain as into the domain.

pressureInletOutletVelocity
Applied to boundaries where the pressure is specified, i.e. the atmosphere boundary. It imposes a zero gradient condition for outflow.

slip
The slip condition is essentially a symmetry condition. It implies that there is no shear force and no flow through the boundary, and that the velocity at the boundary is parallel to the boundary.

symmetryPlane
A condition than ensures symmetry about the boundary. It is used to ensure that no outflow occurs along the boundary.

totalPressure
Sets the static pressure at the boundary based upon a specification of the total pressure. Used for a boundary that borders to the atmosphere.

variableHeightFlowRate
Used for the phase fraction, alpha.water. It allows for a varying water height at the outlet, which is needed when surface waves are created.

zeroGradient
When used, a zero gradient is applied for the parameter over the boundary. This means that no change over the boundary is desired, i.e. the flow parameter is constant at the boundary.

Chapter 7

Results and Discussion

Results for all analyses are presented in this chapter. The results are discussed and compared with relevant reference data and studies where possible. Lastly, all numerical analyses and results are for calm water conditions.

7.1 Double Body Analysis

The double body analysis have been performed for learning the ways of snappyHexMesh, and to validate the frictional resistance on the ship hull. Results of a mesh independence study on the double body model are shown in table 7.1. It can be seen from the table that a various grid density together with a varying number of layers have been used. The reason for this is to find the effect of grid resolution in and around the boundary layer of the hull on the viscous resistance.

Figure 7.1a shows convergence of the viscous resistance for the mesh with 1 817 181 cells. The simpleFoam solver ends the iterations when the residuals have converged to a value of 1×10^{-6} or below. Further, figure 7.1b shows the frictional coefficient based on the calculated R_V, and the frictional coefficient based on the ITTC-1957 correlation line.

The non-dimensional distance to the wall for the mesh with 1 817 181 cells is shown in figure 7.2. It can be seen from the figure that the non-dimensional distance to the wall is well within the logarithmic region for almost the whole hull. Only the bow region and parts of the stern region lies outside the logarithmic region. Therefore, due to most parts of the hull being in the logarithmic region, the use of logarithmic wall functions for the present case can be said to be correct.

Table 7.1: Mesh independence study double body analysis, Fn = 0.218.

Number of cells	R_V [N]	$C_F \times 10^3$ [-]	y^+_{avg} [-]	Number of layers [-]	Layer expansion rate [-]
1 407 484	24.78	2.86	28.1	5	1.5
1 684 156	24.53	2.83	46.0	4	1.2
1 817 181	24.41	2.81	52.8	5	1.15
2 302 367	24.65	2.84	45.2	9	1.1

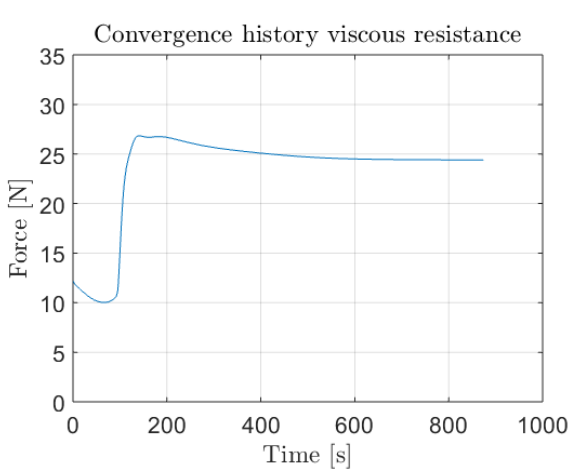

(a) Convergence of viscous resistance.

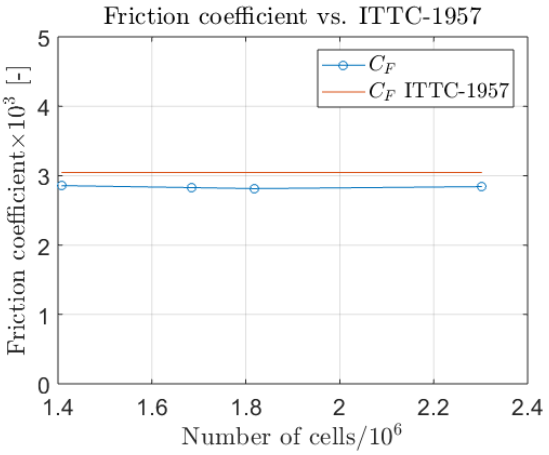

(b) Calculated friction coefficient vs. ITTC-1957 correlation line.

Figure 7.1: Viscous resistance convergence and friction coefficient for double body mesh independence study, Fn = 0.218.

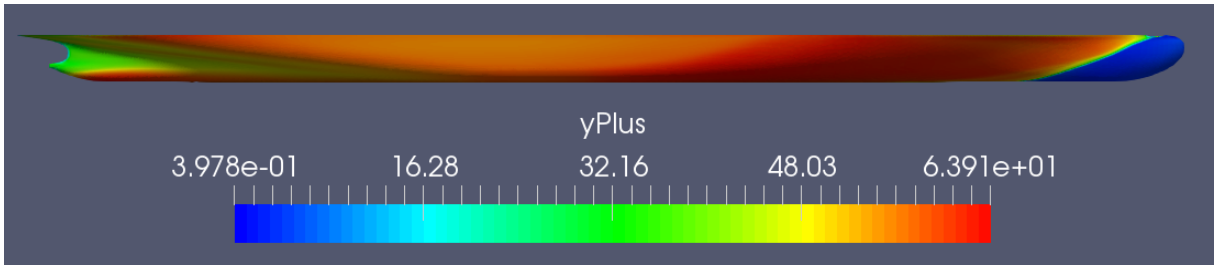

Figure 7.2: Non-dimensional distance to the wall, y^+, on ship hull surface for mesh with 1 817 181 cells.

From table 7.1 and figure 7.1b it can be seen that the mesh density does not have a large effect on the viscous resistance. This agrees well with the results of El Moctar, Sigmund, et al. (2017, figure 3), who also plotted the frictional resistance coefficient together with the ITTC-1957 correlation line. Additionally, both the result in figure 7.1b and the result by El Moctar, Sigmund, et al. (2017, figure 3) calculates a frictional coefficient which is slightly below $3{\times}10^{-3}$. Thus, the ITTC-1957 correlation line can be said to overestimate the frictional resistance in both cases. However, it is important to remember that the ITTC-1957 correlation line is only an estimate and that it dates back to 1957. Therefore, it may not be the best estimate for modern hull forms.

When considering a double body flow, the form factor, k, may be found from equation 7.1. The reason for this is that there is no wave resistance in the double body analysis, and that there are no appendages causing additional resistance in the present case. For the grid with 1 817 181 cells the total resistance is 26.51N, which gives a form factor k=0.086.

$$1 + k = \frac{R_T}{R_V} \tag{7.1}$$

El Moctar, Shigunov, et al. (2012) performed the same double body study to find the form factor with the result k=0.094 in model scale. This gives a relative difference of -8.5% when compared to the form factor calculated in the current case. It is possible that the form factors are found for different Froude numbers, as El Moctar, Shigunov, et al. (2012) do not state the value for which they found the form factor, which may explain the difference in results. Furthermore, a Froude number less than 0.15 may have resulted in a more appropriate form factor when comparing to El Moctar, Shigunov, et al. (2012). This is because the wave resistance tends to zero for low Froude numbers (Steen, 2014, page 9), and even though wave resistance is not included in a double body analysis a high Froude number may have some impact on the results. Thus, it is possible that the model should have been tested at a lower Froude number with respect to finding the form factor.

7.2 Bare Hull With Free Surface Analysis

7.2.1 Mesh Independence Study

A mesh independence study on the DTC bare hull, including a free surface, have been performed for Fn=0.218. Used mesh parameters can be seen in table 7.2. The wake is properly refined over a distance of 2L aft of the ship hull, using a refinement level of three. Resistance results can be found in table 7.3. Figure 7.3 shows convergence of the total and viscous resistance. The convergence of the pressure resistance and residuals may be found in appendix C.1 and C.2, respectively.

Table 7.2: Mesh parameters for mesh independence study.

	Base size [m]	Refinement levels [-]	Number of layers [-]	Layer expansion ratio [-]	Relative final layer size [m]
Mesh 1	1.0	7	5	1.25	0.7
Mesh 2	0.75	7	5	1.2	0.75
Mesh 3	0.50	7	5	1.1	0.7

Table 7.3: Resistance results for mesh independence study of bare ship hull, Fn = 0.218.

	Number of cells	R_T [N]	R_V [N]	R_P [N]
Mesh 1	2 262 732	28.40	24.47	3.93
Mesh 2	4 202 056	28.72	24.64	4.08
Mesh 3	10 708 305	28.79	24.84	3.95

Figure 7.3 shows that the forces oscillate, with oscillations gradually becoming smaller. The oscillations will eventually die out if the simulations are run for a longer period of time than what is presented. However, this will take an unnecessary amount of time, and it can be seen that the oscillations converge towards the mean value in figure 7.3. This is especially evident in figures 7.3a and 7.3b. From figure 7.3 one can also see that the oscillations die out faster for coarser grids. The reason for this may be that an increasing cell size causes numerical damping, and that the ship generated waves are dampened out more quickly with larger cell sizes.

In order to account for oscillations of the forces, the resistance components are found by taking the arithmetic mean over the last 70 seconds of the numerical analysis. This results in a relative difference of total resistance from experiments (table 6.3) of:

- Mesh 1: 10.78%
- Mesh 2: 9.77%
- Mesh 3: 9.55%

Results in table 7.3 indicate that the resistance is reasonably stable for the three grids. It is considered that there is no point in increasing the mesh resolution even further as this will most likely only result in time consumption.

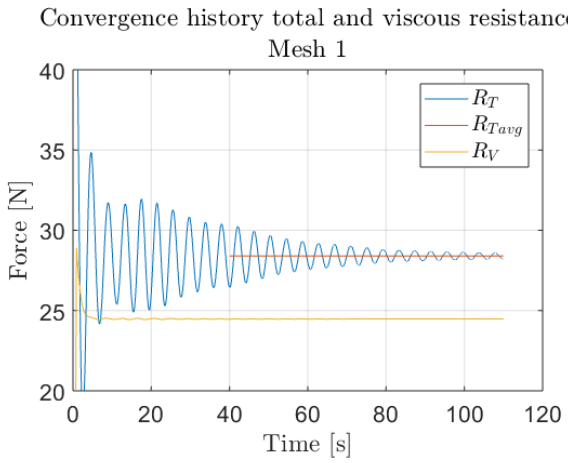

(a) Mesh 1.

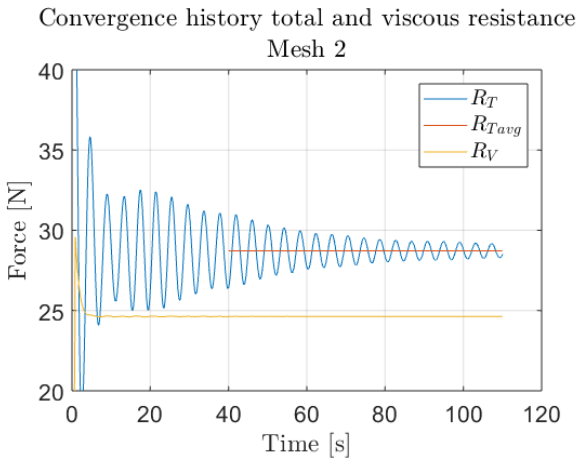

(b) Mesh 2.

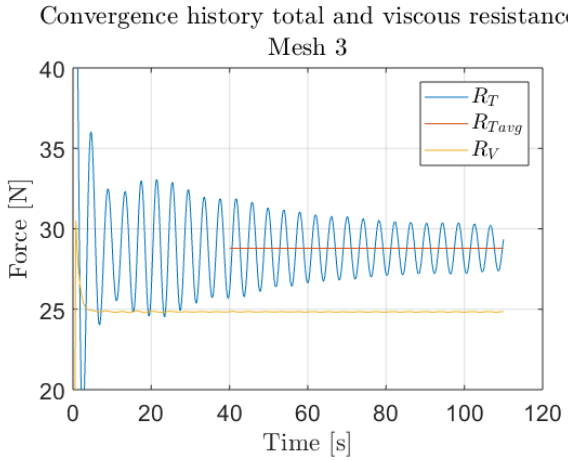

(c) Mesh 3.

Figure 7.3: Convergence of total and viscous resistance for mesh independence study of bare hull analysis, Fn = 0.218.

The deviation of the calculated results from the model tests may be explained by that the ship is fixed in the numerical analyses. The effect of sinkage and trim is therefore not accounted for in the present study, which may cause the resistance to be underestimated. However, it should be possible to come closer to the experimental results. El Moctar, Sigmund, et al. (2017) achieved a relative difference of 4.12% to experimental results and

Piehl (2016) a difference of 4.4%. Both used a fixed ship and underestimated the total resistance. Further, it is not believed that it is the mesh that is the cause of the difference in results when comparing to El Moctar, Sigmund, et al. (2017) and Piehl (2016). El Moctar, Sigmund, et al. (2017) used for instance 809 839 cells, a much lower grid resolution than in the present study. It is believed that El Moctar, Sigmund, et al. (2017) and Piehl (2016) comes closer to the experimental results due to modifications to the OpenFOAM source code, which is supported by the fact that El Moctar, Sigmund, et al. (2017) have used a modified version of the interDyFoam solver. Hence, the mesh resolution is viewed as sufficient and the resistance would likely come closer to the experimental results if the effect of sinkage and trim had been accounted for.

Figure 7.4 shows the non-dimensional distance to the wall for all three grids used in the mesh independence study. It can be seen that the wetted surface of the hull are within the requirements for using logarithmic wall functions.

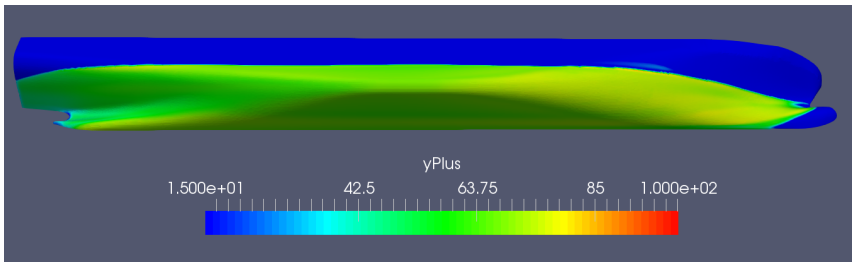

(a) Mesh 1.

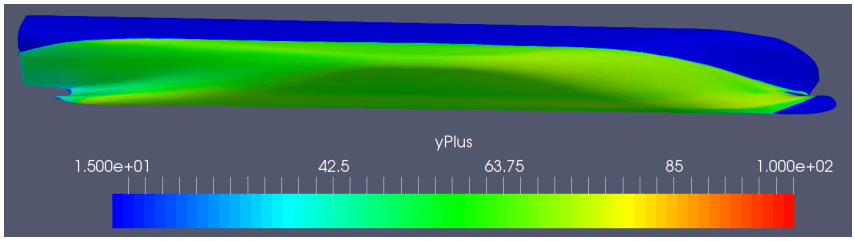

(b) Mesh 2.

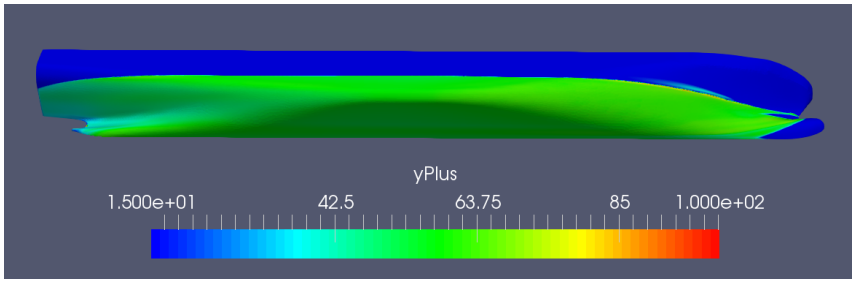

(c) Mesh 3.

Figure 7.4: Non-dimensional distance to the wall, y^+, on ship hull for the mesh independence study, Fn = 0.218.

7.2.2 Time Step Study

A time step study have been performed in order to test the sensitivity of the results to the time step. Because OpenFOAM allows for an adjustable time step, the study is performed in terms of the maximum CFL number. Further, the study is performed on mesh 1 and 2, where mesh 3 is omitted due to the stable results of the mesh independence study and the time consumption related to the large amount of cells in mesh 3.

Table 7.4 shows resistance results for the two meshes and the maximum CFL condition used. Figures 7.5 and 7.6 shows the convergence of the total and viscous resistance, where the convergence of the pressure resistance and residuals may be found in appendix C.3 and C.4, respectively.

The convergence of the resistance components are viewed to be stable with the exception of the result for mesh 2 with a maximum CFL number of 20. Figure 7.6a shows that the numerical simulation is unstable, and a large drop in the resistance is observed. Also, a maximum CFL number of 20 caused the simulation on mesh 1 to crash due to instabilities. The difference in total resistance for mesh 1 is 0.04N. For mesh 2, neglecting the result for maximum CFL = 20, the difference is 0.09N. Therefore, halving the time step can be said to give little effect on the results, and running simulations with a maximum CFL number of 10 is considered to be sufficient.

Table 7.4: Resistance results for time step study of bare hull analysis, Fn = 0.218.

	Max CFL [-]	R_T [N]	R_V [N]	R_P [N]
Mesh 1	10	28.40	24.47	3.93
Mesh 1	5	28.36	24.49	3.87
Mesh 2	20	25.50	21.30	4.20
Mesh 2	10	28.72	24.64	4.08
Mesh 2	5	28.81	24.76	4.05

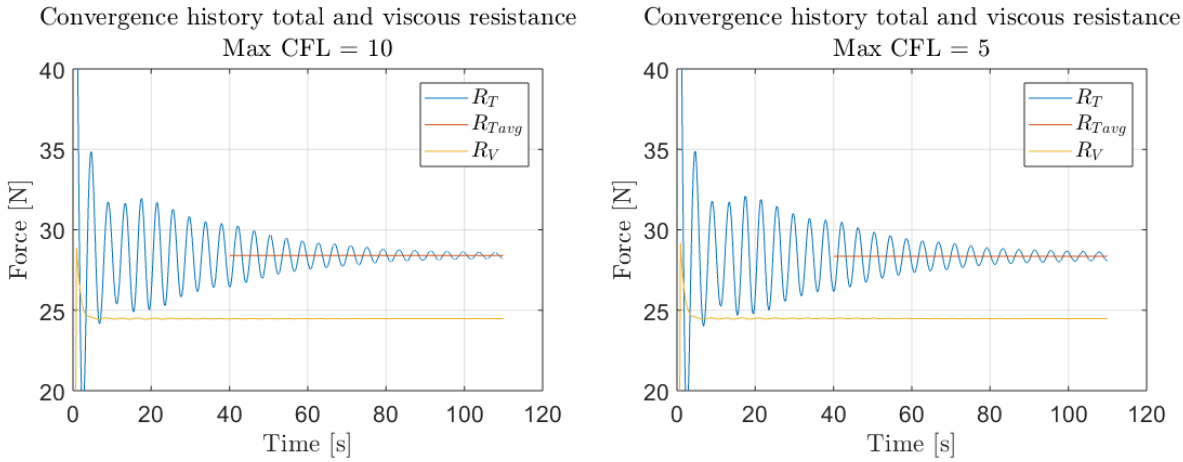

(a) Mesh 1, max CFL = 10.

(b) Mesh 1, max CFL = 5.

Figure 7.5: Convergence of total and viscous resistance for time step study on mesh 1 of bare hull analysis, Fn = 0.218

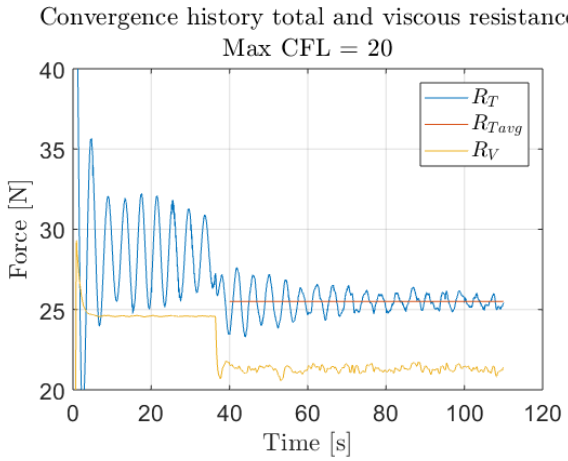

(a) Mesh 2, max CFL = 20.

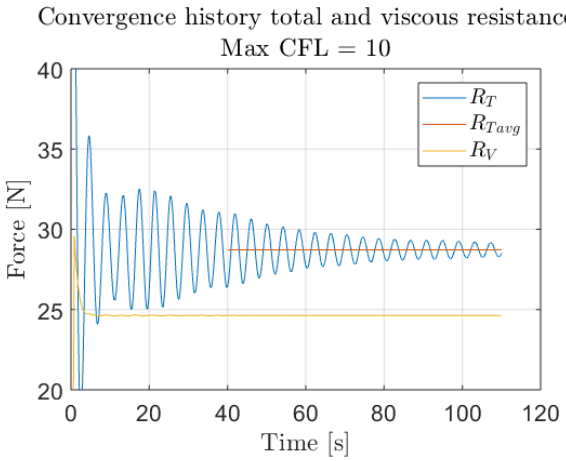

(b) Mesh 2, max CFL = 10.

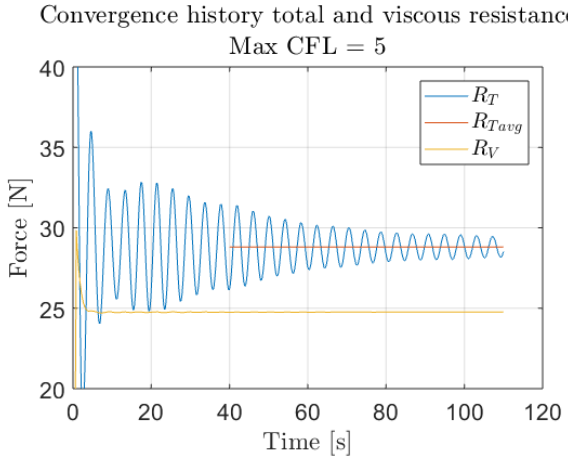

(c) Mesh 2, max CFL = 5.

Figure 7.6: Convergence of total and viscous resistance for time step study on mesh 2 of bare hull analysis, Fn = 0.218.

7.2.3 Final Results Bare Hull Analysis

Table 7.5 gives resistance results for three froward speeds. Two of the forward speeds have previously been run for a model test by El Moctar, Shigunov, et al. (2012) (see table 6.3), and a comparison is made in figure 7.7. Additional results for convergence of forces and residuals can be found in appendix C.5. Further, the results are based on mesh 1 with a maximum CFL number of 10. The reason for using mesh 1 is that this grid is used as a basis for the numerical simulations including the wavefoil, which makes a comparison between the cases possible.

It can be seen from figure 7.7 that the numerical results differ from the model test results. The effect of sinkage and trim, and the possibility of obtaining numerical results closer to the ones of model tests have previously been discussed in section 7.2.1. Therefore, it is possible that the numerical results will come closer to those of the experimental study if the numerical simulation had been run with heave and trim data from the experiments.

Table 7.5: Resistance on bare ship hull.

U [m/s]	Fn [-]	Re $\times 10^{-6}$ [-]	R_T [N]	R_V [N]	R_P [N]
1.602	0.209	8.783	25.99	22.68	3.31
1.668	0.218	9.145	28.40	24.47	3.93
1.730	0.226	9.485	30.71	26.19	4.52

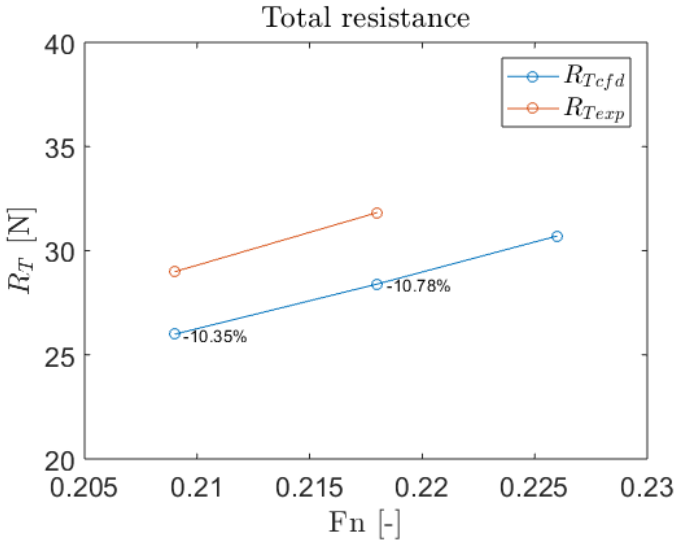

Figure 7.7: Calculated total resistance compared to experimental results.

The wave elevation on the hull surface is shown for mesh 1 and 2 in figure 7.8 at a Froude number of 0.218, with the result for mesh 3 omitted because it coincides with the result for mesh 2. The result show that the wave elevation on the hull is continuously underestimated for mesh 1 with respect to mesh 2. The reason for this is believed to be due to the resolution of the mesh on the free surface, which is higher for mesh 2 and 3.

Figure 7.8 shows the wave elevation on the hull surface, and Kinaci and Gokce (2015) made an analogous plot in their numerical research of the same hull form. The wave

elevation in figure 7.8 show some agreement with the result of Kinaci and Gokce (2015). One of the main differences are that Kinaci and Gokce (2015) found a larger through around x=5.5 metres, whereas the same through in figure 7.8 is much less pronounced. The difference can be explained by the fact that Kinaci and Gokce (2015) have used an unstructured mesh around the hull. Hence, also the free surface region around the hull is resolved by an unstructured grid. This may not be the best way of resolving the free surface as an orthogonal grid should be used to resolve the free surface (ITTC, 2014a). In the presented study, an orthogonal grid is always used to resolve the free surface. Thus, the wave elevation on the hull is believed to be of sufficient accuracy.

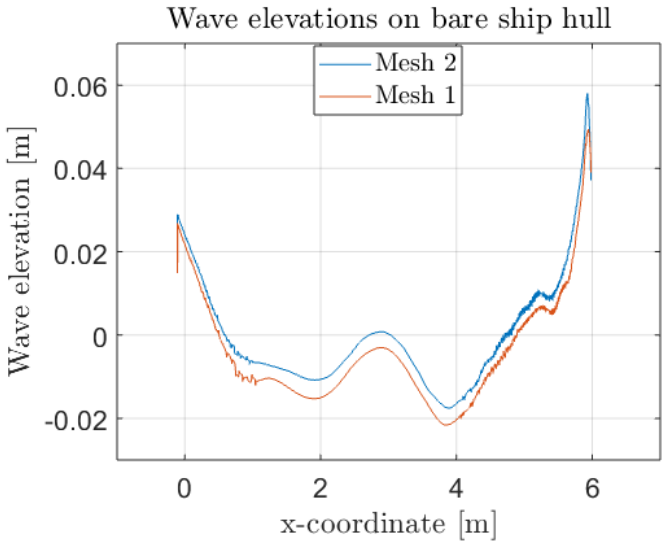

Figure 7.8: Wave elevations on the bare ship hull for Fn = 0.218.

Figure 7.9 shows the wave pattern created by the bare ship hull for mesh 1 and 2. More details of the wave pattern are captured for for mesh 2, due to the higher resolution of the grid in the free surface region. Also, the waves are dampened out earlier for mesh 1, due to the larger cell sizes and stretching of the mesh in the free surface region. Further, in the region closest to the hull, the wave pattern for mesh 1 and 2 are similar. Therefore, it can be said that mesh 1 resolves the wave pattern around the hull in a satisfactory manner relative to mesh 2.

When the ship hull has forward speed, it interacts with the fluid and modifies the flow. This is shown in figure 7.10, which shows the angle of the flow relative to the undisturbed flow at a longitudinal position 5.45 metres forward of the stern. This is where the leading edge of the wavefoil will be located, and it can be seen that the flow will enter with a varying angle of attack over the span on the wavefoil. Further, the angle of attack can be considered to be negative, which causes the low pressure region on the foil to be on the bottom side. This may lead to a wave crest being formed over the hydrofoil, which can cause an amplification of the bow wave and a larger resistance. Additionally, this implies that the wavefoil will provide a thrust force. This is in accordance with the conclusions of Bøckmann and Steen (2016), who believed that the wavefoils were able to produce a thrust force in calm water conditions due to the hull modifying the flow.

The wave crest being formed over a two-dimensional hydrofoil with negative angle of attack was investigated by the author in a preliminary study to the master thesis in

the autumn semester of 2017. The free surface elevation for this case is shown in figure 7.11, and a clear wave crest can be seen at the position x/c=0, which corresponds to the rotational centre of the hydrofoil. This may show the importance of proper positioning of a wavefoil, such that the bow wave is not amplified by the wavefoil's influence on the free surface - causing an increase in calm water resistance.

Even though the resistance results for the bare hull could have been closer to experimental results, they are considered to be stable and physical due to the mesh and time independence study results. Moreover, the grid resolution is higher than for compared studies, and is not believed to be the cause of poorer results relative to what is achieved in comparable studies. Results for the flow angle at the position of the leading edge of the wavefoil suggests that there will be a negative angle of attack, which must be considered when deciding the positioning and orientation of the wavefoil.

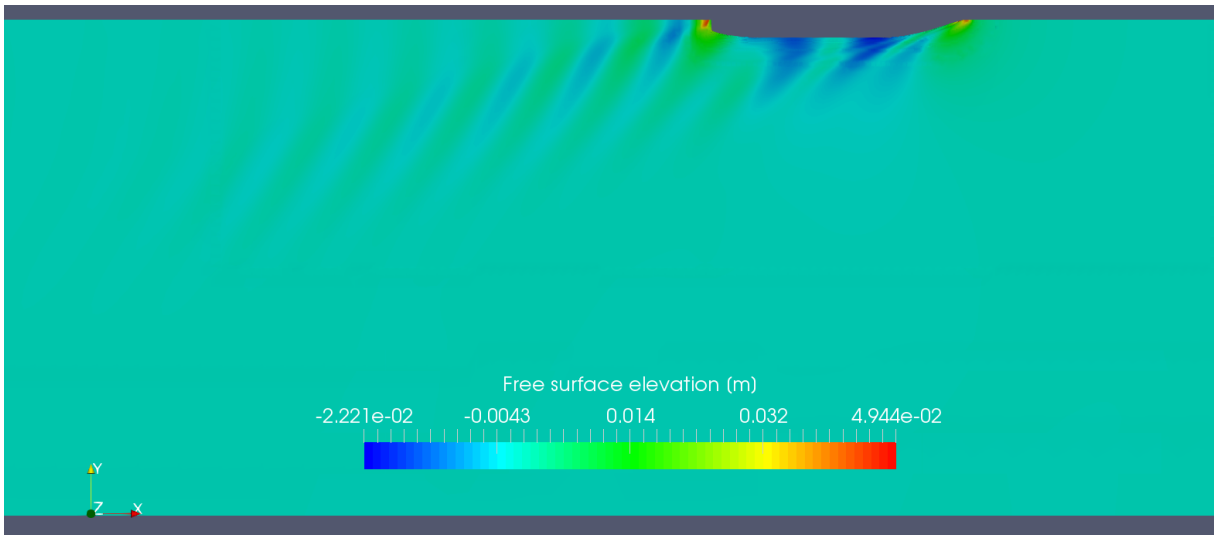

(a) Wave pattern mesh 1.

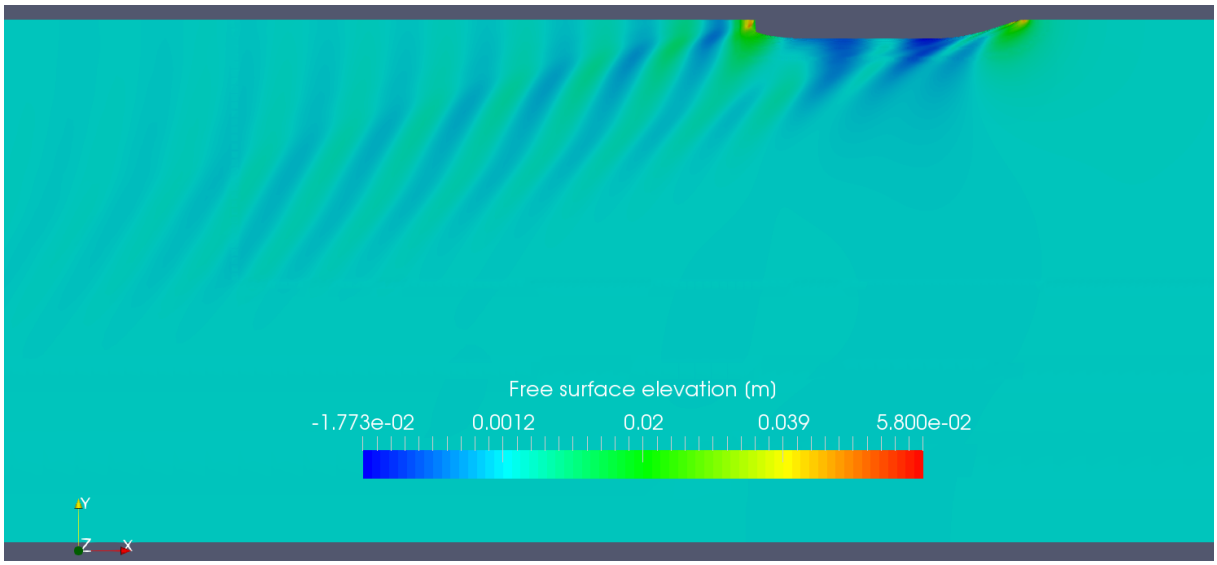

(b) Wave pattern mesh 2.

Figure 7.9: Wave pattern generated by ship hull at Fn = 0.218.

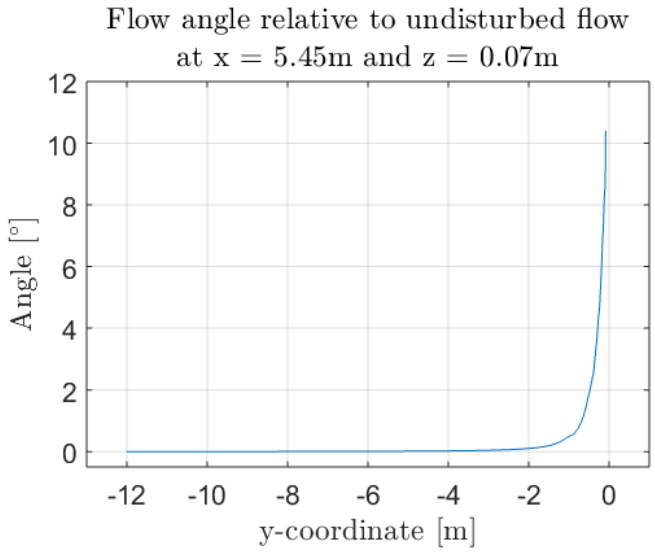

Figure 7.10: Angle of flow relative to undisturbed flow at longitudinal and vertical position where wavefoil will be placed, Fn = 0.218.

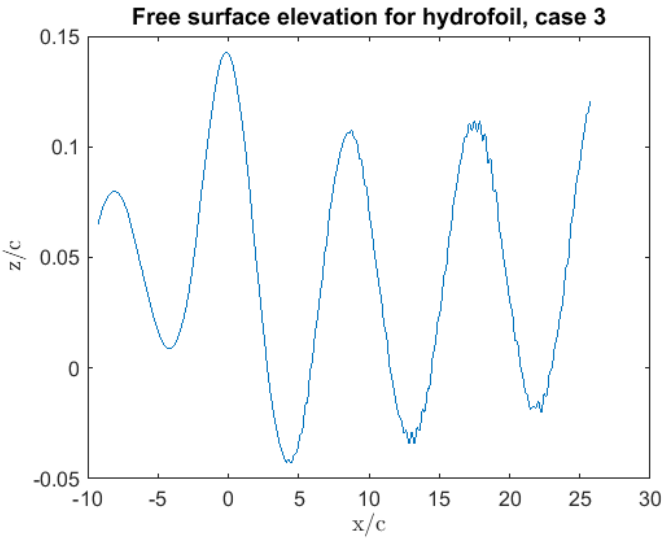

Figure 7.11: 2D free surface elevation caused by NACA 0015 hydrofoil with α = -5°, $h/c = 2$ and $Fn_h = 0.83$.

7.3 Ship Hull With Wavefoil Analysis

7.3.1 Mesh

The mesh used in the analysis of the hull including a wavefoil is based on mesh 1, where mesh parameters are given in table 7.2. The refinement level around the wavefoil is set to 12, producing approximately 477 cells over one chord length and resulting in a total number of 11 223 644 cells.

There have been some challenges with the mesh where the wavefoil intersects the hull. This can be seen in figure 7.12a at the top left corner of the intersection. Cells can here be observed to be skewed and warped, which may affect the results due to instabilities caused by nonphysical behaviour. This also caused challenges with adding layers over the wavefoil surface, and simulations crashed because of instabilities when layers were added. Several attempts on adding layers were unsuccessful, and therefore layers are only added around the ship hull. The lack of layers around the wavefoil may cause problems with resolving the forces acting on it, as the non-dimensional distance to the wall for the wavefoil should be less than a value of five according to the Spalding formula (section 4.3.1).

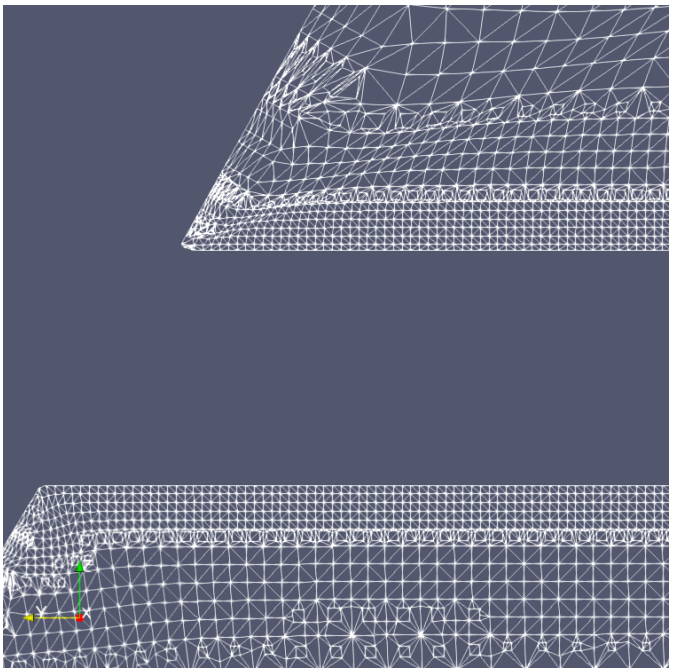

(a) Mesh at intersection of hull and wavefoil.

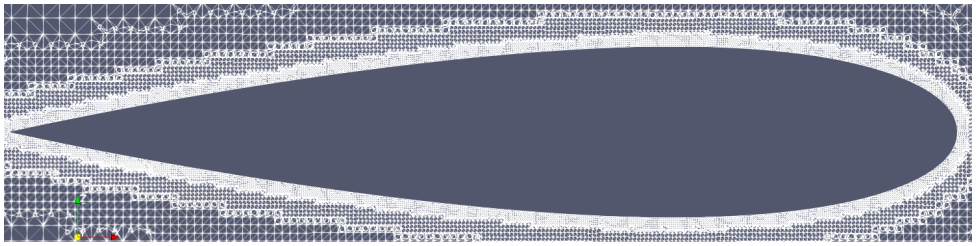

(b) Mesh at cross-section of wavefoil.

Figure 7.12: Mesh at intersection and cross-section of wavefoil.

The mesh around the cross-section of the wavefoil can be seen in figure 7.12b. It shows that no layers are added, but the snapping phase in snappyHexMesh has resulted in a smooth mesh around the hydrofoil. Also, it can be seen form the figure that the sharp trailing edge of the foil profile is well resolved by the mesh.

Attempts on making a finer mesh around the hydrofoil was made by using mesh 2 as a basis, and 12 refinement levels around the wavefoil. The same problems with adding layers occurred, causing the numerical simulations to crash. Therefore, no layers were added to the wavefoil, which resulted in a running simulation. However, the mesh based on mesh 2 had nearly 20 million cells, which required a long computational time. It would take 10 days to simulate 20 seconds. Due to time limitations, analyses based on mesh 2 were dismissed as it would have taken too much time to produce a representative data series. Therefore, it was decided to use mesh 1 as a basis, for which results are comparable to the results for mesh 1 on the bare ship hull.

7.3.2 Results

Numerical simulations are run for three forward speeds, which corresponds to those in the analysis of the bare ship hull. The maximum CFL number used is 10, which is used based on the time step analysis of the bare hull in section 7.2.2. Convergence of the forces on the hull and the wavefoil for Fn=0.218 can be seen in figure 7.13, and appendix D gives force convergence and residuals for all three forward speeds.

It can be seen from figure 7.13 that the force oscillations are not smooth as they are for the bare hull analysis. This is believed to be connected to the mesh, where cells in the intersection of the hull and the wavefoil are of poor quality. This results in instabilities, which OpenFOAM corrects for by adjusting the time step such that the maximum CFL number is kept below a value of 10. The instabilities, which can be seen in figure 7.13, occurs when the maximum CFL number rises above 10, but is quickly corrected for in the next time step.

Even though there are some instabilities in the numerical results, no consistent large drop or increase in forces occur. Thus, it is possible to use the average over the oscillations, which is done for about the last 35-40 seconds of the result. The reason for not simulating for a longer period of time is due to the fact that it took 10 days to simulate the presented results for each case. Due to time limitations, the results are therefore not simulated for a longer time period. However, it can be seen that the forces oscillate about the mean line in figure 7.13, and the results are considered to be representative for the case.

The non-dimensional distance to the wall for the hull and the wavefoil can be inspected in figure 7.14. The result show that the use of wall functions for the logarithmic region is correct for the hull. However, for the wavefoil the y^+-values are too high for correctly using wall functions based on the Spalding formula. The values should have been less than five, but ranges instead around a value of 9.5 for large parts of the wavefoil. Hence, the forces acting on the wavefoil may not be of correct magnitude, but is thought to give a reasonable indication due to the y^+-values being close to the value of five.

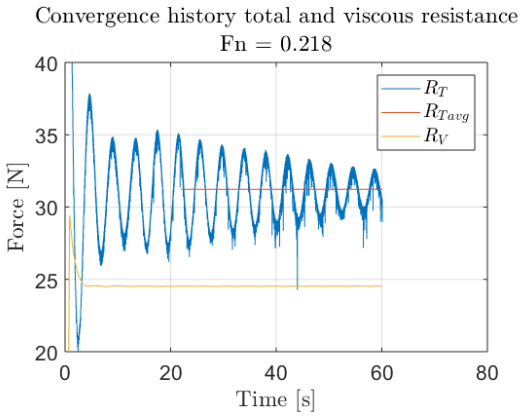

(a) Total and viscous resistance on hull.

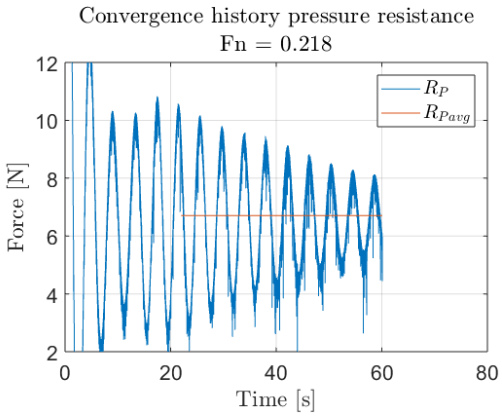

(b) Pressure resistance on hull.

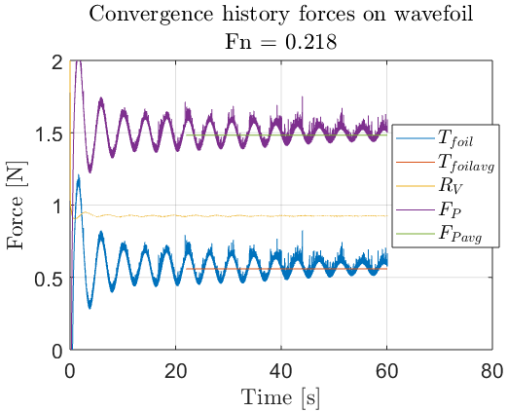

(c) Forces on wavefoil.

Figure 7.13: Convergence of forces on hull and wavefoil for Fn = 0.218.

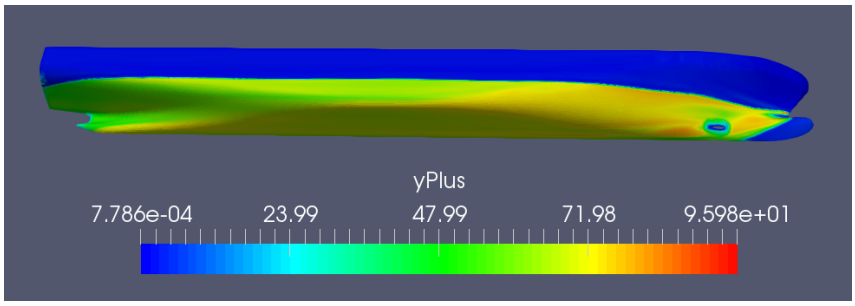

(a) Ship hull.

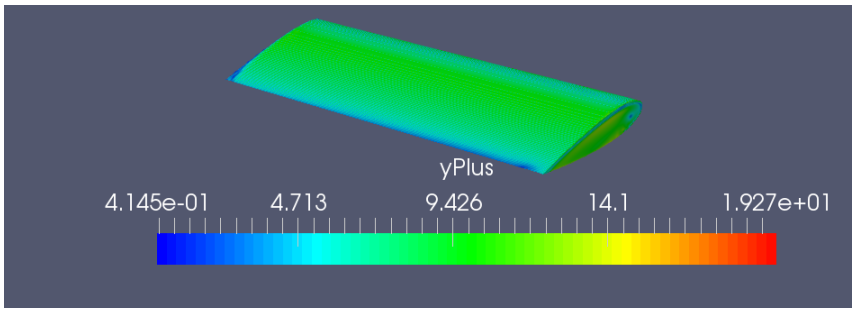

(b) Wavefoil.

Figure 7.14: Non-dimensional distance to the wall y^+, ship with wavefoil analysis for Fn = 0.218.

Table 7.6 presents the resistance forces acting on the ship hull for three forward speeds. The wavefoil is included in the calculation, but the forces in table 7.6 are only calculated for the ship hull. The forces acting independently on the wavefoil are given in table 7.7 together with the Froude submergence number, where a negative sign indicates a forward force. It can be seen from table 7.7 that the wavefoil produce a foil thrust T_{foil}, which is due to the pressure force F_P. Lastly, the foil thrust is found by adding the viscous resistance to the pressure force.

The resistance components acting on the ship hull including the wavefoil forces are presented in table 7.8. Here, the total resistance is found by adding the foil thrust to the resistance force calculated independently for the ship hull. From the results one can see that the wavefoil produces a thrust force for all Froude numbers, and that the foil thrust increase with increasing forward speed. Resistance results for the bare ship hull are given in table 7.5.

Table 7.6: Resistance on ship hull not including forces on wavefoil.

U [m/s]	Fn [-]	Re $\times 10^{-6}$ [-]	R_T [N]	R_V [N]	R_P [N]
1.602	0.209	8.783	28.46	22.76	5.70
1.668	0.218	9.145	31.23	24.53	6.70
1.730	0.226	9.485	34.03	26.22	7.81

Table 7.7: Forces on wavefoil.

U [m/s]	Fn_h [-]	T_{foil} [N]	R_V [N]	F_P [N]
1.602	1.23	-0.28	0.86	-1.14
1.668	1.28	-0.56	0.92	-1.48
1.730	1.32	-0.82	0.98	-1.80

Table 7.8: Resistance on ship hull including wavefoil.

U [m/s]	Fn [-]	R_T [N]	R_V [N]	R_P [N]
1.602	0.209	28.18	23.62	4.56
1.668	0.218	30.67	25.45	5.22
1.730	0.226	33.21	27.20	6.01

A comparison between the total resistance of the hull with wavefoil and the bare hull is made in figure 7.15, including the thrust force from the wavefoil. It can be seen that the resistance increases in calm water when the wavefoil is used compared to the bare hull resistance, even though if the wavefoil produces a thrust force. This corresponds to the experimental results of Bøckmann and Steen (2016, figure 12). It is believed that the increase in resistance is due to an increase in wave-making resistance due to the wavefoil. The additional wave-making resistance can then be $R_{Wadd} = R_{Twavefoil}$ - R_{Tbare}, which results in:

- $Fn = 0.209$: $R_{Wadd} = 2.19$N, Relative difference = 8.43%
- $Fn = 0.218$: $R_{Wadd} = 2.27$N, Relative difference = 8.00%

- $Fn = 0.226$: $R_{Wadd} = 2.50$N, Relative difference = 8.14%

The relative difference between the ship hull with wavefoil and the bare ship hull total resistance is 8% or higher for all three Froude numbers, and is considered to be of significant magnitude. Further, that there is an increase in wave-making resistance as the cause is supported by the plotted wave elevations on the ship hull in figure 7.16. A clear rise in wave elevation can be seen around x= 5-5.5 metres, which corresponds to the longitudinal position of the wavefoil. Some cancellation can also be seen in an area forward of x=4 metres, but it is though that the amplification gives a higher contribution. This is supported by the small amplifications which can be seen downstream of x=4 metres.

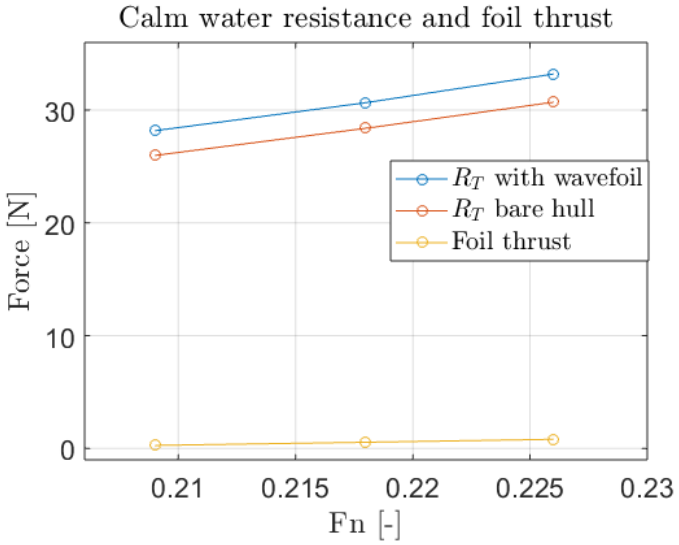

Figure 7.15: Calm water resistance and foil thrust.

Figure 7.17, 7.18 and 7.19 gives a comparison between the wave patterns created at three different Froude numbers. One can see that there is an amplification in the bow region when the wavefoil is included. Further, the wave throughs that appear along the ship hull, including the wavefoil, seem to be somewhat less prominent relative to the bare hull. This is believed to be caused by the free surface waves generated by the wavefoil, which amplifies the waves created by the ship hull. Another aspect that may be considered from figures 7.17, 7.18 and 7.19 is the effect of the wavefoil further out from the hull surface, which cannot be done with the results in figure 7.16. It can be deducted that the wavefoil has modified the wave pattern by amplifying the wave-making away from the hull also. Thus, it may be said that the ship hull with wavefoil gives away more energy to wave-making than what is the case of the bare hull, resulting in an increase of the wave pattern resistance in calm water.

That the wavefoil creates free surface waves in the numerical analyses is supported by linear theory, where a hydrofoil will create free surface waves when Fn_h is larger than 0.4 (see section 3.3). Table 7.7 show that Fn_h is considerably larger for all three forward speeds. Further, the magnitude of the wave-making by the wavefoil must be large enough in order to influence the steady wave pattern of the ship hull in calm water. In the current analysis the magnitude of the wavefoil's wave-making is of a magnitude that influence the steady wave pattern of the ship hull, which is supported by the findings in figure 7.16, 7.17, 7.18 and 7.19. Furthermore, the negative angle of attack over the span of the wavefoil

found in figure 7.10 causes a crest to form over it, instead of a through that may be needed in order to cancel out parts of the bow wave.

It is possible that numerical simulations should have been run for a wider range of Froude numbers. Froude numbers below 0.2, where the wave resistance becomes less important, may have given further indications on the importance of the wave-making due to the wavefoil. Further, a wider range of forward speeds could have given indications on the importance of the phasing between the wave-making due to the ship hull and the wavefoil, as wavelength increases with increasing forward speed. However, because of the time requirements of the numerical simulations, there was not sufficient time for further analyses. Additionally, the Froude numbers simulated are for, and close to, design speed of the vessel, which is where the ship is most likely to operate and therefore considered to be of highest importance in the study.

Hence, it is found that the wavefoil in the current research affects the steady wave pattern of the ship hull and causes an increase in wave resistance. This must be considered when designing a wavefoil so that it causes the least negative, or causes positive, effects on the steady wave pattern and wave-making resistance.

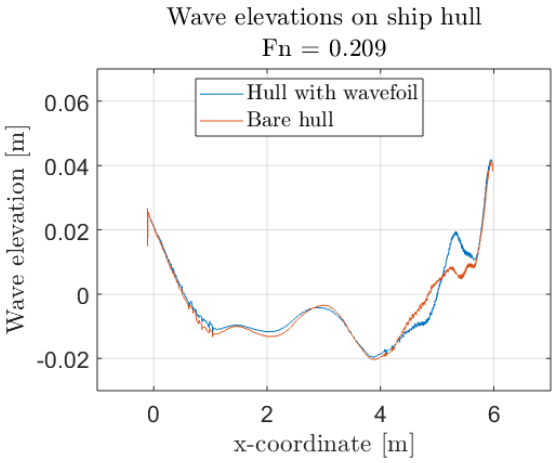

(a) Fn = 0.209.

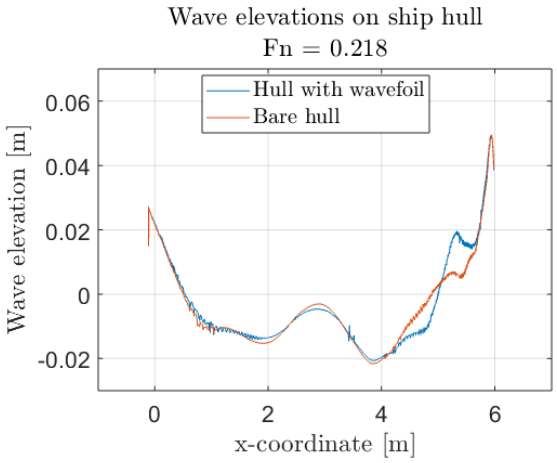

(b) Fn = 0.218.

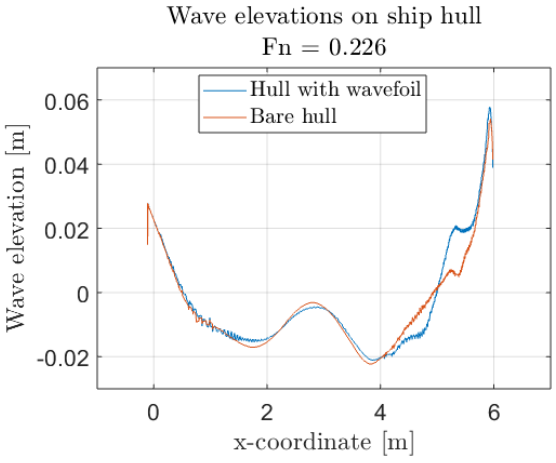

(c) Fn = 0.226.

Figure 7.16: Wave elevations on ship hull with and without wavefoil.

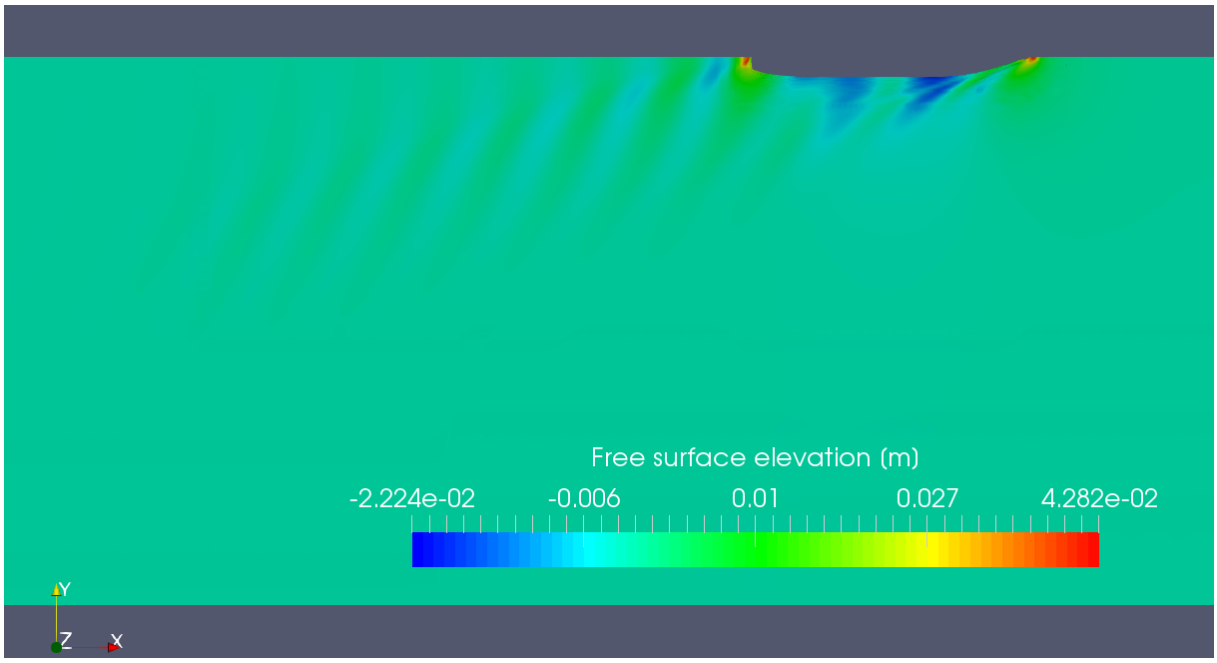

(a) Wave pattern bare ship hull.

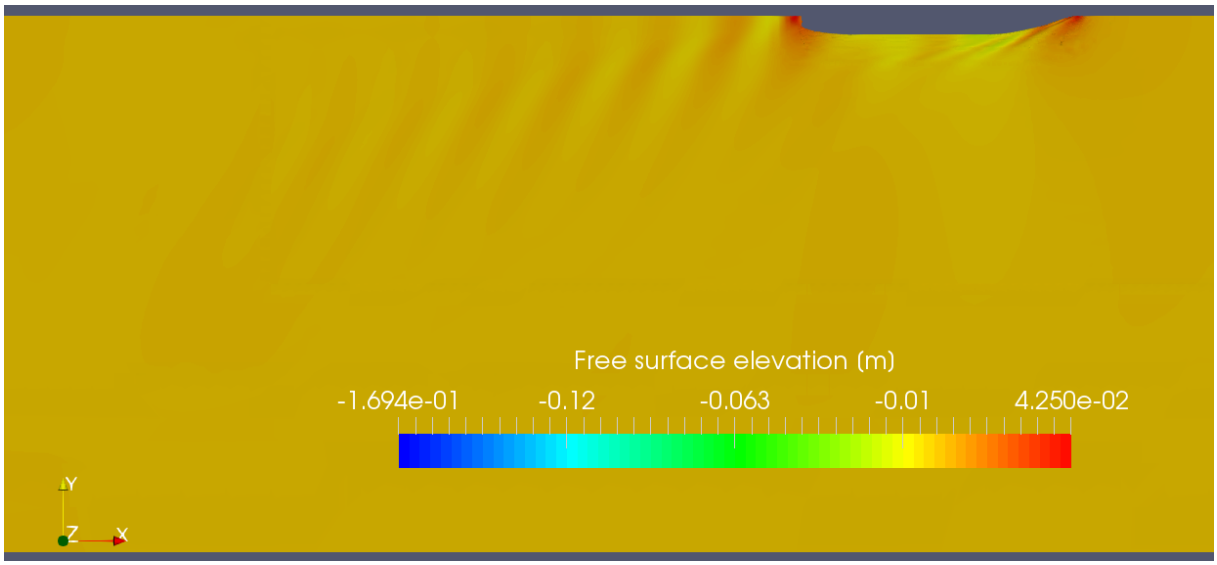

(b) Wave pattern ship hull with wavefoil

Figure 7.17: Wave patterns at Fn = 0.209.

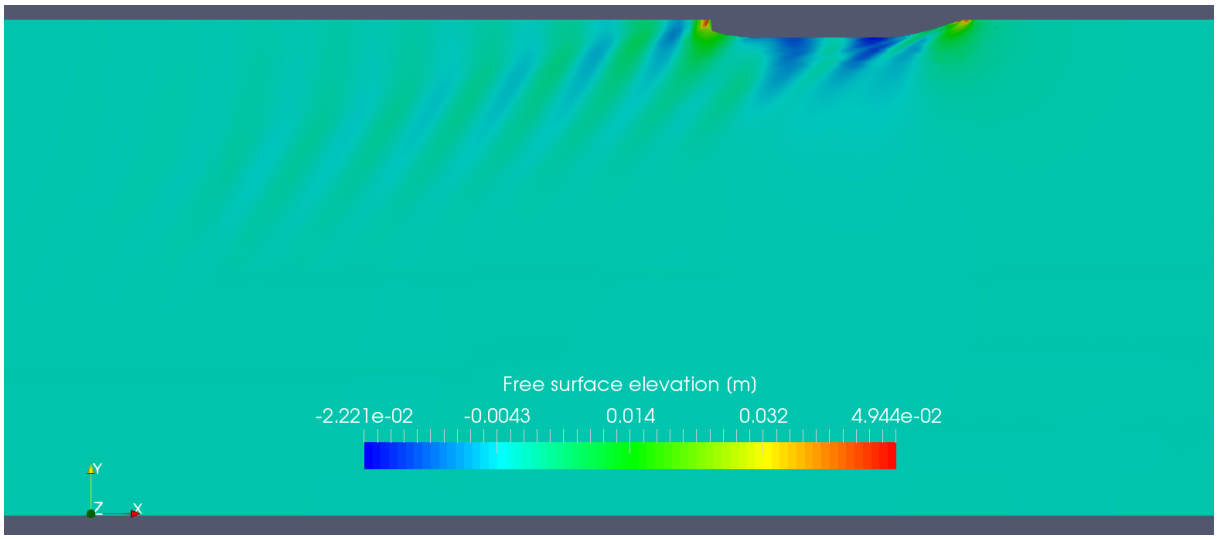

(a) Wave pattern bare ship hull.

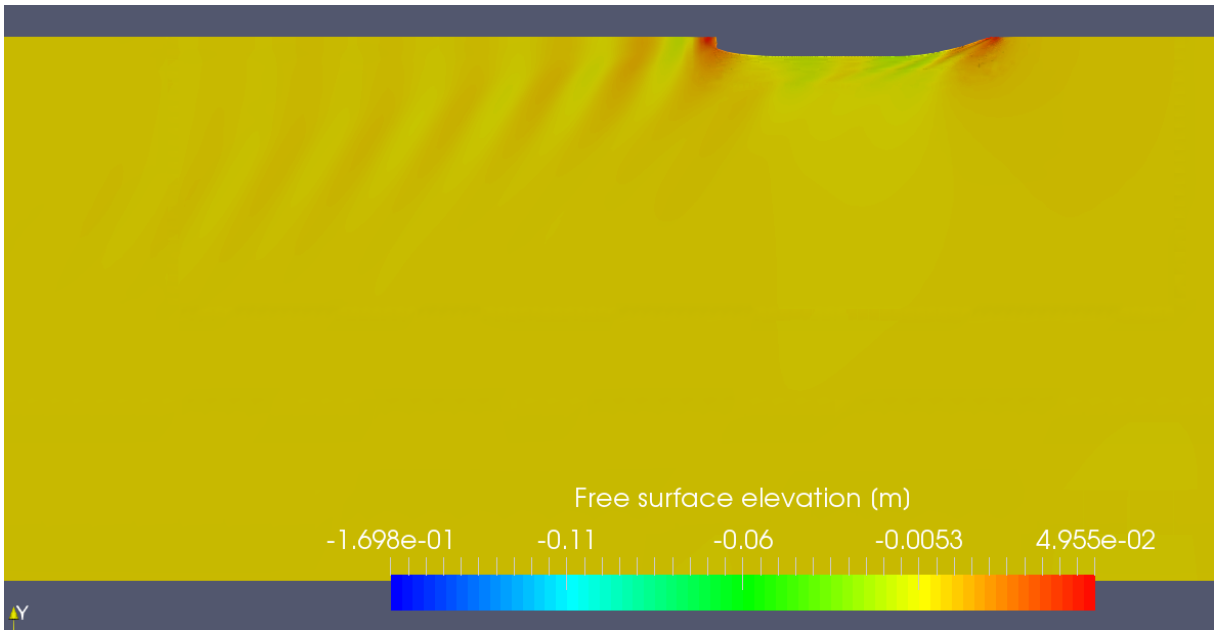

(b) Wave pattern ship hull with wavefoil.

Figure 7.18: Wave patterns at Fn = 0.218.

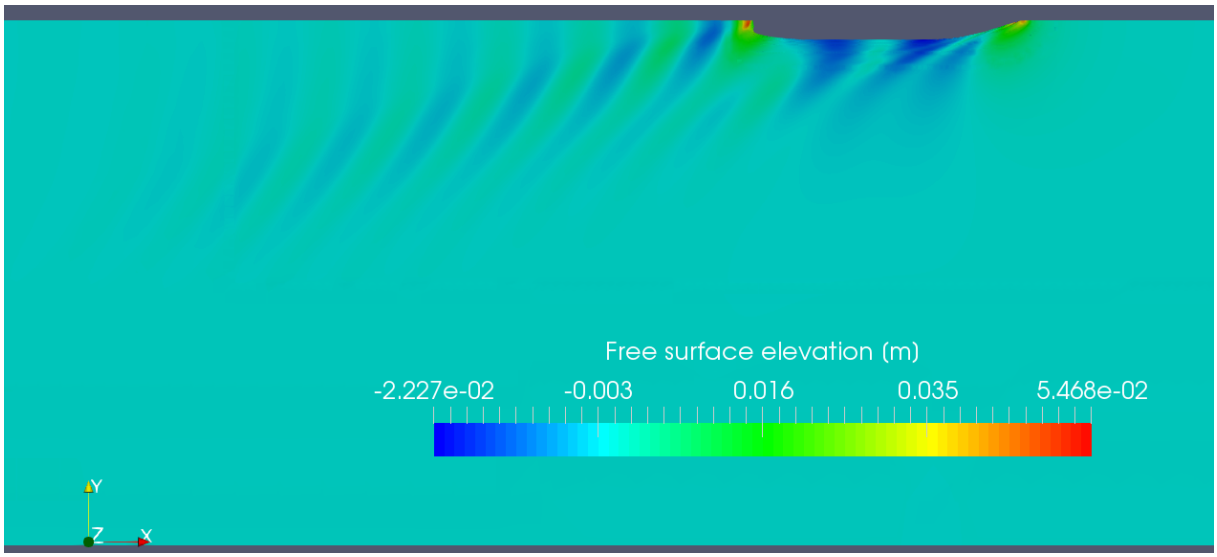

(a) Wave pattern bare ship hull.

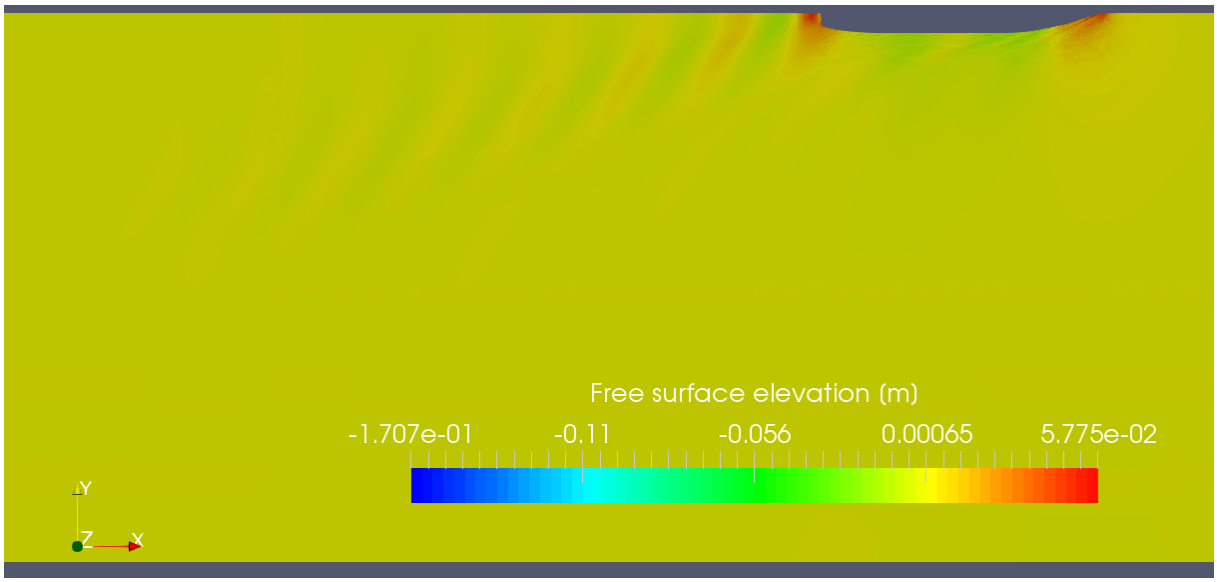

(b) Wave pattern ship hull with wavefoil.

Figure 7.19: Wave patterns at Fn = 0.226.

7.4 Discussion on Using Wavefoils

There is no doubt that wavefoils can give positive effects for ships in waves by creating a significant thrust force - and by so reducing greenhouse gas emissions (see chapter 1). However, in calm water conditions there have been reported negative effects relating to the resistance by Bøckmann and Steen (2016) and Naito and Isshiki (2005). The assumption of Bøckmann and Steen (2016) saying that the wavefoils modify the wave-making resistance is supported by the results in this study, which show that the wave pattern changes unfavourably with respect to the total resistance when including a wavefoil.

Only one case with respect to the wavefoil's position have been studied for three different Froude numbers in the current research. The negative effects found must be accounted for when considering wavefoils in a design phase. Some practical implications on improvements and design are therefore made in the following text.

The result in figure 7.20 is obtained by calculating the flow angle at the leading edge's position from the bare hull analyses. It shows that there will be a varying angle of attack over the span of the wavefoil for the three forward speeds tested. Further, this shows that the flow will be directed downwards over the span of wavefoil due to the influence of the ship hull, which will give a downwards directed lift force. Therefore, the wavefoil will produce a wave crest on the free surface above it and amplify the bow wave. To counteract this, one could rotate the wavefoil, giving a positive angle of attack relative to the undisturbed flow. This may result in a positive angle of attack also from the flow caused by the ship hull. Further, figure 7.20 indicates that the inflow angle will vary between approximately 2.5 and 10.5 degrees, and large parts of the wavefoil will experience inflow angles higher than 5 degrees. Therefore it may be said that the wavefoil should be rotated with a minimum angle of 5 degrees to obtain better results with respect to changing the negative foil lift to positive. It is possible that such a rotation of the wavefoil will result in a wave through being formed above it on the free surface, and by so cancel parts of the bow wave and reduce the wave-making resistance. This is in accordance with the study of Abkowitz and Pauling Jr. (1953), who achieved a reduction in wave-making resistance, and also total resistance, by using a hydrofoil with positive angle of attack that had a cancellation effect on the bow wave.

An even rotation of the wavefoil may not give the best results with respect to resistance due to varying inflow angle. To improve this a twisted foil can be used, which can be twisted relative to the inflow angle. The result in figure 7.20 can give indications on how much the wavefoil should be twisted. A twisted foil can for instance be made to produce no lift force in calm water. It will then give an additional drag force to the ship-wavefoil system. On the other hand, a positive aspect may be that the thickness effect of the wavefoil will cause a wave through above it, thereby cancelling parts of the bow wave and reducing the wave-making resistance.

Another possibility is to use an actively pitch controlled wavefoil. This is possible for both an untwisted and a twisted foil. The active pitching can be used for rotating the wavefoil to an orientation that results in a positive angle of attack at different speeds. Hence, the wavefoil may cause a wave through on the free surface as described above, and active pitching be used for optimisation at different speeds. In addition, active pitch control can be used to produce the highest possible foil thrust in waves for a given system.

It is also important to consider the positioning of the wavefoil. The submergence of the wavefoil will contribute to the magnitude of free surface waves created, and thus the amount of amplification or cancellation of the bow wave. Further, the longitudinal position of the wavefoil is an important aspect. As can be seen from figure 7.16, the wavefoil is located at a position, and with such an orientation, that it amplifies the bow wave. This causes a rise in wave-making resistance and total resistance, despite of the foil thrust created. Therefore, in addition to considering the orientation of the wavefoil, one must find a longitudinal position that cancel out the bow wave by ensuring that the bow wave and wavefoil created waves are out of phase. One way of obtaining a reasonable longitudinal position of the wavefoil can be to study the steady wave patterns of the ship hull and wavefoil separately. The wave patterns can then be superimposed to find a location in which the superimposed wave system is believed to give the least wave pattern resistance.

By studying the interference flow field, as is also suggested by Naito and Isshiki (2005), the most favourable positioning and orientation of the wavefoil can be found. It is possible that there is no general location of the wavefoil that may affect the resistance favourably - in terms of producing thrust and reducing the wave-making resistance in calm water. For design purposes it can be recommended that the interference flow field is found individually for each case. One can then find a position and orientation that affects the total resistance in a positive or least negative way in calm water, and at the same time producing significant foil thrust in waves. Hence, the design of wavefoils must include an optimisation process. If fixed foils are to be used, they must be designed for conditions in which the ship is most likely to operate.

Assuming linear theory, one can superimpose the forces in calm water and forces due to incoming waves. This means that the interaction effect causing increased wave pattern resistance is also present in waves. Previous studies (see chapter 1) have shown that the foil thrust is significant in waves and reduces the total resistance. One can then say that the positives outweighs the negatives in waves. However, the interaction effect should be solved with respect to the increased wave pattern resistance in order to obtain optimum effect from the wavefoil.

The optimisation process for designing wavefoils that works well in calm water and waves, with respect to wave-making and total resistance, may be costly in terms of both time and money. A retractable foil system may therefore be recommended. Wavefoils can then be stored in calm water conditions to avoid negative effects on the wave pattern resistance, and be deployed in conditions where the foil thrust is significant and outweighs the increased wave pattern resistance. The Wavefoil company (Wavefoil, 2018) is currently developing such a system, where the wavefoils are allowed to be stored within the ship hull in conditions where they have little effect. Another positive aspect of a retractable foil system is seen to be that the wavefoils can be stored during docking, as it may be difficult for a ship to lay close to a port with wavefoils possibly increasing the total breadth.

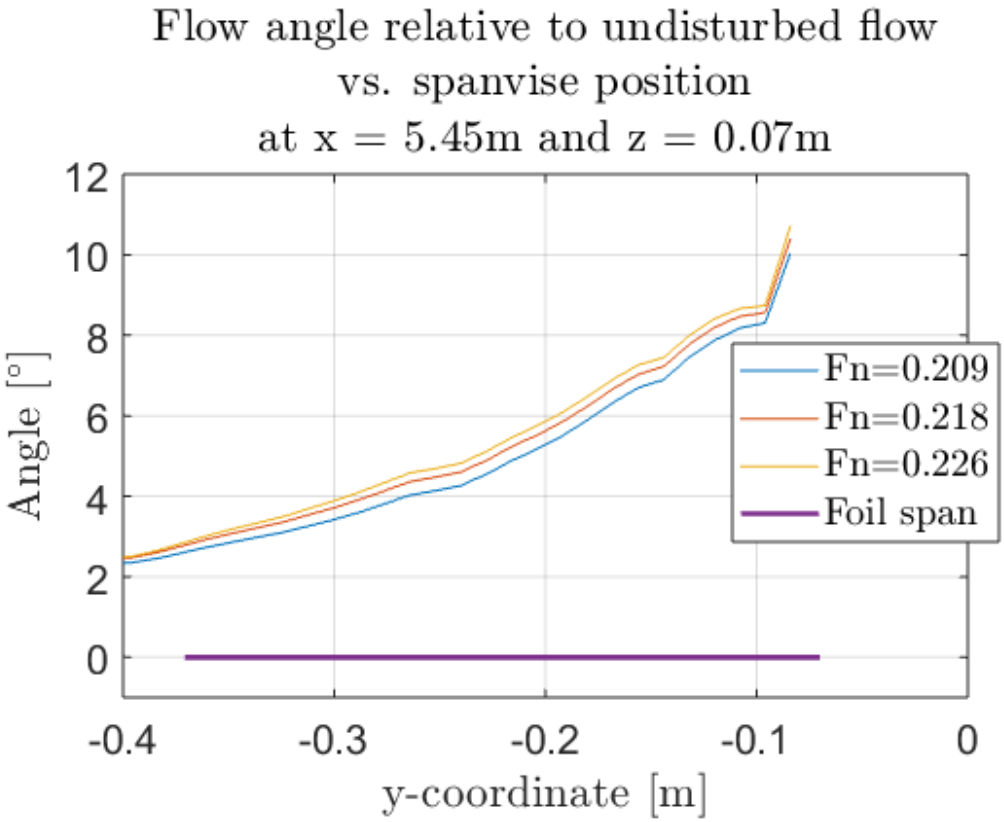

Figure 7.20: Flow angle relative to undisturbed flow over the span of the wavefoil at longitudinal and vertical position of the leading edge.

Chapter 8

Conclusions and Further Work

8.1 Conclusions

The goal to counteract global climate change can be said to be a driving force in finding and developing ways to utilise clean energy for propulsion of ships. One way is to use bow mounted hydrofoils - wavefoils - that convert wave energy into a propulsive thrust. In addition, this will result in other positive aspects such as reduced fuel costs and motions in waves.

In the present study the RANS equation have been numerically solved using OpenFOAM in order to find the effects of a wavefoil on the wave pattern resistance of a ship in calm water. The study has focused on a particular case using the DTC hull in model scale, but a general understanding of the interaction between the ship hull and wavefoil have been sought through analysis and discussion of the results.

For learning the ways of the meshing utility snappyHexMesh and validating the frictional resistance, a double body analysis of the bare hull was conducted. The results show little variation with grid density and resolution of the boundary layer. In addition, the calculated friction coefficient is somewhat underestimated when compared to the ITTC-1957 correlation line, but is found acceptable when compared to existing literature.

Results for the bare ship hull show that the resistance is underestimated with respect to model test results, with over 10% relative difference for two comparable forward velocities. The underestimation is not believed to be due to the mesh, as a greater density is used in the current research as opposed to comparable studies. Further, the non-dimensional distance to the wall is found to be in the logarithmic region, making the use of logarithmic wall functions correct for the case. Ways to make the numerical result come closer to the experimental are discussed, with the possibility of running the simulation with heave and trim data from the experiments to create more accurate results. Lastly, the results are considered to be stable, shown by systematic mesh and time independence studies, and physical.

Creating a working computational grid for the ship hull with a wavefoil proved to be difficult due to skewed and warped cells where the wavefoil intersects the hull. However, a working grid was obtained by omitting layer addition over the surface of the wavefoil. This caused y^+-values for large parts of the wavefoil to be around 9.5. Hence, the forces

acting on the wavefoil may not have been correctly resolved, yet they still are considered to give reasonable indications. Attempts on making finer grids were made. This resulted in a large amount of cells and required time for the analysis was too large compared to available time for the study. A mesh that may have yielded more accurate results and lower y^+-values on the wavefoil was therefore not found due to time limitations.

Instabilities caused by bad cells at the hull-wavefoil intersection was evident when plotting forces versus simulated time. However, no continuous large drop or increase in the forces occurred, and the forces was found to converge towards the mean value. Thus, the forces are considered to be physical.

Even though it is found that the wavefoil produces a thrust force in the current research, the total resistance increases when the wavefoil is attached. For Froude numbers 0.209, 0.218 and 0.226 the total resistance respectively increased by 8.43%, 8.00% and 8.14%. Plots of the wave elevations on the ship hull surface indicates that the wavefoil amplifies the bow wave, and by so increases the wave-making resistance of the ship. Further, the steady wave pattern in calm water is altered in an unfavourable way when the wavefoil is included. Hence, the wavefoil has contributed in a negative manner with respect to resistance by increasing the wave pattern resistance of the ship.

One of the main reasons for the wavefoil's negative modification of the wave-making is believed to be a negative angle of attack from the inflow caused by the ship hull. This creates a wave crest being formed on the free surface over the wavefoil that amplifies the bow wave, which must be considered in design and positioning of the wavefoil.

Due to the negative effects of the wavefoil in calm water found in this study, practical implications for improvement and design have been discussed. It is recommended that an orientation of the wavefoil that produce a wave through over it on the free surface is found. This can for instance be achieved through a uniform rotation of the wavefoil, which should result in a positive angle of attack from the inflow. Further, twisting of the foil may give positive results in terms of the wave-making. Also, the longitudinal position of the foil should be carefully considered in order to find a location where the bow wave is least amplified, or where a cancelling effect occur. It is important that these suggested improvements do not affect the ability of the wavefoil to produce a thrust force in waves, and an optimisation process is advised. Lastly, a retractable foil system may be useful to avoid the negative effects due to the wavefoil in calm water conditions. However, the negative effects will also be present in waves even if the total resistance is reduced by the foil thrust. Therefore, the problem should be solved in order to achieve optimum effect from the wavefoil.

The study has some shortcomings with respect to accuracy of the results, which may be due to neglecting sinkage and trim, too high y^+-values for the wavefoil and/or bad cells at the hull-wavefoil intersection. The choice of using the DTC hull in the present study was made due to it being easily available in OpenFOAM, and that there exist several experimental and numerical studies on the bare hull. In hindsight the work should have been performed using the same hull and wavefoil as in the experimental research of Bøckmann and Steen (2016). This would have enabled more validation of the results - especially for the forces on the wavefoil that has no comparable data in the present study. However, it was not realised until late in the work that a different ship hull should have been used, and there was not sufficient time to change ship model.

Due to mesh and time independence studies, and validation of the bare ship hull results, the results for the ship hull including the wavefoil are considered to be satisfactory and give accurate implications on the flow field. This is further supported by the fact that the results in principle agree with the model test results of Bøckmann and Steen (2016). Thus, the study is believed to provide an understanding of the interaction between the ship hull and wavefoil in calm water and the effects on the wave pattern resistance.

8.2 Suggestions for Further Work

There is a lot of existing work on wave propulsion of ships. However, to the authors knowledge, this is the first study that numerically solves the RANS equation to investigate the interaction effect between a ship hull and a wavefoil. This gives basis for further development and research using CFD.

First of all, the numerical model can be improved to provide numerical results closer to model test results for the bare ship hull. Further, it can be improved by increasing the grid resolution when including the wavefoil. This may result in better capturing of the flow features, and lower non-dimensional distances to the wall on the wavefoil surface - leading to more accurate prediction of the forces. Additionally, letting the ship model be free to heave and pitch may give more physical results. Lastly, a wide range of Froude numbers can be tested for finding the influence due to a wavefoil in a larger speed range.

A natural progression can be to test various longitudinal positions of the wavefoil in calm water. One can then find a position where the wave-making of the ship hull and wavefoil interacts in the most favourable way. Another way of attacking this, is to test the ship hull and wavefoil separately and inspect the individual wave patterns. A propitious longitudinal position may then be reasoned. Another interesting aspect can be to test the wavefoil with a rotation, giving it a positive angle of attack relative to the undisturbed flow. This may cause a cancellation effect instead of amplification, which is found in the present study.

The flow field caused by the hull shape may be used to design a twisted foil that do not cause any lift in calm water conditions. It would be interesting to test a twisted wavefoil attached to the ship hull, and inspect the effects on the wave pattern.

The design of a wavefoil must not restrain its main purpose; to produce a thrust force in waves. Design with respect to calm water should not result in a considerable loss of performance in waves. Therefore, a thorough CFD study of a ship equipped with wavefoils in waves would be interesting.

Bibliography

Abkowitz, M. A. and J. R. Pauling Jr. (1953). "The Ship Model Towing Tank at M.I.T - Part 2 The Use of Hydrofoils to Reduce the Wavemaking Resistance of Ships". In: *Society of Naval Architects and Marine Engineers*, pp. 80–86.

Airfoil Tools (2018). *NACA 4 digit airfoil generator: NACA 4 digit airfoil calculation*. Accessed: 22.07.2018. URL: `http://airfoiltools.com/airfoil/naca4digit`.

Belibassakis, K. A. and G. K. Politis (2012). "Hydrodynamic Analysis of Flapping Wing Systems for Augmenting Ship Propulsion in Rough Sea". In: *Proceedings of the Twenty-second International Offshore and Polar Engineering Conference*, pp. 929–936.

– (2013). "Hydrodynamic performance of flapping wings for augmenting ship propulsion in waves". In: *Ocean Engineering* 72, pp. 227–240.

Bøckmann, E. (2015). "Wave Propulsion of Ships". PhD thesis. Trondheim: Norwegian University of Science and Technology.

Bøckmann, E. and S. Steen (2016). "Model test and simulation of a ship with wavefoils". In: *Applied Ocean Research* 57, pp. 8–18.

Bøckmann, E., A. Yrke, and S. Steen (2018). "Fuel savings for a general cargo ship employing retractable bow foils". In: *Applied Ocean Research* 76, pp. 1–10.

Bouman, E. A., E. Lindstad, A. I. Rialland, and A. H. Strømman (2017). "State-of-the-art technologies, measures, and potential for reducing GHG emissions from shipping - A review". In: *Transportation Research Part D: Transport and Environment* 52, pp. 408–421.

Çengel, Y. A. and J. M. Cimbala (2014). *Fluid Mechanics: Fundamentals and Applications*. 3rd ed. Singapore: MCGraw-Hill Education.

CFD Online (2014). *Turbulence free-stream boundary conditions*. Accessed: 21.06.2018. URL: `https://www.cfd-online.com/Wiki/Turbulence_free-stream_boundary_conditions`.

De Silva, L. and H. Yamaguchi (2012). "Numerical study on active wave devouring propulsion". In: *Journal of Marine Science and Technology* 17(3), pp. 261–275.

El Moctar, O., V. Shigunov, and T. Zorn (2012). "Duisburg Test Case: Post-Panamax Container Ship for Benchmarking". In: *Ship Technology Research* 59(3), pp. 50–64.

El Moctar, O., S. Sigmund, J. Ley, and T. E. Schellin (2017). "Numerical and Experimental Analysis of Added Resistance of Ships in Waves". In: *Journal of Offshore Mechanics and Arctic Engineering-Transactions Of The As* 139(1).

Faltinsen, O. M. (1990). *Sea Loads on Ships and Offshore Structures*. Camebridge: Camebridge University Press.

– (2005). *Hydrodynamics of High-Speed Marine Vehicles*. Cambridge: Cambridge University Press.

Grue, J., A. Mo, and E. Palm (1988). "Propulsion of a foil moving in water waves". In: *Journal of Fluid Mechanics* 186, pp. 393–417.

Holzmann, Tobias (2018). *Mathematics, Numerics, Derivations and OpenFOAM(R)*. Accessed: 11.07.2018. URL: `http://voluntary.holzmann-cfd.de/publications/mathematics-numerics-derivations-and-openfoam`.

Issa, R. I. (1985). "Solution of the Implicitly Discretised Fluid Flow Equations by Operator-Splitting". In: *Journal of Computational Physics* 62(1), pp. 40–65.

Isshiki, H. (1982a). "A Theory of Wave Devouring Propulsion (1st Report) - Thrust Generation by a Linear Wells Turbine". In: *Journal of the Society of Naval Architects of Japan* 151, pp. 54–64.

– (1982b). "A Theory of Wave Devouring Propulsion (2nd Report) - Optimized Foil Motions for a Passive-Type Wave Devouring Propulsor". In: *Journal of the Society of Naval Architects of Japan* 152, pp. 89–100.

Isshiki, H. and M. Murakami (1983). "A Theory of Wave Devouring Propulsion (3rd Report) - An Experimental Verification of Thrust Generation by a Passive-Type Hydrofoil Propulsor". In: *Journal of the Society of Naval Architects of Japan* 154, pp. 118–128.

– (1984). "A Theory of Wave Devouring Propulsion (4th Report) - A Comparison Between Theory and Experiment in Case of a Passive-Type Hydrofoil Propulsor". In: *Journal of the Society of Naval Architects of Japan* 156, pp. 102–114.

ITTC (2011a). *ITTC - Recommended Procedures and Guidelines: Practical Guidelines for Ship CFD Applications*. Section 7.5-03-02-03 Revision 01.

– (2011b). *ITTC - Recommended Procedures and Guidelines: Resistance Test*. Section 7.5-02-02-01 Revision 03.

– (2014a). *ITTC - Recommended Procedures and Guidelines: Practical Guidelines for Ship CFD Applications*. Section 7.5-03-02-03 Revision 01.

– (2014b). *ITTC - Recommended Procedures and Guidelines: Practical Guidelines for Ship Resistance CFD*. Section 7.5-03-02-04 Revision 00.

Karim, Md. M., B. Prasad, and N. Rahman (2014). "Numerical simulation of free surface water wave for the flow around NACA 0015 hydrofoil using the volume of fluid (VOF) method". In: *Ocean Engineering* 78, pp. 89–94.

Kinaci, O. K. and M. K. Gokce (2015). "A computational hydrodynamic analysis of Duisburg test case with free surface and propeller". In: *Brodogradnja* 66(4), pp. 23–28.

Klein, T.S., T.J Craft, and H. Iacovides (2014). "Assessment of the performance of different classes of turbulence models in a wide range of non-equilibrium flows". In: *International Journal of Heat and Fluid Flow* 51, pp. 229–256.

Larsson, L. and H. C. Raven (2010). *Ship Resistance and Flow*. Jersey City, N.J: The Society of Naval Architects and Marine Engineers.

Menter, F. R., M. Kuntz, and R. Langtry (2003). "Ten years of industrial experience with the SST turbulence model". In: *Turbulence, Heat and Mass Transfer 4(1)*, pp. 625–632.

Menter, F. and T. Esch (2001). "Elements of industrial heat transfer predictions". In: *16th Brazilian Congress of Mechanical Engineering* 109.

Molland, A. F., T. R. Stephen, and H. A. Dominic (2011). *Ship Resistance and Propulsion: Practical Estimation of Ship Propulsive Power*. Cambridge: Cambridge University Press.

Nagata, S., Y. Imai, K. Toyota, and H. Isshiki (2010). "Thrust Generation by Waves". In: *Proceedings of the Ninth (2010) ISOPE/Asia Offshore Mechanics Symposium*, pp. 155–162.

Naito, S. and H. Isshiki (2005). "Effect of Bow Wings on Ship Propulsion and Motions". In: *Applied Mechanics Reviews* 58, pp. 253–267.

NTNU HPC Group (2018). *Vilje*. Accessed: 15.07.2018. URL: `https://www.hpc.ntnu.no/display/hpc/Vilje`.

Ong, M.C., T. Utnes, L.E. Holmedal, D. Myrhaug, and B. Pettersen (2009). "Numerical simulation of flow around smooth circular cylinder at very high Reynolds numbers". In: *Marine Structures* 22, pp. 142–153.

OpenCFD Ltd (2018a). *OpenFOAM: The open source CFD toolbox*. Accessed: 20.06.2018. URL: `https://openfoam.com/`.

– (2018b). *User Guide*. Accessed: 20.06.2018. URL: `https://openfoam.com/documentation/user-guide/`.

Piehl, H. P. (2016). "Ship Roll Damping Analysis". PhD thesis. University of Duisburg-Essen.

Pletcher, R. H., J. C. Tannehill, and D. A. Anderson (2013). *Computational Fluid Mechanics and Heat Transfer*. 3rd ed. Boca Raton, Fla: CRC Press.

Politis, G. and K. Politis (2014). "Biomimetic propulsion under random heaving conditions, using active pitch control". In: *Journal of Fluids and Structures* 47, pp. 139–149.

Prasad, B., T. Hino, and K. Suzuki (2015). "Numerical simulation of free surface flows around shallowly submerged hydrofoil by OpenFOAM". In: *Ocean Engineering* 102, pp. 87–94.

Shariati, S. K. and S. H. Mousavizadegan (2017). "The effect of appendages on the hydrodynamic characteristics of an underwater vehicle near the free surface". In: *Applied Ocean Research* 67, pp. 31–43.

Spalding, D. B. (1961). "A Single Formula for the "Law of the Wall"". In: *Journal of Applied Mechanics* 28(3), pp. 455–458.

Steen, Sverre (2014). *TMR4247 Marin teknikk 3 - Hydrodynamikk Motstand og propulsjon, Propell og foilteori*. Trondheim: Kompendieforlaget, Akademika.

Strandenes, Håkon (2012). *OpenFOAM - Airfoil Calculations*. Accessed: 22.07.2018. URL: `https://www.hpc.ntnu.no/display/hpc/OpenFOAM+-+Airfoil+Calculations`.

Tennekes, H. and J. L. Lumley (1972). *A First Course in Turbulence*. Cambridge, Massachusetts: The MIT Press. Chap. 2 and 5.

The OpenFOAM Foundation (2017). *OpenFOAM v5 User Guide*. Accessed: 20.06.2018. URL: `https://cfd.direct/openfoam/user-guide`.

United Nations UN Web Services Section, Department of Public Information (2018). *GOALS, Sustainable Development, 17 Goals to transform Our World*. Accessed: 22.05.2018. URL: `https://www.un.org/sustainabledevelopment/`.

Wavefoil (2018). *Wavefoil - Retractable Bow Foil*. Accessed: 03.08.2018. URL: `https://www.wavefoil.com/`.

White, F. M. (2006). *Viscous Fluid Flow*. 3rd ed. Boston: McGraw-Hill Higher Education. Chap. 6.

Xie, N. and D. Vassalos (2007). "Performance analysis of 3D hydrofoil under free surface". In: *Ocean Engineering* 34(8), pp. 1257–1264.

Appendix A

Solver Files - fvSolution

Solver File for Double Body Analysis

```
/*--------------------------------*- C++ -*----------------------------------*\
| =========                 |                                                 |
| \\      /  F ield         | OpenFOAM: The Open Source CFD Toolbox           |
|  \\    /   O peration     | Version:  5                                     |
|   \\  /    A nd           | Web:      www.OpenFOAM.org                      |
|    \\/     M anipulation  |                                                 |
\*---------------------------------------------------------------------------*/
FoamFile
{
    version     2.0;
    format      ascii;
    class       dictionary;
    location    "system";
    object      fvSolution;
}
// * * * * * * * * * * * * * * * * * * * * * * * * * * * * * * * * * * * * ** //

solvers
{
    p
    {
        solver          GAMG;
        smoother        GaussSeidel;
        tolerance       1e-08;
        relTol          0.01;
        nPreSweeps      0;
        nPostSweeps     2;
        cacheAgglomeration true;
        nCellsInCoarsestLevel 10;
        agglomerator    faceAreaPair;
        mergeLevels     1;
    }


    U
    {
        solver          smoothSolver;
        smoother        GaussSeidel;
        nSweeps         2;
        tolerance       1e-09;
        relTol          0;
    }


    k
    {
        solver          smoothSolver;
        smoother        GaussSeidel;
```

```
        tolerance       1e-9;
        relTol          0;
        nSweeps         2;
    }

    omega
    {
        solver          smoothSolver;
        smoother        GaussSeidel;
        tolerance       1e-9;
        relTol          0;
        nSweeps         2;
    }


    cellDisplacement
    {
        solver          GAMG;
        smoother        GaussSeidel;
        tolerance       1e-09;
        relTol          0;
        cacheAgglomeration true;
        nCellsInCoarsestLevel 10;
        agglomerator    faceAreaPair;
        mergeLevels     1;
    }
}

SIMPLE
{
    nNonOrthogonalCorrectors 3;

    residualControl
    {
        p               1e-6;
        U               1e-6;
        "(k|omega)"     1e-6;
    }
}

relaxationFactors
{
    fields
    {
        p               0.3;
    }
    equations
    {
        U               0.7;
        "(k|omega).*" 0.7;
    }
}


cache
{
    grad(U);
}

// ************************************************* //
```

Solver File for Free Surface Analysis

```
/*--------------------------------*- C++ -*----------------------------------*\
| =========                 |                                                 |
| \\      /  F ield         | OpenFOAM: The Open Source CFD Toolbox           |
|  \\    /   O peration     | Version:  plus                                  |
|   \\  /    A nd           | Web:      www.OpenFOAM.com                      |
|    \\/     M anipulation  |                                                 |
\*---------------------------------------------------------------------------*/
FoamFile
{
    version     2.0;
    format      ascii;
    class       dictionary;
    location    "system";
    object      fvSolution;
}
// * * * * * * * * * * * * * * * * * * * * * * * * * * * * * * * * * * * * * * * * * * * * * * * * * * * * * * * * //

solvers
{
    "alpha.water.*"
    {
        nAlphaCorr      3;
        nAlphaSubCycles 1;
        cAlpha          1;
        icAlpha         0;

        MULESCorr       yes;
        nLimiterIter    10;
        alphaApplyPrevCorr  yes;

        solver          smoothSolver;
        smoother        symGaussSeidel;
        tolerance       1e-10;
        relTol          0;
        minIter         1;
    }

    "pcorr.*"
    {
        solver          GAMG;
        smoother        DIC;
        tolerance       0.1;
        relTol          0;
    };

    p_rgh
    {
        solver          GAMG;
        smoother        GaussSeidel;
        tolerance       1e-7;
        relTol          0.001;
    };

    p_rghFinal
    {
        $p_rgh;
        relTol          0;
    };

    "(U|k|omega)"
    {
        solver          smoothSolver;
        smoother        GaussSeidel;
        nSweeps         2;

        tolerance       1e-8;
        relTol          0.001;
        minIter         1;
    };
```

```
    "(U|k|omega)Final"
    {
        solver          smoothSolver;
        smoother        GaussSeidel;
        nSweeps         2;

        tolerance       1e-8;
        relTol          0;
        minIter         1;
    };

    cellDisplacement
    {
        solver          GAMG;
        smoother        GaussSeidel;
        tolerance       1e-09;
        relTol          0;
        cacheAgglomeration true;
        nCellsInCoarsestLevel 10;
        agglomerator     faceAreaPair;
        mergeLevels      1;
    }
}

PIMPLE
{
    momentumPredictor   yes;

    nOuterCorrectors    3;
    nCorrectors         2;
    nNonOrthogonalCorrectors 0;


}

relaxationFactors
{
    equations
    {
        ".*" 1;
    }
}

cache
{
    grad(U);
}


// ************************************************************************* //
```

Appendix B

Discretisation Files - fvSchemes

Discretisation File for Double Body Analysis

```
/*--------------------------------*- C++ -*----------------*\
| =========                      |                                                 |
| \\      /  F ield              | OpenFOAM: The Open Source CFD Toolbox           |
|  \\    /   O peration          | Version:  5                                     |
|   \\  /    A nd                | Web:      www.OpenFOAM.org                      |
|    \\/     M anipulation       |                                                 |
\*---------------------------------------------------------------------------*/
FoamFile
{
    version     2.0;
    format      ascii;
    class       dictionary;
    location    "system";
    object      fvSchemes;
}
// * * * * * * * * * * * * * * * * * * * * * * * * * * * * * * * * * * * * //

ddtSchemes
{
    default         steadyState;
}

gradSchemes
{
    default         Gauss linear;
    limitedGrad     cellLimited Gauss linear 1;
}

divSchemes
{
    default         none;
    div(phi,U)      bounded Gauss linearUpwindV grad(U);
    div(phi,k) bounded Gauss linearUpwind limitedGrad;
    div(phi,omega) bounded Gauss linearUpwind limitedGrad;
    div((nuEff*dev2(T(grad(U))))) Gauss linear;
}

laplacianSchemes
{
    default         Gauss linear corrected;
    laplacian(diffusivity,cellDisplacement) Gauss linear corrected;
}

interpolationSchemes
{
    default         linear;
}
```

```
snGradSchemes
{
    default         corrected;
}

wallDist
{
    method meshWave;
    correctWalls true;
}


// ************************************************************************* //
```

Discretisation File for Free Surface Analysis

```
/*--------------------------------*- C++ -*----------------------------------*\
| =========                 |                                                 |
| \\      /  F ield         | OpenFOAM: The Open Source CFD Toolbox           |
|  \\    /   O peration     | Version:  plus                                  |
|   \\  /    A nd           | Web:      www.OpenFOAM.com                      |
|    \\/     M anipulation  |                                                 |
\*---------------------------------------------------------------------------*/
FoamFile
{
    version     2.0;
    format      ascii;
    class       dictionary;
    location    "system";
    object      fvSchemes;
}
// * * * * * * * * * * * * * * * * * * * * * * * * * * * * * * * * * * * * * //

ddtSchemes
{
    default         Euler;
}

gradSchemes
{
    default         Gauss linear;
    limitedGrad     cellLimited Gauss linear 1;
}

divSchemes
{
    div(rhoPhi,U)   Gauss linearUpwind grad(U);
    div(phi,alpha)  Gauss vanLeer;
    div(phirb,alpha) Gauss linear;
    div(phi,k)      Gauss linearUpwind limitedGrad;
    div(phi,omega)  Gauss linearUpwind limitedGrad;
    div(((rho*nuEff)*dev2(T(grad(U))))) Gauss linear;
}

laplacianSchemes
{
    default         Gauss linear corrected;
    laplacian(diffusivity,cellDisplacement) Gauss linear corrected;
}

interpolationSchemes
{
    default         linear;
}

snGradSchemes
{
    default         corrected;
}

wallDist
{
    method meshWave;
    correctWalls true;
}


// ************************************************************************* //
```

Appendix C

Additional Results - Bare Hull

C.1 Pressure Resistance Mesh Independence Study

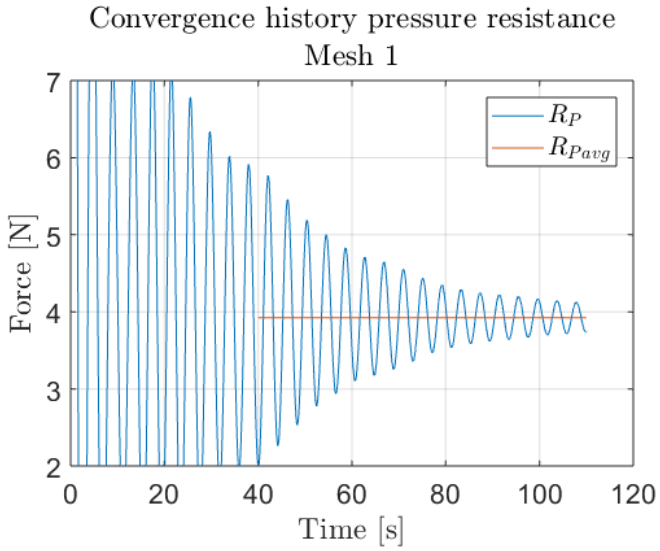

(a) Mesh 1.

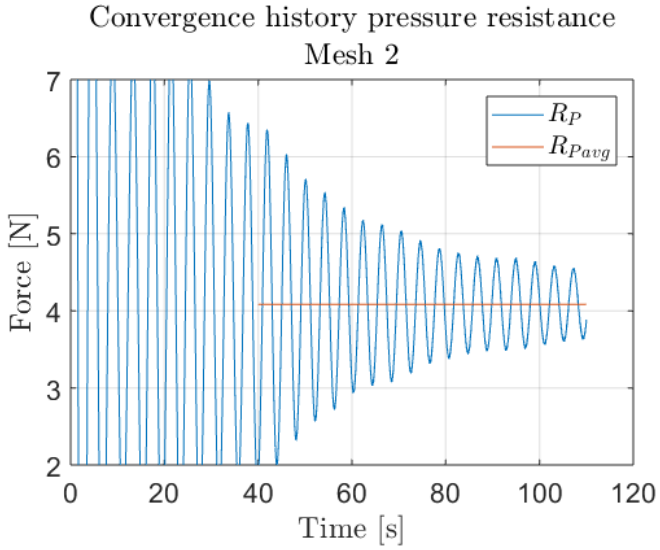

(b) Mesh 2.

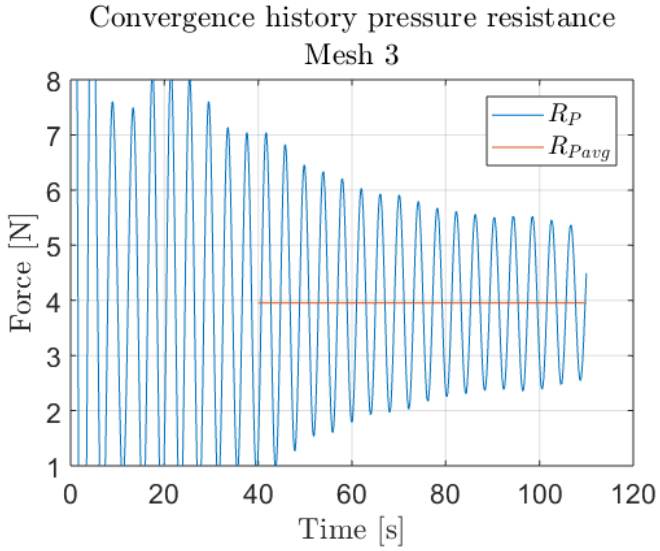

(c) Mesh 3.

Figure C.1: Convergence of pressure resistance for mesh independence study of bare hull.

C.2 Residuals From Mesh Independence Study

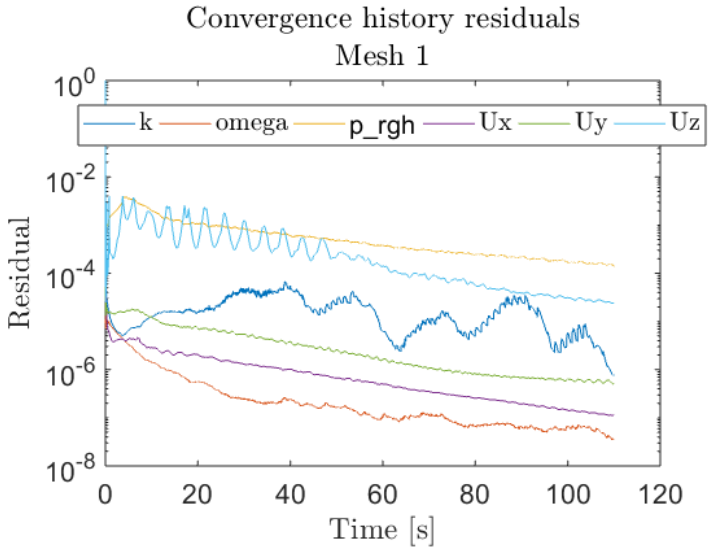

(a) Mesh 1.

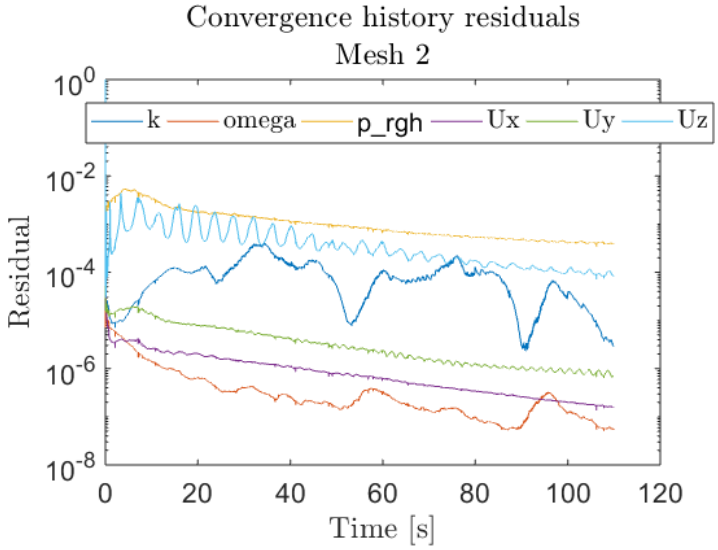

(b) Mesh 2.

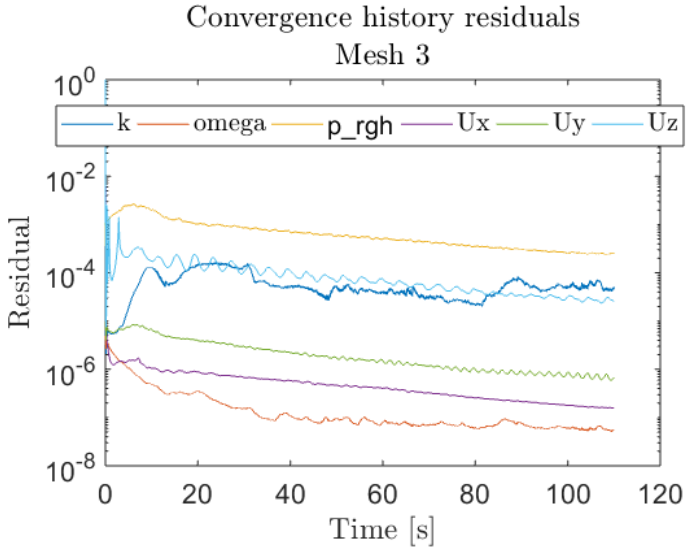

(c) Mesh 3.

Figure C.2: Residual convergence from mesh independence study of bare hull.

C.3 Pressure Resistance Time Step Study

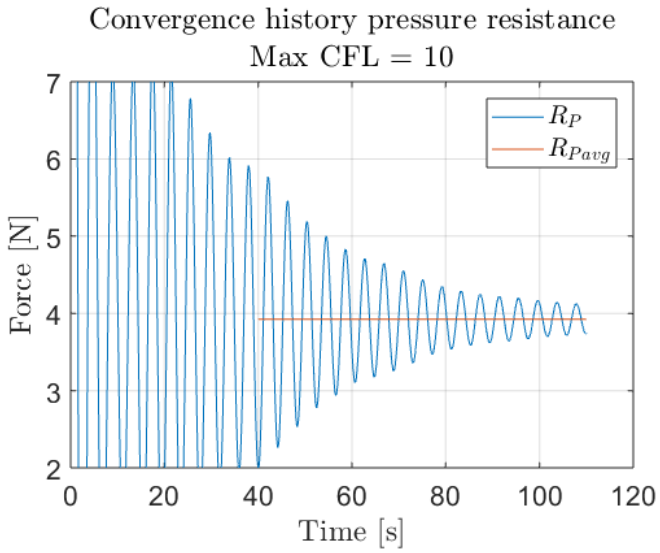

(a) Mesh1, max CFL = 10.

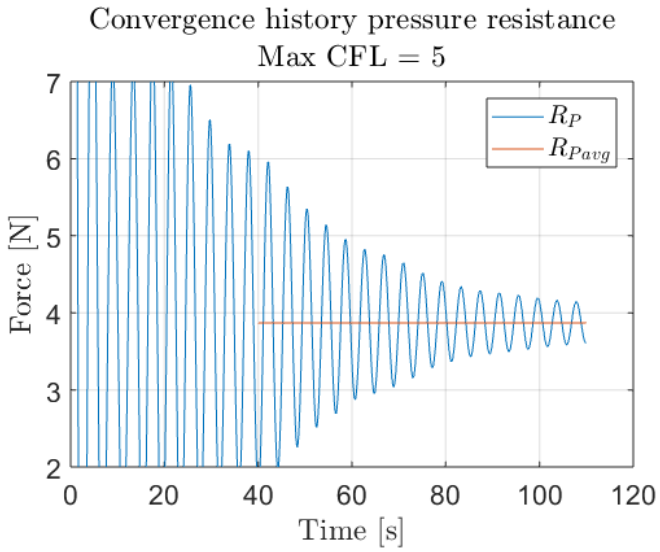

(b) Mesh1, max CFL = 5.

Figure C.3: Convergence of pressure resistance for time step study on mesh 1 of bare hull.

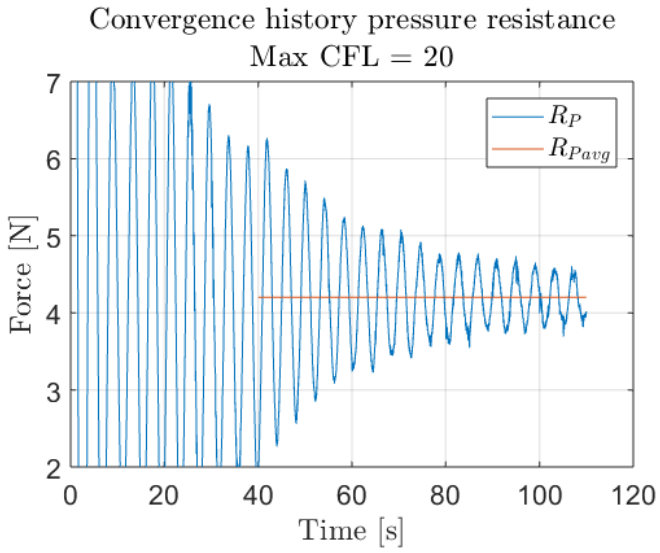

(a) Mesh 2, max CFL = 20.

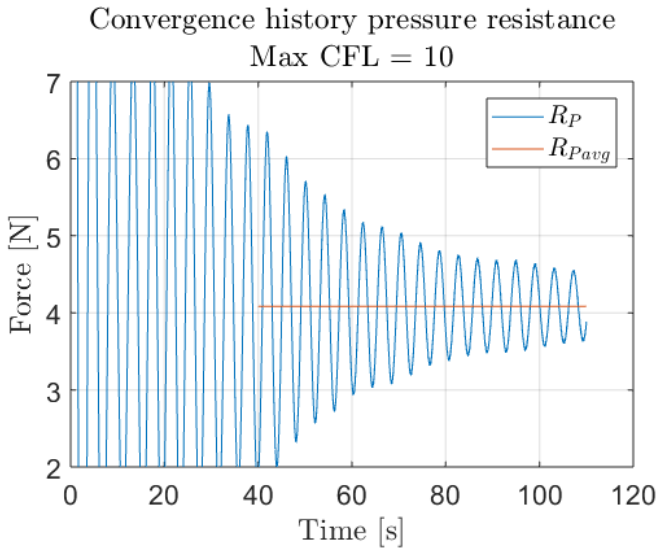

(b) Mesh 2, max CFL = 10.

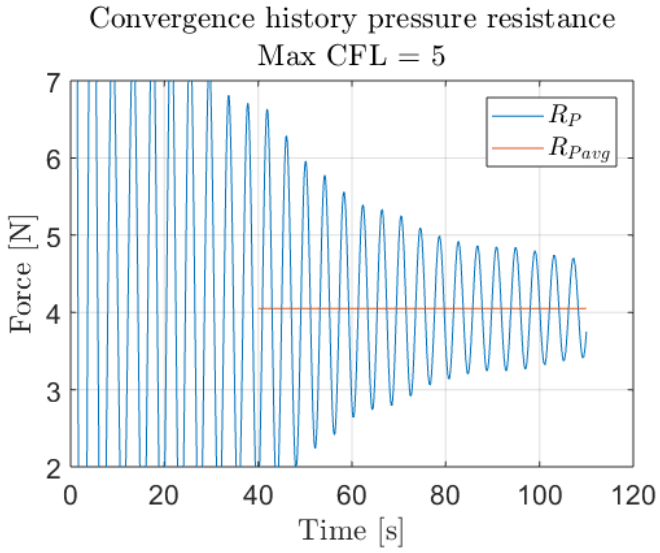

(c) Mesh 2, max CFL = 5.

Figure C.4: Convergence of pressure resistance for time step study on mesh 2 of bare hull.

C.4 Residuals From Time Step Study

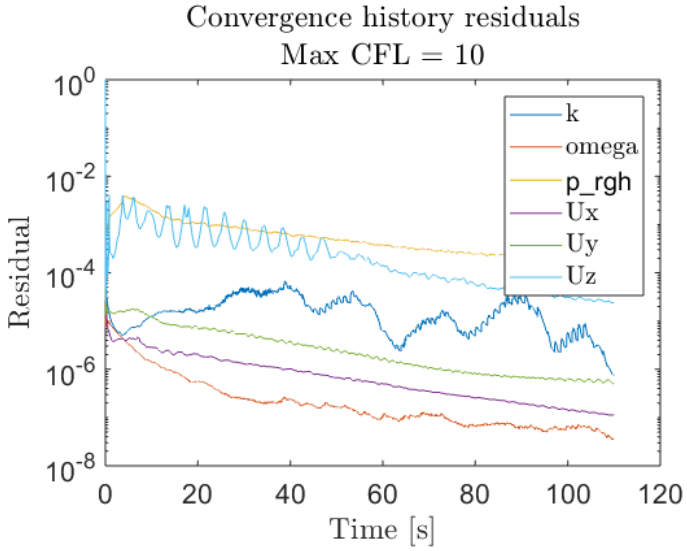

(a) Mesh 1, max CFL = 10.

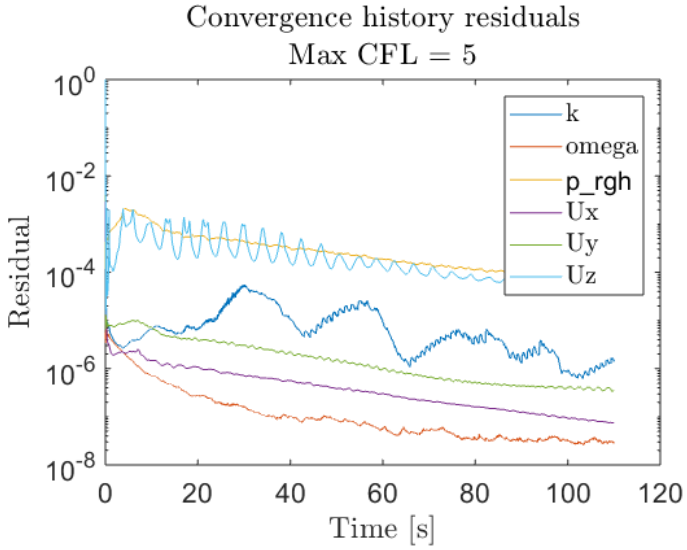

(b) Mesh 1, max CFL = 5.

Figure C.5: Residual convergence from time step study on mesh 1 of bare hull.

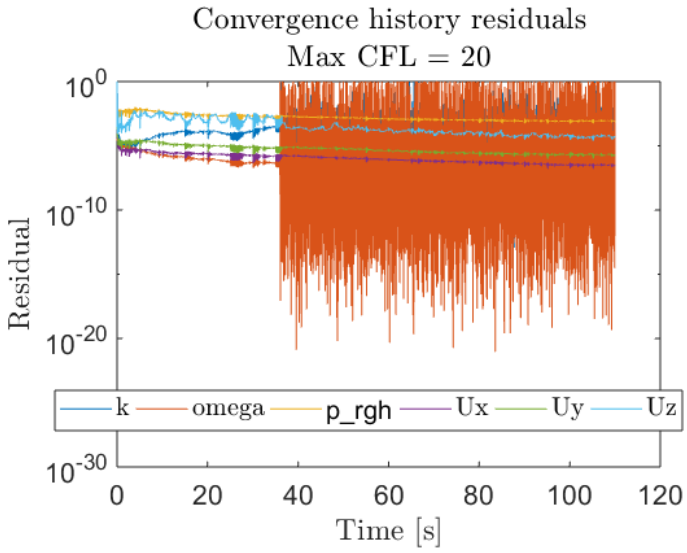

(a) Mesh 2, max CFL = 20.

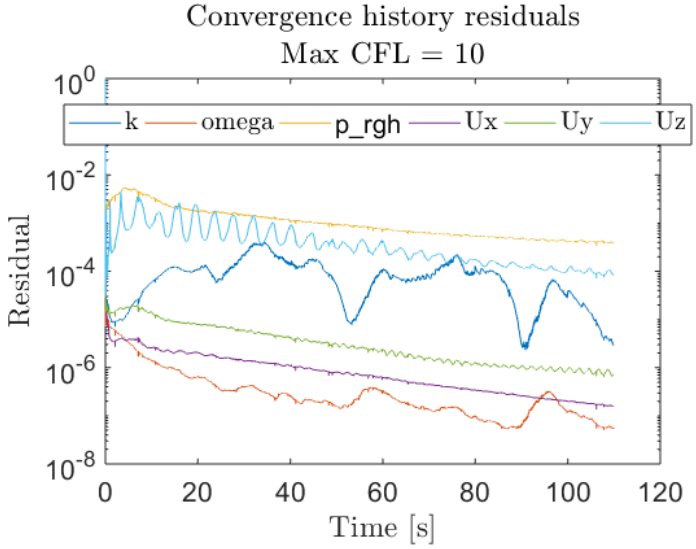

(b) Mesh 2, max CFL = 10.

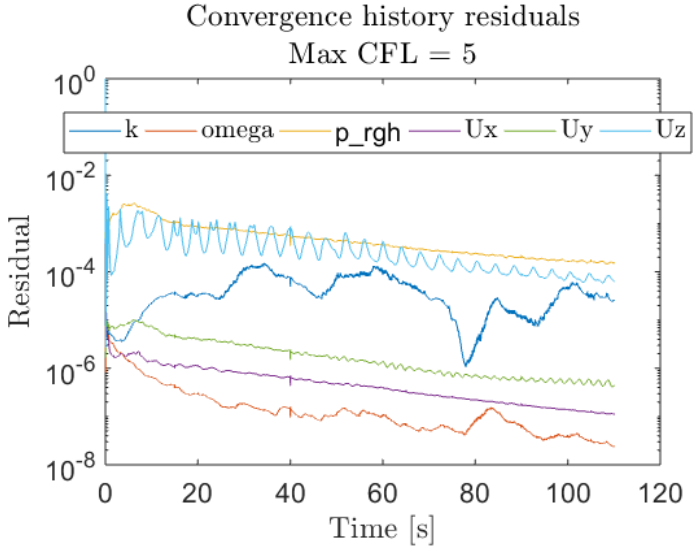

(c) Mesh 2, max CFL = 5.

Figure C.6: Residual convergence from time step study on mesh 2 of bare hull.

C.5 Results for Three Forward Speeds

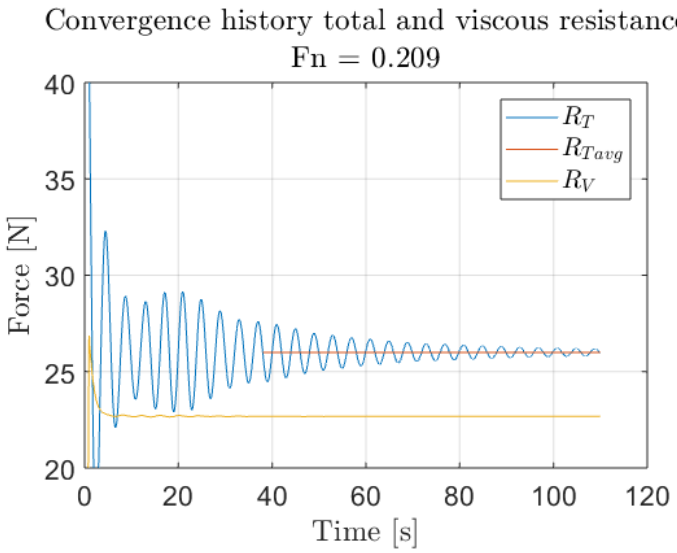

(a) Fn = 0.209.

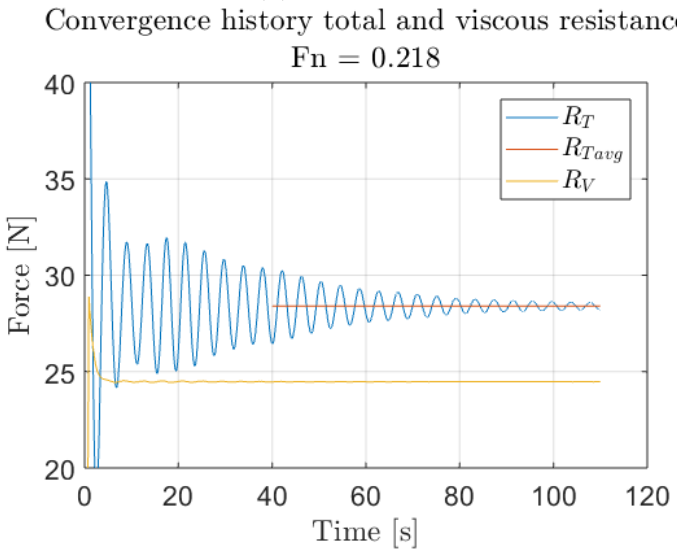

(b) Fn = 0.218.

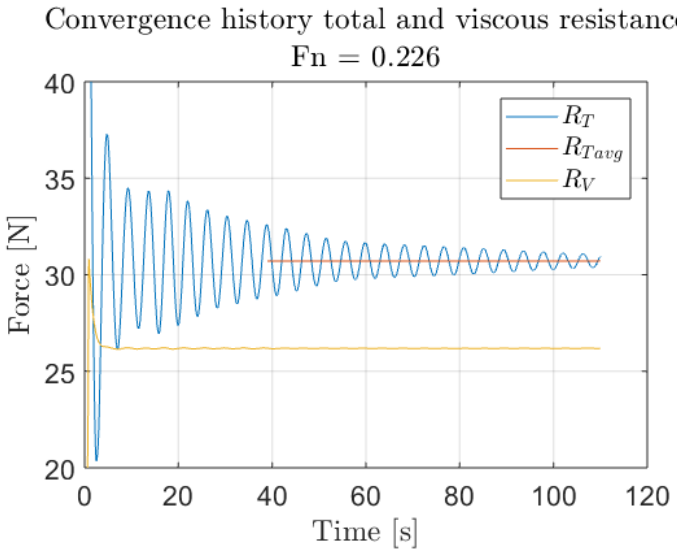

(c) Fn = 0.226.

Figure C.7: Convergence history total and viscous resistance for three forward speeds - Bare hull analysis.

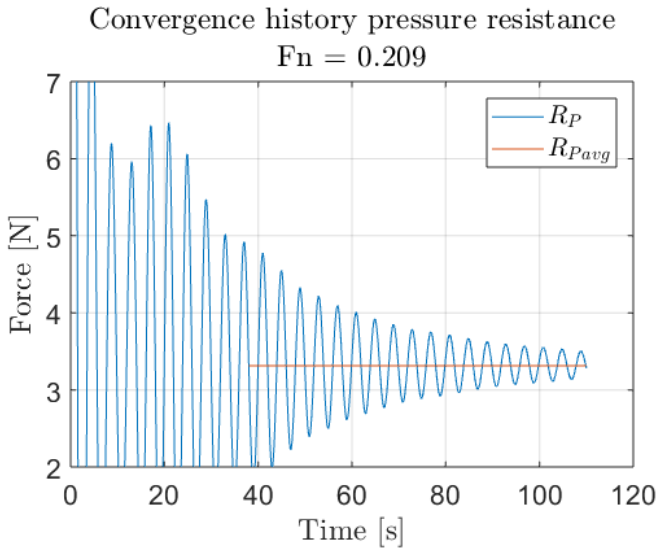

(a) Fn = 0.209.

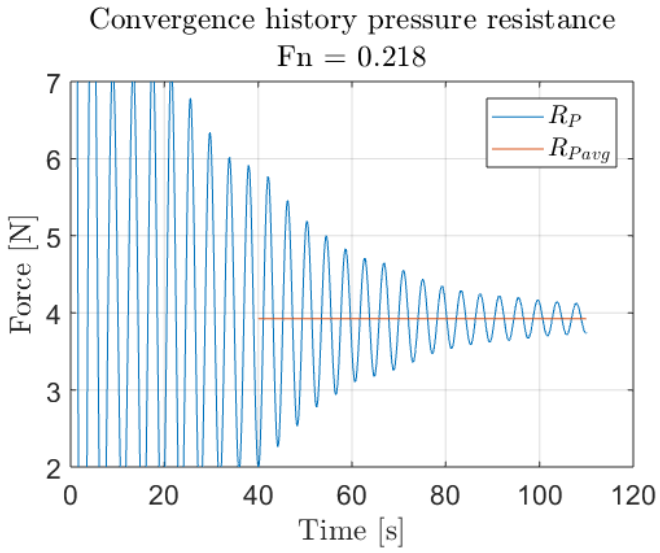

(b) Fn = 0.218.

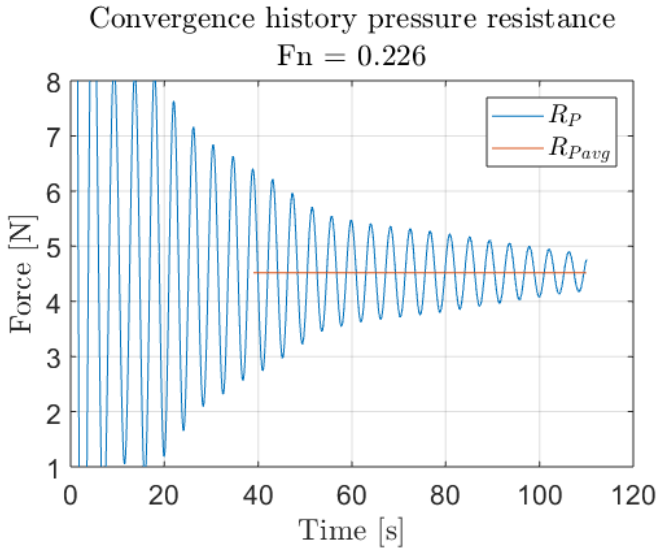

(c) Fn = 0.226.

Figure C.8: Convergence history pressure resistance for three forward speeds - Bare hull analysis.

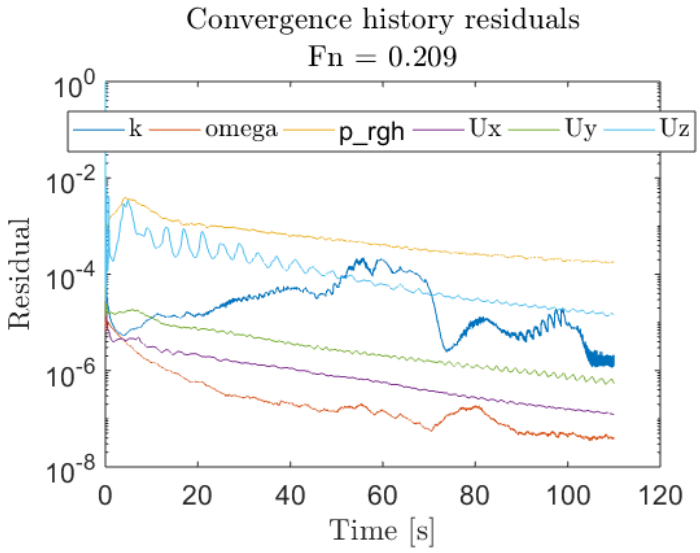

(a) Fn = 0.209.

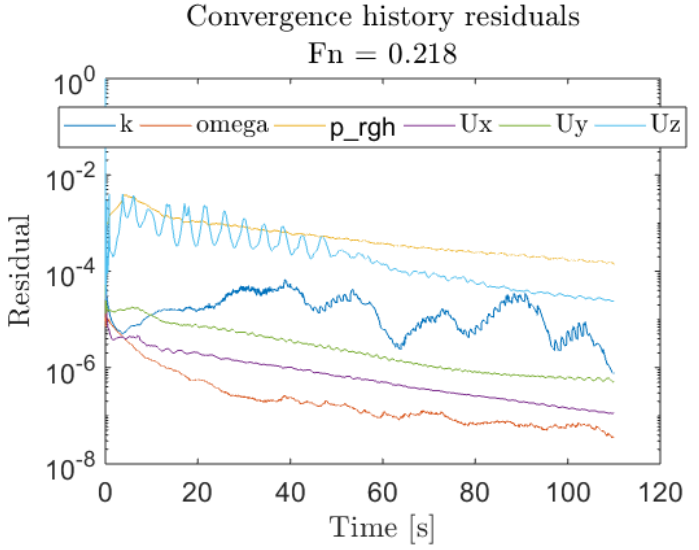

(b) Fn = 0.218.

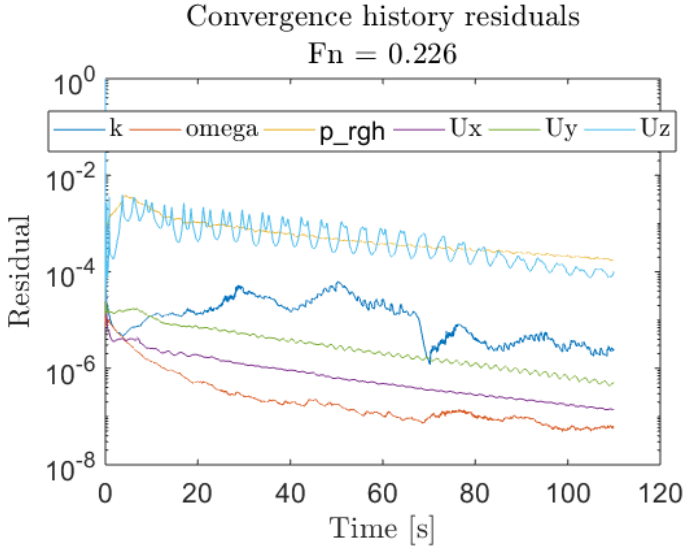

(c) Fn = 0.226.

Figure C.9: Residual convergence for three forward speeds - Bare hull analysis.

Appendix D

Additional Results - Hull With Wavefoil

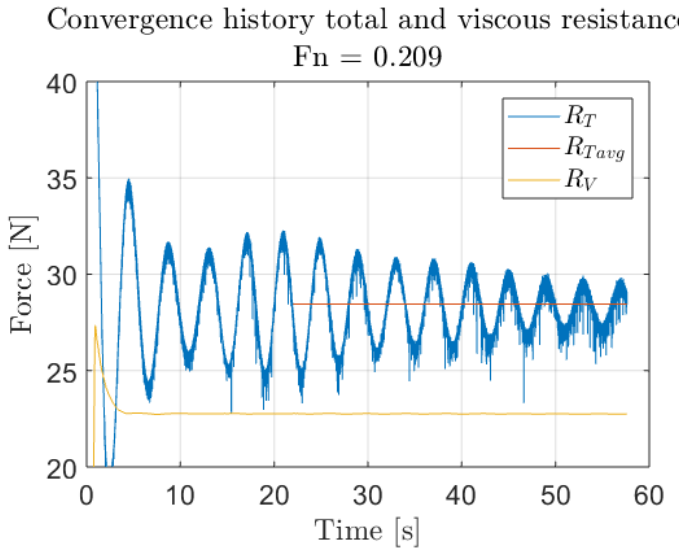

(a) Fn = 0.209.

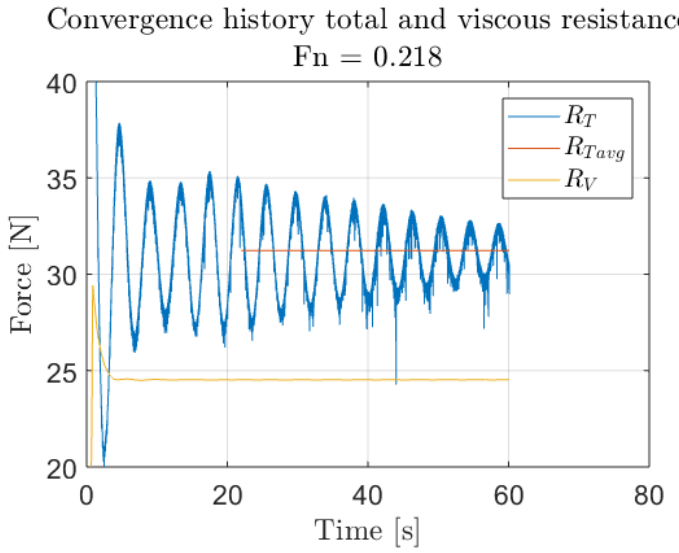

(b) Fn = 0.218.

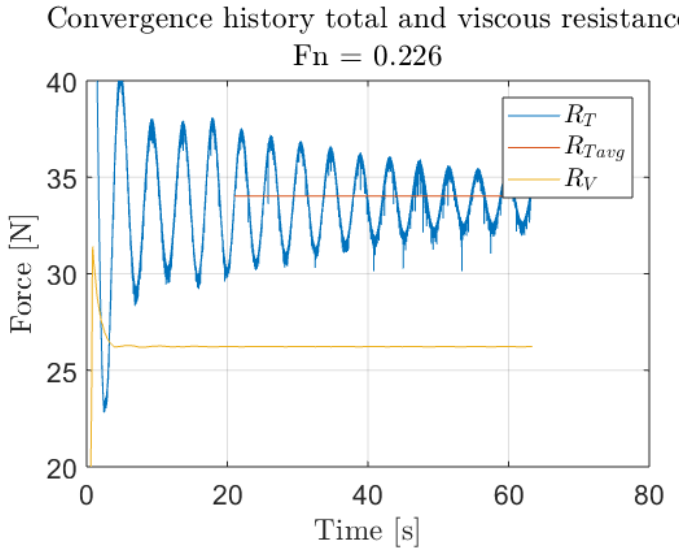

(c) Fn = 0.226.

Figure D.1: Convergence of total and viscous resistance on hull.

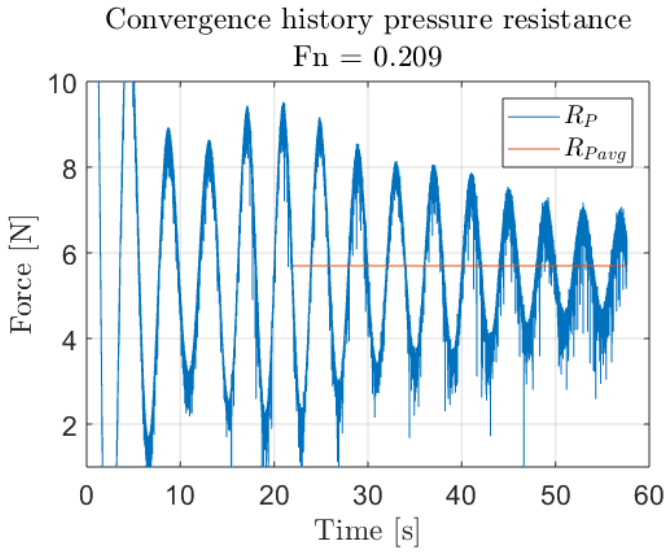

(a) Fn = 0.209.

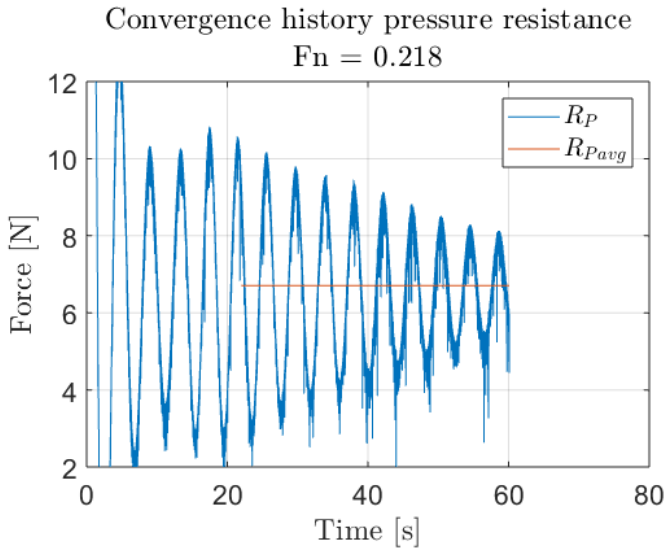

(b) Fn = 0.218.

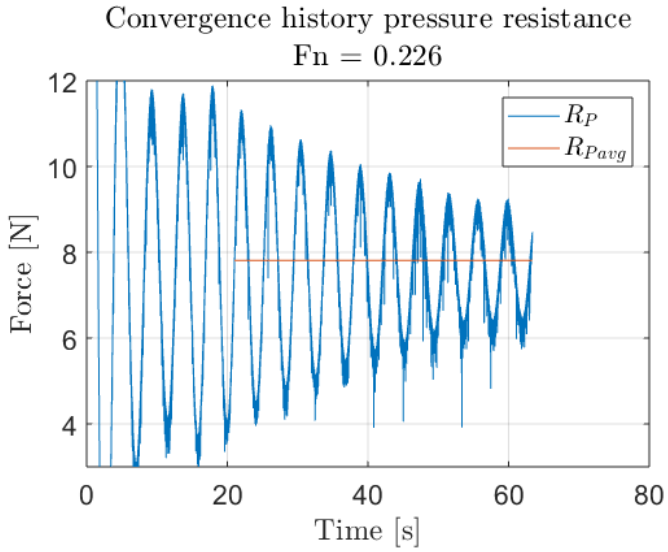

(c) Fn = 0.226.

Figure D.2: Convergence of pressure resistance on hull.

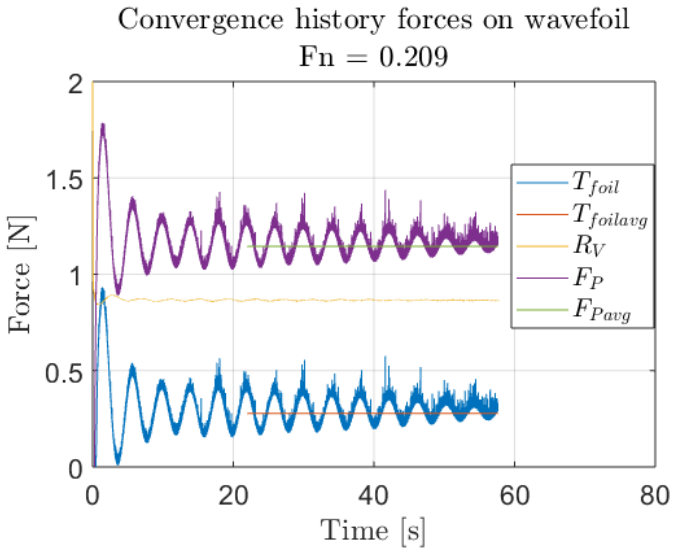

(a) Fn = 0.209.

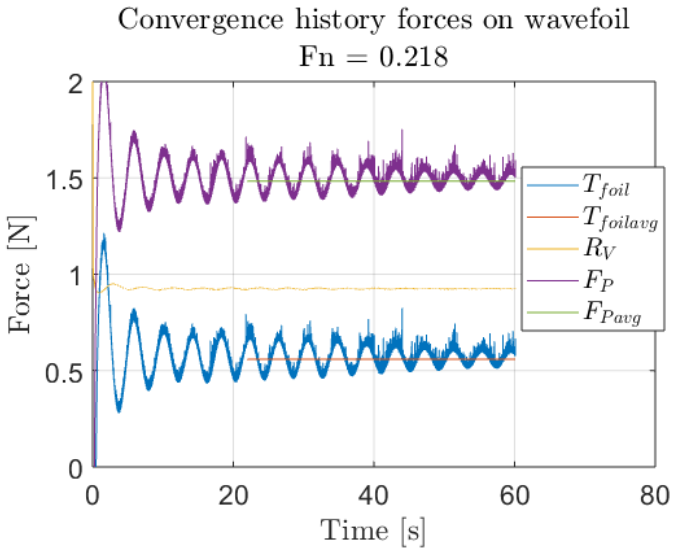

(b) Fn = 0.218.

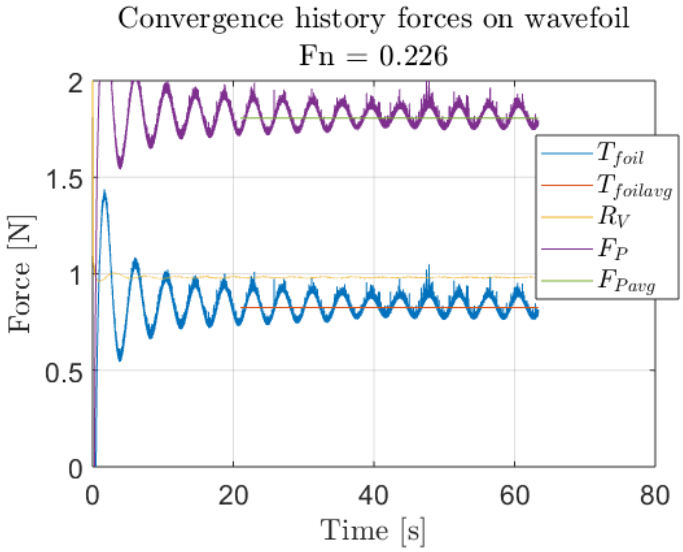

(c) Fn = 0.226.

Figure D.3: Convergence of forces on wavefoil.

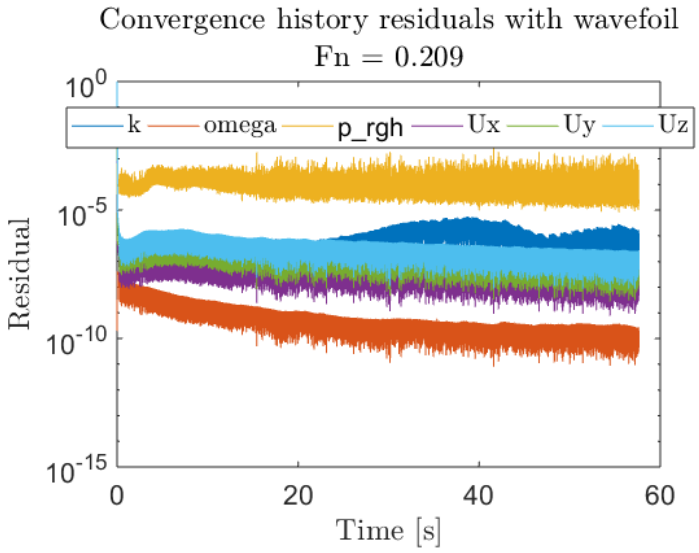

(a) Fn = 0.209.

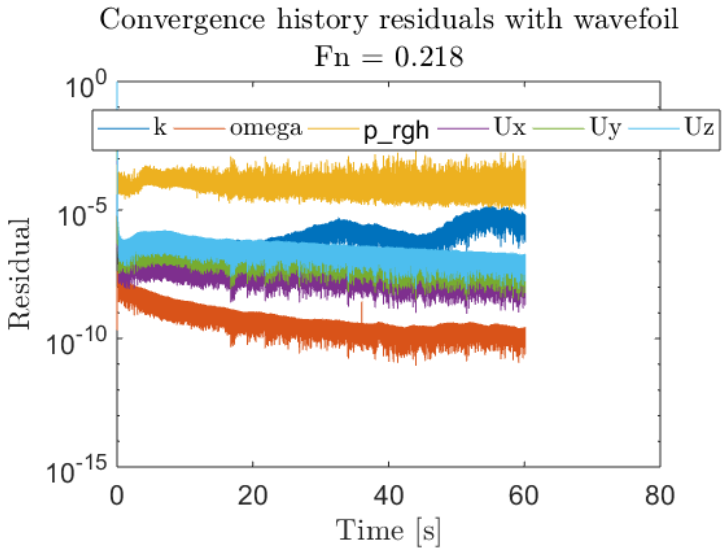

(b) Fn = 0.218.

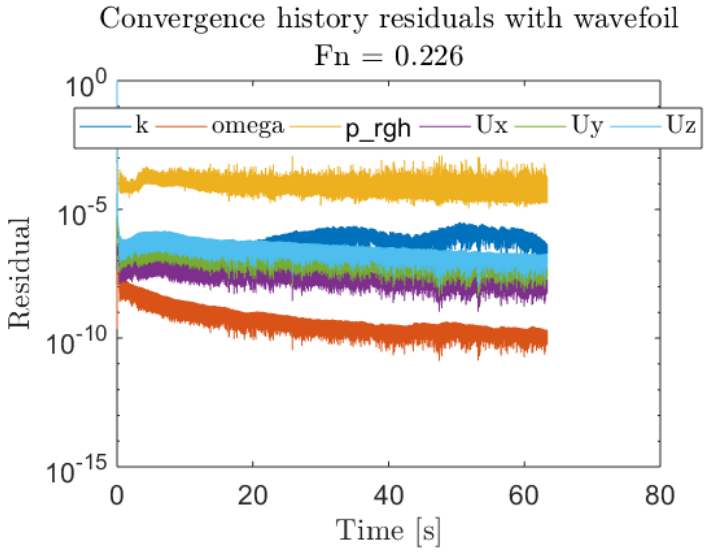

(c) Fn = 0.226.

Figure D.4: Residual convergence - Hull with wavefoil analysis.

Appendix E

Electronic Appendages

A list of electronic appendages attached in a .zip folder is presented below.

- DoubleBody - Folder containing the necessary file structure for meshing and running the double body analysis in OpenFOAM
- DTCHull_bare_1668 - Folder containing the necessary file structure for meshing and running a free surface analysis of the bare hull at design speed.
- DTCHull_foil_1668 - Folder containing the necessary file structure for meshing and running a free surface analysis of the ship hull with the wavefoil at design speed.
- Poster.pdf - A poster made in connection with presenting the master thesis.